Interactions and optical properties of microorganisms on surfaces

Rafaël Naomi Sibilo

ICFO – Institut de Ciències Fotòniques

UPC – Universitat Politècnica de Catalunya

Interactions and optical properties of microorganisms on surfaces

Rafaël Naomi Sibilo

Thesis Advisor: Prof. Dr. Valerio Pruneri

This dissertation is submitted for the degree of: Doctor of Philosophy

Barcelona, July 2021

To my parents, André & Joyce and
my brothers I'saï & Othniël

For existence is summarized in unconditional love.

By faith we understand that the worlds were framed by the word of God, so that the things which are seen were not made of things which are visible.
Hebrews 11:3

Abstract

Controlling microbial growth is essential to industries such as healthcare, food, pharmacy but also for ship hulls and water systems. Interactions of bacteria with surfaces are highly dynamic and complex. Once a single cell transitions to a persistent multicellular microbial community (biofilm), elimination becomes complicated. Bacterial adherence, growth, and detachment are regulated by biological, chemical, physical, mechanical, and electrical properties of the bacterial cell, the surface, and the surrounding medium. Comprehensive studies in this field therefore require a multidisciplinary approach involving experts from different branches of science and appropriate choices of equipment depending on the question to address. This thesis focuses on the interaction and optical properties of bacteria on surfaces. More specifically, it investigates novel methods for enhanced bacteria detection, growth monitoring and presents an in-depth study of interaction mechanisms of bacteria and surface nano-structures.

In the first part of the thesis, we validate a newly in-house built bio-sensing device to detect cells and their growth on surfaces. The proposed surface cytometer is compared with two standard laboratory methods, spectrophotometry and fluorescence microscopy. The results obtained with the three different techniques show similar trends, confirming the suitability of the surface cytometer as a compact, fast and low-cost device for measuring bacterial growth. Distinctively, the surface cytometer possesses both a large field-of view (~200 mm^2) and depth of focus (~2 mm), these being particularly interesting for in-situ measurements and point-of-care testing.

In order to enhance cell imaging, we propose a new type of surface, ultrathin (<10nm) gold films on a transparent substrate, such as glass. Such a surface has the capability to quench background fluorescence, improving microscopy and imaging. This is demonstrated through both numerical simulations and experiments. The physical mechanism at the basis of our design is that metals can reduce the lifetime of a fluorophore in its proximity. On the contrary, fluorophores further from the surface, because of their separation from the metal due to cell body, will maintain a much higher level of signal, i.e. they are less quenched. The higher signal-to-noise ratio (SNR) compared with a glass bare substrate is observed in both air and water. An improved SNR promotes the collection of a higher number of photons leading to more accurate localization precision, while reducing background, thanks to lower laser powers and shorter acquisition times. The enhanced imaging mediated through an ultrathin metal has potential in single-molecule localization super-resolution microscopy and live-cell imaging applications, especially under controlled conditions to minimize photodamage.

In another study of the thesis, we demonstrate that bacterial growth can be regulated by tuning surface wettability. In contrast to commonly used indirect methods such as bacterial colony counting and scanning electron microscopy, we investigated a direct approach for assessment. First, we used molecular dynamics simulations to predict bacterial behavior on flat and nanostructured glass substrates, with wetting characteristics further modulated by chemical coatings. Then, we experimentally assessed these findings using *E. coli* bacteria and time-lapse fluorescence microscopy. Obtained data confirmed that nanostructured glass simultaneously hydrophobic, repelling water, and oleophilic, attracting fat, is most destructive, avoids cell adherence and promotes total cell disruption. These direct observations reflect a more accurate spatial- and time evolution of the

interactions and bactericidal effects due to surface morphology and wettability. The results provide guidelines to design antimicrobial surfaces using simple nano-structuring and chemistry.

Resumen

El control del crecimiento microbiano es esencial en las industrias de salud, alimentación y, farmacia, pero también, en la superficie de los cascos de los barcos y en los sistemas de tratamiento de agua. Las interacciones de las bacterias con las superficies son muy dinámicas y complejas. Cuando una sola célula se convierte en una comunidad microbiana multicelular persistente (biopelícula), la eliminación se complica. La adherencia, el crecimiento y el desprendimiento de bacterias están regulados por las propiedades biológicas, químicas, físicas, mecánicas y eléctricas de la célula bacteriana, la superficie y el medio circundante. Por lo tanto, los estudios integrales en este campo requieren un enfoque multidisciplinario que involucre a expertos de diferentes ramas de la ciencia y elecciones adecuadas de equipos en función de la cuestión a abordar. Esta tesis se centra en la interacción y las propiedades ópticas de las bacterias con las superficies. Más específicamente, investiga métodos novedosos para mejorar la detección de bacterias, el seguimiento del crecimiento bacteriano y presenta un estudio en profundidad de los mecanismos de interacción entre bacterias y superficies nanoestructuradas.

En la primera parte de esta tesis, validamos la tecnología del citómetro de superficie, dispositivo de detección biológica de reciente construcción para detectar células y su crecimiento en superficies. Este dispositivo propuesto se compara con dos métodos de laboratorio estándar, espectrofotometría y microscopía de fluorescencia. Los resultados obtenidos mediante las tres técnicas nombradas muestran tendencias similares, confirmando la idoneidad del citómetro de superficie como un dispositivo compacto, rápido y de bajo coste para la medición del crecimiento bacteriano. De manera distintiva, el citómetro de superficie posee un gran campo de visión (~ 200 mm^2) y una elevada profundidad de enfoque (~ 2 mm), lo que es particularmente interesante para las mediciones in situ y las pruebas en el lugar de atención.

En esta tesis proponemos un nuevo tipo de superficie, películas de oro ultrafinas (<10 nm) sobre un sustrato transparente, como el vidrio, para mejorar la imagen celular. Esta superficie tiene la capacidad de apagar la fluorescencia de fondo, mejorando la microscopía y la formación de imágenes. Esto se expresa mediante simulaciones numéricas y experimentos. El mecanismo físico de la base de nuestro diseño es que los metales pueden reducir la vida útil de un fluoróforo en sus proximidades. Por el contrario, los fluoróforos más alejados de la superficie, debido a su separación del metal del cuerpo celular, mantendrán un nivel de señal mucho más alto, es decir, estarán menos apagados. La mayor relación señal-ruido (SNR, por sus siglas en inglés) en comparación con un sustrato virgen de vidrio se observa tanto en el aire como en el agua. Una SNR mejorada promueve la recolección de un mayor número de fotones, lo que conduce a una precisión de localización más precisa, al tiempo que se reduce el fondo, gracias a la menor potencia del láser y a los tiempos de adquisición más cortos. La obtención de imágenes mejoradas mediante un metal ultrafino muestra un potencial en aplicaciones de microscopía de superresolución de localización de una sola molécula y de imágenes de células vivas, especialmente en condiciones controladas para minimizar el fotodaño.

En otro estudio de la tesis, demostramos que el crecimiento bacteriano se puede regular ajustando la humectabilidad de la superficie. En contraste con los métodos indirectos comúnmente utilizados, como el recuento de colonias bacterianas y la microscopía electrónica de barrido, investigamos un

enfoque directo para la evaluación. Primero, utilizamos simulaciones de dinámica molecular para predecir el comportamiento bacteriano en sustratos de vidrio planos y nanoestructurados, con características de humectación moduladas aún más por recubrimientos químicos. Luego, evaluamos experimentalmente estos hallazgos utilizando bacterias, E. coli, y microscopía de fluorescencia de lapso de tiempo. Los datos obtenidos confirmaron que el vidrio nanoestructurado hidrofóbico, repelente de agua, y oleofílico, que atrae grasas, es el más destructivo, evitando la adherencia celular y promoviendo la rotura celular total. Estas observaciones directas reflejan una evolución espacial y temporal más precisa de las interacciones y los efectos bactericidas debido a la morfología de la superficie y la humectabilidad. Los resultados obtenidos proporcionan directrices para diseñar superficies antimicrobianas utilizando una simple nanoestructuración y química.

Resum

El control del creixement microbià és essencial en les indústries de la salut, alimentació i farmàcia, però també en la superfície dels cascs dels vaixells i en els sistemes de tractament d'aigües. Les interaccions dels bacteris amb les superfícies són molt dinàmiques i complexes. Quan una sola cèl·lula es converteix en una comunitat microbiana multicel·lular persistent (biopel·lícula), la seva eliminació es torna complicada. L'adherència, el creixement i el despreniment dels bacteris està regulat per les propietats biològiques, químiques, físiques, mecàniques i elèctriques de la cèl·lula bacteriana, la superfície i el medi circumdant. Així doncs, els estudis integrals en aquest camp requereixen un enfocament multidisciplinari que involucri experts de diferents rames de la ciència i eleccions adequades d'equips en funció de la qüestió a abordar. Aquesta tesi se centra en la interacció i les propietats òptiques dels bacteris amb les superfícies. Més específicament, investiga nous mètodes per millorar la detecció de bacteris, el seguiment del creixement bacterià i presenta un estudi en profunditat dels mecanismes d'interacció entre bacteris i superfícies nanoestructurades.

En la primera part d'aquesta tesi, validarem la tecnologia del citòmetre de superfície, un dispositiu de detecció biològica de recent construcció per a detectar cèl·lules i el seu creixement en superfícies. Aquest dispositiu proposat es compara amb dos mètodes de laboratori estàndard, espectrofotometria i microscòpia de fluorescència. Els resultats obtinguts a partir de les tres tècniques esmentades mostren tendències similars, confirmand la idoneïtat del citòmetre de superfície com a un dispositiu compacte, ràpid i de baix cost per a la mesura del creixement bacterià. De manera distintiva, el citòmetre de superfície posseeix un gran camp de visió (~200mm^2) i una elevada profunditat d'enfocament (~2mm), els quals són particularment interessants per a les mesures in situ i les proves en el lloc d'atenció.

En aquesta tesi proposem un nou tipus de superfície, pel·lícules d'or ultrafines (<10 nm) sobre un substrat transparent, com el vidre, per millorar la imatge cel·lular. Aquesta superfície té la capacitat d'apagar la fluorescència del fons, millorant la microscòpia i la formació d'imatges. Això s'expressa a partir de simulacions numèriques i experiments. El mecanisme físic de la base del nostre disseny és que els metalls poden reduir la vida útil d'un fluoròfor en la seva proximitat. Al contrari, els fluoròfors més allunyats de la superfície, donada la separació del metall del cos cel·lular, mantindran un nivell del senyal molt més alt, és a dir, hi seran menys apagats. La millor relació senyal-soroll (SNR, per les seves sigles en anglès) en comparació amb un substrat verge de vidre s'observa tant com en l'aire com en l'aigua. Una SNR millorada promou la recol·lecció d'un major nombre de fotons, el que condueix a una precisió de localització més precisa, al mateix temps que es redueix el fons, gràcies a la menor potència del làser i als temps d'adquisició més curts. L'obtenció d'imatges millorades a partir d'un metall ultrafí demostra un potencial en aplicacions de microscòpia de superresolució de localització d'una sola molècula i d'imatges de cèl·lules vives, especialment en condicions controlades per a minimitzar el fotodany.

En un altre estudi de la tesi, demostrem que el creixement bacterià es pot regular ajustant la humectabilitat de la superfície. El contrast amb els mètodes indirectes comunament utilitzats, com el recompte de colònies bacterianes i la microscòpia electrònica de rastreig, investiguem un enfocament directe per a l'avaluació. Primer, utilitzem simulacions de dinàmica molecular per a predir el comportament bacterià en substrats de vidre plans i nanoestructurats, amb característiques

d'humectació modulades a més de recobriments químics. Després avaluem experimentalment aquests resultats utilitzant bacteris, E. Coli, i microscòpia de fluorescència de lapse de temps. Les dades obtingudes confirmen que el vidre nanoestructurat simultàniament hidrofòbic, repel·leix l'aigua, i oleofilic, que atrau greixos, és el més destructiu, evitant l'adherència cel·lular i promovent la ruptura cel·lular total. Aquestes observacions directes demostren una evolució espacial i temporal més precisa que les interaccions i els efectes bactericides deguts a la morfologia de la superfície i la humectabilitat. Els resultats obtinguts proporcionen directrius per a dissenyar superfícies antimicrobianes utilitzant una simple nanoestructuració i química.

Acknowledgements

Throughout this thesis I have received a great deal of support, assistance, and advice.

My heroes and life counselors, my parents André and Joyce, for your love, affection, but also for conversations about wisdom, knowledge, and common sense. My brothers I'saï and Othniël who lovingly support me in everything I undertake, I thank you both and my parents for joining me from adventure to adventure, crossing borders in many ways to keep developing in every aspect of life. I am truly fortunate to have you as my family.

My loving Creator, I am convinced that the academic title Philosophiae Doctor "Doctor of Philosophy" or Teacher in "love of knowledge, pursuit of wisdom" (from the Latin and Greek philosophia) reflects Your attributes far more than mine. I am amazed to see how you made the vision you gave me on 13 January 2006, the day I handed in my career path plan during my studies in medical biology a reality in my own life. You guided me into the field of photonics (science and application of light) to learn that everything we perceive with our natural eyes truly comes from what is invisible to the unaided eye, i.e., everything we see is held together by electromagnetic forces, light as science has confirmed. My greatest gratitude is to You, for providing in everything to live a blessed life, everything meets completeness in its right time, thank you so much for making me part of Your story called: LIFE. For life comes from Light, and Light comes from You and You are true Love.
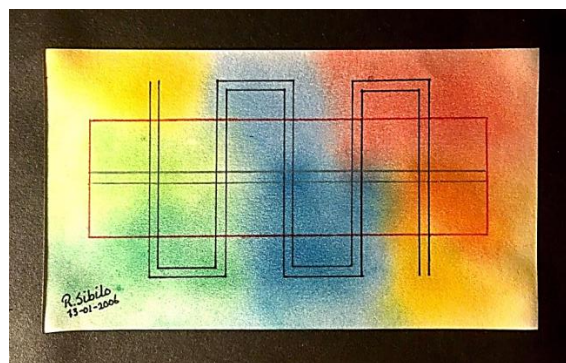
List of publications

1. "Imaging and detection of bacteria on a surface enhanced by an ultrathin metal quencher", **R. Sibilo**, J.M. Pérez Rosas, F. Tebbenjohanns, C. Hurth, N. Bareza, R.A. Maniyara, F. Campelo & V. Pruneri, *under preparation*.

2. "Direct and fast assessment of antimicrobial surface activity using molecular dynamics simulation and time-lapse imaging", **R. Sibilo**, I. Mannelli, R. Reigada, C. Manzo, M. A. Noyan, P. Mazumder, V. Pruneri, *Anal. Chem.* 92, 6795–6800 (2020).

3. "Surface cytometer for fluorescent detection and growth monitoring of bacteria over a large field-of-view", **R. Sibilo**, J. M. Pérez Rosas, C. Hurth, V. Pruneri, Biomed. *Opt. Express* 10, 2101 (2019).

Patents

1. "Optical device for detecting fluorescence emission", V. Pruneri, J.M. Pérez Rosas, **R. Sibilo**, C. Hurth, International patent application WO 2020161364, priority date 05/02/2019.

Contribution to conferences

1. "Active surfaces to modulate bacterial activity", **R. Sibilo**, I. Mannelli, R. Reigada, V. Finazzi, P. Mazumder, V. Pruneri, 6th International Conference on Multifunctional, Hybrid and Nanomaterials, Sitges, Spain, March 2019.

2. "Antimicrobial and biofilm preventing functionalised optical surfaces", **R. Sibilo**, I. Mannelli, M. A. Noyan, R. Reigada, P. Mazumder, M. Lakadamyali, V. Pruneri, 5th International Conference on Multifunctional, Hybrid and Nanomaterials, Lisbon, Portugal, March 2017.

3. "Multifunctional nano-structured optical surfaces for industrial applications", M. A. Noyan, K. K. Gopalan, R. A. Maniyara, M. M. Martin-Frances, V. Mkhitaryan, J. Rombaut Segarra, M. Rude, R. Sibilo, I. Mannelli, J. Canet Ferrer, V. Pruneri, Nanometa 2017, Seefeld, Austria, January 2017.

Table of contents

Nomenclature

AMR	Antimicrobial resistance
BG	Background
BSA	Bovine serum albumin
BW	Bandwidth
CA	Contact angle
CDC	Centers for Disease Control and Prevention
CFU	Colony forming unit
CG	Coarse-grained
CMOS	Complementary metal-oxide-semiconductor
CVD	Chemical vapor deposition
CWL	Central wavelength
DNA	Deoxyribonucleic acid
DOF	Depth of focus
eDNA	Extracellular DNA
ELISA	Enzyme-linked immunosorbent assays
EM	Electromagnetic
EMCCD	Electron-multiplying charged-coupled-device
EPS	Extracellular polymeric substance
FC	Fluorocarbon
FEG SEM	Field Emission Gun Scanning Electron Microscopy
FITC	Fluorescein isothiocyanate
FOV	Field-of-view
HAI	Hospital-acquired infection
HC	Hydrocarbon
HCAI	Healthcare-associated infection
HyD SMD	Hybrid single molecule detector
IAA	Image autocorrelation analysis
IAD	Ion assisted deposition
LED	Light- emitting diode
LOD	Limit of detection
NA	Numerical aperture
PI	Propidium iodide
POC	Point-of-care
PSF	Point-spread function
PVD	Physical vapor deposition
qPCR	Quantitative polymerase chain reaction
RF	Radio frequency
RIE	Reactive ion etching
RNA	Ribonucleic acid
SEM	Scanning electron microscopy
SERS	Surface-Enhanced Raman Spectroscopy
SMLM	Single molecule localization microscopy
SNR	Signal-to-noise ratio
TIRF	Total internal reflection fluorescence
TMM	Transfer matrix method
UTMQ	Ultrathin metal quencher
VMR	Variance-to-mean ratio
WHO	World Health Organization

List of figures

List of tables

Chapter 1: Introduction & state-of-the –art

The fascinating world around us can be observed with the unaided eye. Our curiosity and eagerness to learn and understand how the different components synergistically and dynamically function, inspire us to build devices to study them in greater detail. Whether they are telescopes to study stars and galaxies or simply our eyes that analyze structure, geometry, and color of flowers, animals and so forth, they all enchant us in some way. Yet, when we move from this macro world and dive into the micron and sub-micron nature of life, a wealth of new discoveries await us. However, as objects of these sizes are often too small to be observed with the unaided eye, one needs to think of clever ways to visualize, measure, and analyze them. It was in the seventeenth century when the Dutch pioneering microscopist, Antoni van Leeuwenhoek (1632-1723) tweaked his tiny microscope to get his objects into focus and what he saw must have intrigued him. In front of his eyes he saw little moving creatures which he coined "animalcules", or microorganism as we know them today.[1,2] His contemporary microscopist, Robert Hooke (1635-1703), an English physicist, verified much of his work and he himself was the first to use the term "cells" when studying cork, in his publication Micrographia in 1665.[3] In more modern times, Dutch Professor Ploem (1927 -) was the first to develop a four-wavelength vertical fluorescence illuminator to excite with a narrow-band of ultraviolet, violet, blue or green light. This four wavelength epi-illumination system was first commercialized by Leica under the name "Ploem-opak" (figure 1.1). A principle we currently use in the lab and for the experiments in this thesis.[4] Present-day technology has allowed us to study life at an even smaller scale arriving at atoms and sub-atomic particles that are held together by electromagnetic radiation or light. Everything we see around us is ultimately made up of particles that from matter which are held together by electromagnetic forces. Or as Griffiths writes in his book '*Introduction to electrodynamics*': "Indeed, it is scarcely an exaggeration to say that we live in an electromagnetic world-for virtually every force we experience in everyday life, with the exception of gravity, is electromagnetic in origin."[5]
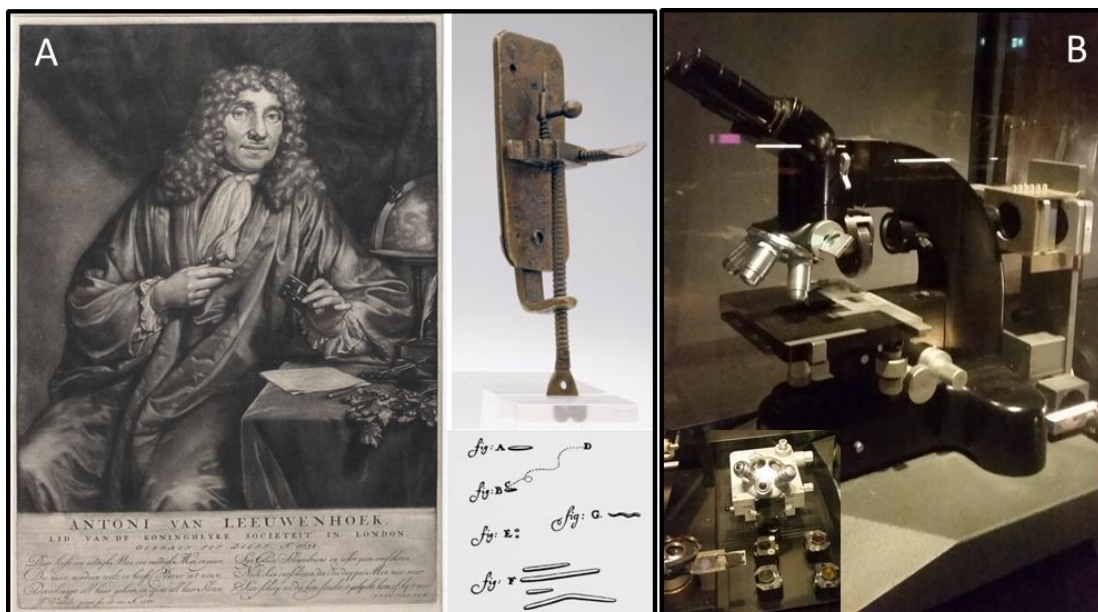
Figure 1.1. A. Antoni van Leeuwenhoek, his microscope and the microbes he drew. B. Epi-fluorescence microscope. Fluorescence multi-wavelength epi-illuminator with four dichroic beam-splitters. (Ploem, 1965). Developed with Leitz respectively, Leica Wetzlar.

From a physics point-of-view, light spans the entire electromagnetic (EM) spectrum from gamma rays to radio waves and is a form of energy.[6] However, more general light is described as the visible radiant energy of the EM spectrum, roughly ranging between 400 – 700 nm to which the human eye is sensitive but more recently the range from 310 nm in the ultraviolet to 1100 in the near-infrared has been proposed to be more accurate.[6,7] Light described as a an EM wave possesses a specific amplitude that dictates its brightness while its wavelength the color. We see objects because light interacts with matter, causing processes such as reflection, refraction, diffraction, and absorption all to occur at the same time with mostly one process dominating.[6,7] These considerations are important in our optical studies of bacteria.

1.1. Societal need for early detection of microorganisms and the problem with antibiotics

Microbes can attach to biotic and abiotic surfaces, proliferate and together with non-microbial matter form biofilms causing adverse effects. Especially in the medical field this does not only lead to failure of lenses, dental or medical implants but also to infection and disease spread.[8,9,10,11] Reports on hospital-acquired infections (HAI) have stated that surfaces can serve as reservoirs for pathogens that can be transmitted via touching.[12,13] In the marine industry biofilms increase drag, bio-corrosion of the metal, and fuel consumption.[14,15,16,17] Furthermore, industries related to food and potable need to constrain bacterial growth depending on the product produced to prevent foodborne diseases.[15,18]

According to a 2016 report published by the Review on Antimicrobial Resistance (AMR), AMR drugs are medicines that are active against a range of infections caused by bacteria (antibiotics), viruses (antivirals), fungi (antifungals) and parasites (including antimalarials).[19] Microbial resistance to drug treatments is a primary concern in choosing an effective therapy for patients with persistent infections which are often not only precarious and costly but they also increase the risk of disease spread and sometimes remain present for life.[20,21,22] In Europe alone, bacterial resistance claims around 33.000 lives and is predicted to reach around 10 million cases worldwide by 2050.[23] The U.S. Centers for Disease Control and Prevention (CDC) reports that yearly over 2.8 million antibiotic-resistant infections lead to more than 35.000 lethal cases.[24] In figure 1.2A several frequently occurring causes of death are compared with antimicrobial resistance. The World Health Organization (WHO) promotes global effort to approach this serious concern by bringing awareness, exchange knowledge, and define a plan of action.[25] National and international initiatives to combat AMR have been taken, including political declarations, international initiatives, partnerships to fund research and development,[26] building a One Health Learning Platform[23] and monitoring health-related issues as proposed by the European Observatory on Health Systems and Policies.[27]

Figure 1.2B depicts a timeline that indicates when different types of antibiotics came in use and in what time frame microbial resistance was developed against them. Especially, in the last 40 years new clinically-relevant classes antibiotics are lacking which is a huge concern as around 70% of patients with HAI are resistant to 1 or more types of antibiotics.[28] Depending on the type of antibiotics, different bacterial functions are targeted such as inhibiting of cell wall synthesis, protein synthesis, deoxyribonucleic acid (DNA) replication or ribonucleic acid (RNA) transcription.[28]

Antibiotics can be either bactericidal, i.e., have the ability to kill or they can be bacteriostatic meaning that they inhibit growth but as fewer options are left out, alternative ways are needed to reduce the risk of contamination and disease spread such as antimicrobial surface research that investigates how to prevent and constrain bacterial cell growth.
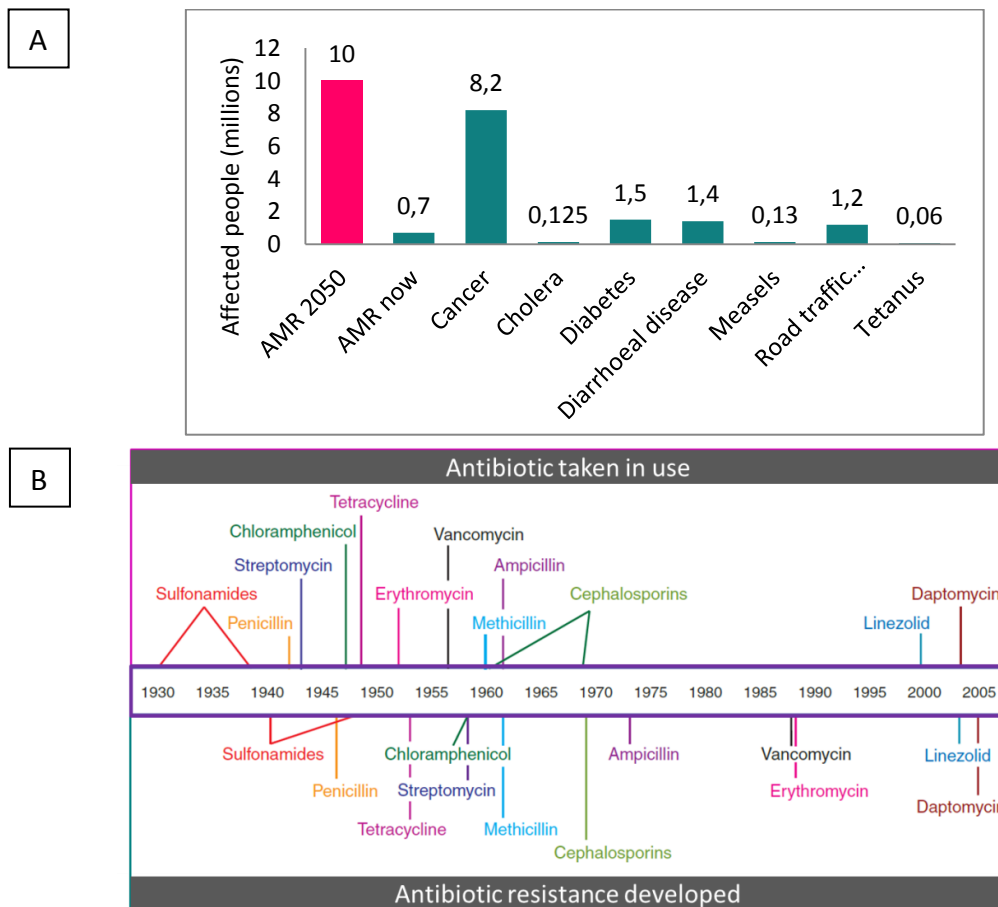
Figure 1.2. Antibiotics and antimicrobial resistance. A. Predicted antimicrobial resistance (AMR) by 2050 in relation to other frequently occurring causes of death worldwide.[29] B. Timeline of antibiotics taken in use and onset of resistance developed against them (figure adapted).[28]

1.2. Bacteria-surface interactions from bulk liquid to surface adherence developing into biofilm

Bacteria as freely floating single cells are called planktonic. Their journey from bulk liquid to an abiotic surface depends on environmental cues (chemotaxis) that induce genetic changes favoring adherence but also on movement, that can be passive and/or active. Passive movement is governed by Brownian motion, which becomes more circular in proximity of the surface, and gravitational forces while active transport involves bacterial flagella for directional movement towards the surface.[30,31,32] Single-cell adhesion to the surface is a result of the interplay of physical, chemical, and biological processes that are determined by the properties of the bacterial cells, the surface, and the surrounding medium.[30,33] Upon successful adherence of a cell to the surface, the bacterium produces extracellular polymeric substance (EPS) that mediates firmer attachment and promotes a sessile lifestyle as a microbial community by forming a biofilm. The organization in a biofilm is a continuous and highly dynamic process that undergoes spatial rearrangements in time.

Conventionally, cell attachment to surfaces is considered to take place in two stages. The initial attachment takes place in the order of about a minute and is reversible because planktonic cells in proximity of a surface experience non-specific weak long-range forces such as van der Waals forces (attractive) and electrostatic (repulsive) forces which depend on the local pH and osmolarity. The interplay between these forces ultimately determines whether a bacterium adheres to the surface or not. However, shear forces can easily cause bacterial detachment. Once adherence is established, the process enters into the next stage of irreversible attachment which requires several hours. This stage involves stronger forces such as hydrogen bonding, covalent bonding, hydrophobic in combination with cellular appendages (adhesins) such as flagella, pili, fimbriae, and curli fibres that serve as anchorage to surfaces.[30,33,34,35] Moreover, signaling known as quorum sensing enhances the negative charge of bacteria that facilitates surface attachment.[36] Proximity of bacteria not only causes changes in pH, osmolarity, and flagellar rotation but also acid-base hydrophobic interactions can be attractive or repulsive depending on the environment. Surface topography and the bacterial polymeric brush (biopolymers on their surface) influence attachment through steric hindrance, the long polysaccharide chains can overcome them by generating long-range steric forces. To summarize, adhesion is a sum of attractive and repulsive forces, attachment is facilitated by bacterial adhesion molecules and bacterial adhesion is further influenced by surface topography and surface chemistry.

In our work we have used *Escherichia coli* (*E.coli*) bacteria, a well-studied model bacterium commonly used in laboratories around the world. *E.coli* is a rod-shaped Gram-negative bacterium, which signifies that the bacterium possesses a cytoplasmic as well as an outer membrane with in addition to phospholipids in its outer membrane it also contains lipopolysaccharides (LPS).[37] To be more descriptive, approximate numbers will be given of what is currently known about *E.coli* bacteria. One bacterial cell is around 2 µm long and 1.5 µm in diameter, has a cell volume of 1 µm^3, a dry mass of 1 pg, a division time of 3000 s, a surface area of 6 µm^2, has genome length of 5 x 10^6 base pairs and can swim at a speed of 20 µm/s.[38]

Biofilm formation on surfaces is generally described by several stages (figure 1.3):

1. A single planktonic bacterial cell from a liquid, reversibly adheres to an abiotic surface.
2. Once the bacterial cell irreversibly adhered to the surface, it produces a sugar-based coating called extracellular polymeric substance (EPS) for protection and facilitating strong cell-surface adhesion. It multiplies and together with other microbes assembles to form a biofilm.
3. The initial biofilm matures and creates a balanced local microbial environment based on the availability of nutrition, space and resources.
4. Cells that turned into their planktonic state disperse from the biofilm and freely float to repeat the process.
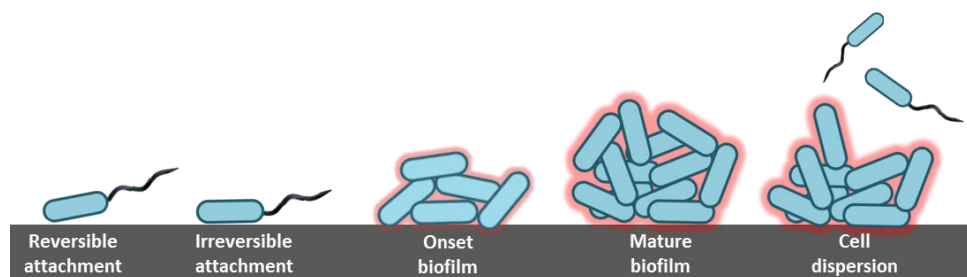
Figure 1.3. Stages in biofilm formation.

1.3.   Bacteria fight back - Antibiotic resistance development and bacterial antagonism

Though microorganisms need to be tightly controlled under certain circumstances, we should not forget that they are ubiquitous and vital to sustain life. Bacteria live in complex communities to survive, replicate and compete for their own space (niche). In their own local ecological space they their competition with other can be exploitative by consuming resources of others or interference where they inhibit growth of others. A developing research branch studies bacterial antagonism and their way to maintain an ecological balance to understand how microbiota develop within a host and contribute to health and disease. The local habitat of microbes with the physio-chemical processes and their so called 'theatre of activities' form a specific ecological niche called a microbiome. Microbiota on the other hand encompass microorganisms of different kingdoms such as prokaryotes (bacteria, archaea) and eukaryotes (fungi and algae), together with their 'theatre' which involves mobile genetic elements such as viruses, transposons, and phages, metabolites and relic DNA from the environment. To protect themselves against mechanical damage, they compete and collaborate with one another but reach a stable configuration over time.[39,40,41]

Bacteria can resist drug through enzymes and the transportation path. Moreover, obtained drug resistance can be transmitted to fellow bacteria through plasmids, bacteriophages, 'free' DNA, and transposons.[42] When antibiotics are used, they kill off both good and pathogenic bacteria. When some bacteria survive, they proliferate and become more dominant, making it harder to fight them. Figure 1.4 summarizes the process of bacteria acquiring resistance, spreading resistance genes, and applying mechanisms to fight antibiotics. Interestingly, it was the Scottish physician and microbiologist Alexander Flemming, the discoverer of penicillin produced by mold, who during his Nobel Lecture on 11 December 1945 warned that easy access and uncontrolled use of this antibiotic could induce resistance in bacteria and would no longer function for another individual.[43]

A Antibiotic-resistant mechanism

Some bacteria may be resistant to antibiotics. Microbial communities are diverse and antagonistic.

Antibiotics kill both good- and infection-causing bacteria.

Antibiotic-resistant bacteria proliferate and dominate.

Normal bacterium

Resistant bacterium

Dead bacterium
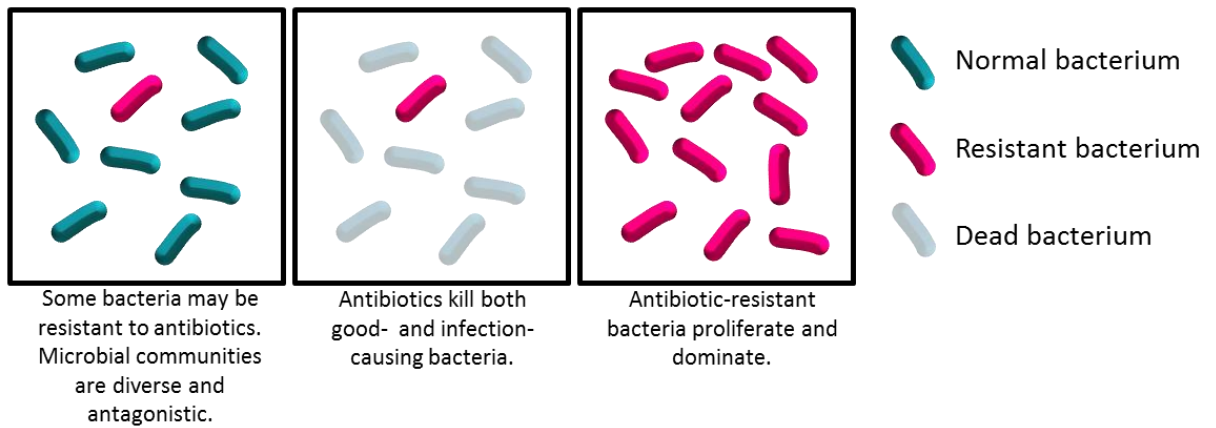
B Spreading of drug resistance
through, plasmids, bacteriophages, transposons, and naked DNA.
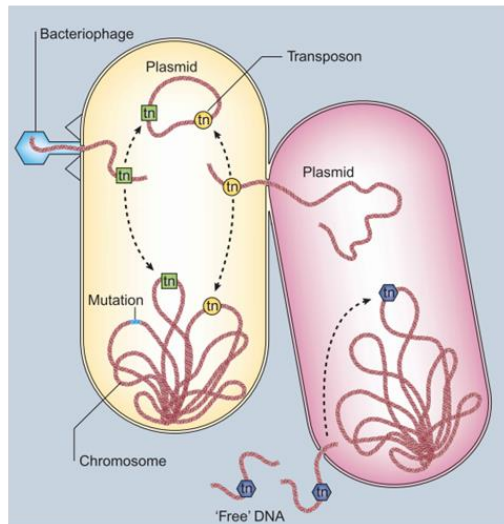
C Antibiotic resistance mechanisms
by genes in plasmids, enzymes, efflux pump.
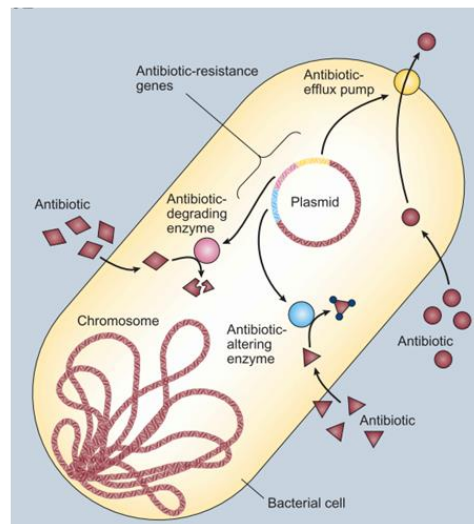
Figure 1.4. Resistance in bacteria. A. Antibiotic resistance mechanism where bacteria unaffected by drugs are not killed, proliferate, and take over. B. Processes through which drug resistance spreads, bacteriophages which are viruses that insert genetic material, plasmids are circular genetic material, transposons are jumping genes or pieces of DNA that can change position within the genome, or naked DNA which releases when surrounding cells burst.[21] C. Bacterial mechanisms to fight antibiotic drugs by acquired antibiotic genes in plasmids, efflux pump to remove drugs from the internal environment, enzymes that degrade or alter an antibiotic.[21]

1.4. Fluorescence and fluophores

An atom is considered to be in its ground state when it exists in a stable configuration with its electron orbitals (regions within the atom with the highest probability to be found) in their lowest possible state. This profoundly changes upon collision with other atoms, electrons or photons that cause transition to other specific configurations, i.e., higher energy levels. Thus, when a photon impinges upon an atom's valence electron with an energy that matches to make an energy jump (resonant frequency), the atom undergoes a rapid transition in the order of femtoseconds (10^{-15}) from its ground state orbital to one of the well-defined excited states. This excited state of the atom is a transient resonance phenomenon of about $10^{-8} - 10^{-9}$ s after which the atom spontaneously relaxes back to its ground state while dissipating its excitation energy.[44] This redistribution of energy occurs through light emission or conversion to thermal energy which stems from interatomic collision within the medium. The latter lies at the basis of light absorption at resonant frequency, while the remaining frequencies are linked to transmission and reflection. These outlined physical mechanisms are the basis for fluorescence light emission by fluorescent molecules (fluophores).[44]

When a fluophore absorbs light in the form of photons, it transitions from its ground state (S_0) to an excited state (S_1, S_2). Energy is rearranged through different processes that occur and as a consequence this shifts the emission of light to a longer wavelength, called a Stokes shift. Light emission occurs through fluorescence or phosphorescence depending on their configuration in the excited state because electrons come in pairs with opposite spins + ½ spin and − ½ spin. In the case of fluorescence, the electron in the excited orbital of the singlet state has an opposite spin from its counterpart electron in the ground state orbital. This return to the ground state is allowed and a photon is emitted. The typical emission rate or fluorescence lifetime (τ) is in the nanoseconds. Phosphorescence on the other hand emits light from a different excited state called the triplet state, where the electron in the excited orbital has the same spin orientation as the electron in the ground state orbital, thus return to the ground state is said to be 'forbidden' and produces low emission rates in the order of milliseconds to seconds. The Jablonski diagram in figure 1.5 summarizes the occurring processes. [44,45]
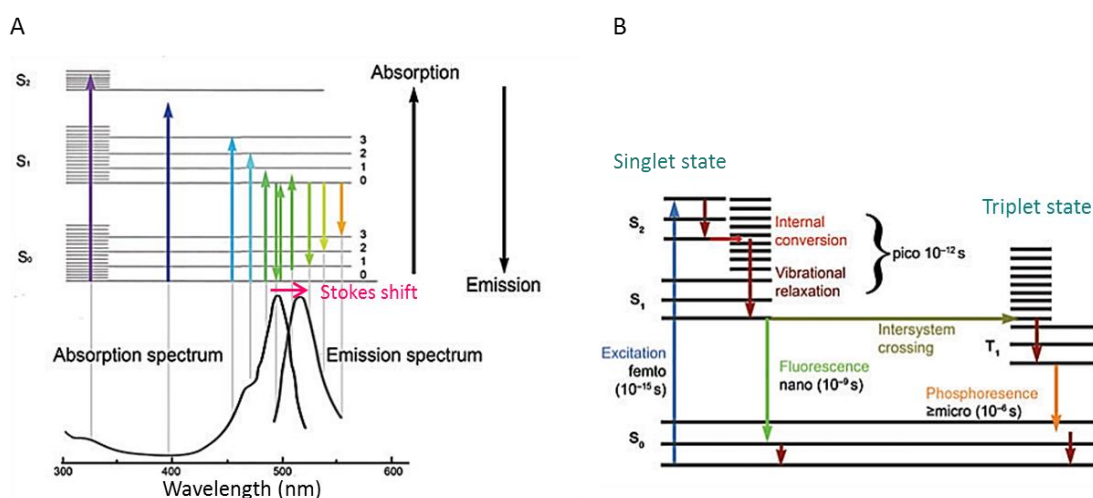
Figure 1.5. Jablonski diagram. A. Light absorption process causing a molecule to transition to an excited singlet state (S_1, S_2) and the Stokes-shifted emission. B. The chief processes that occur after excitation with light and the corresponding time scales.

1.5.   Experimental toolbox to engineer and assess surfaces – equipment at ICFO premises

This section describes several key devices together with their working principle that were used in this thesis to fabricate surfaces with thins films, determine surface wetting characters, and perform imaging.

Reactive ion etching

The wettability of a surface can be altered by nanostructuring rendering it more hydrophilic or hydrophobic depending on successive procedures and we achieved this increased surface area by reactive ion etching (RIE). In RIE a combination of chemical and physical reactions directionally etches a substrate. This highly anisotropic etching process takes place in a vacuum chamber consisting of two electrodes. The top electrode is positively charged while the bottom electrode, on which the target substrate is placed, is negatively charged. When a gas is introduced into the chamber, a strong radio frequency (RF) electric field in between the electrodes ionizes the gas molecules by removing electrons from them, creating a plasma. The high energy positively-charged ions from the plasma accelerate towards the negatively-biased surface and attack (ion bombarding) and react with it. The ions are able to break chemical bonds of atoms in the substrate and coincidently reduce the activation energy so that chemical etching can occur, increasing the reactions rates.   The combination of directional ion bombardment with the high etch rates due to chemically active species is highly directional in the vertical direction resulting in well-defined surface profiles.[46] At ICFO's nanofabrication laboratory we use the reactive ion etcher Plasmalab System 100 by Oxford Instruments depicted in figure 1.6A.

Scanning electron microscopy

For surface morphology characterization after nanostructuring, we used scanning electron microscopy (SEM) as depicted in figure 1.6B. SEM is a widely used imaging method that produces images at high resolution down to 1 nm. In the SEM configuration an electron gun produces electrons of 0-40 kV which are bundled into a beam by several electromagnetic condenser lenses that turn the electron beam into a fine probe that is raster-scanned across a specimen. The interaction of the electron with the specimen produces secondary electrons, back-scattered electrons, Auger electrons and x-rays that are detected and images are displayed unto a monitor. SEM allows one to obtain high resolution three-dimensional images that provide information on the morphology, surface topography, chemical composition and electrical behavior of a specimen under vacuum and thus samples are non-living.[47]
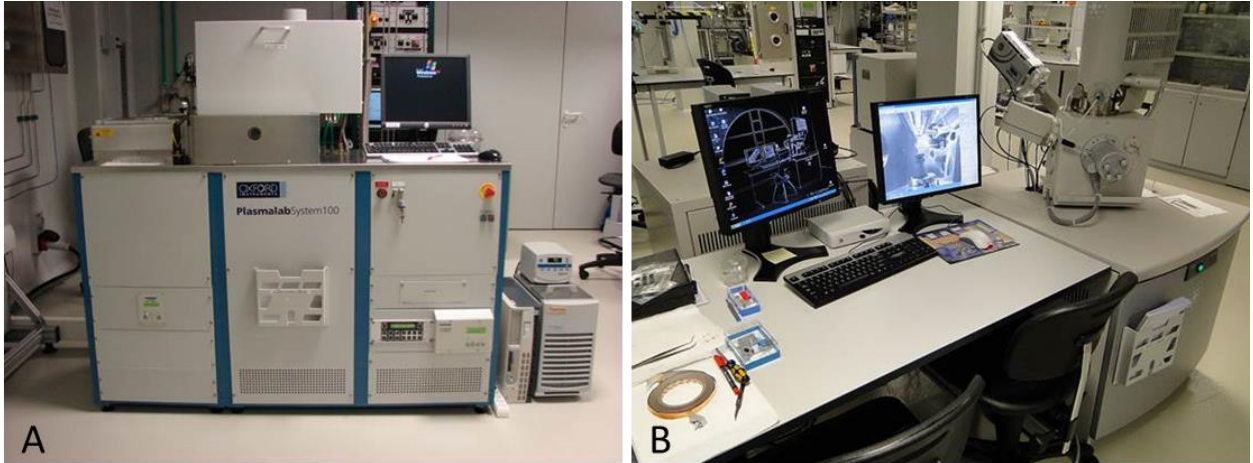
Figure 1.6. A. Reactive ion etcher Plasmalab System 100 by Oxford Instruments. B. Scanning electron microscope FEG-SEM, Inspect F, FEI Systems in the Nanofabrication lab at ICFO.

Thin film deposition

Metals and dielectric materials can be deposited on a substrate by either chemical vapor deposition (CVD) or physical vapor deposition (PVD) forming very thin layers of material ranging from Ångström to micrometer thickness. In the CVD process, precursors adsorbed on a substrate chemically react and form a thin layer of material. In PVD, thins films are deposited on substrates via physical processes such as evaporation or sputtering. In sputtering plasma produces ion bombardment as described in RIE, creating vapor from the source material. In general, thin films are formed by the interplay between thermodynamics and kinetics. Once atoms from the gaseous phase arrive at the surface and successfully adsorb unto the surface it can combine with other atoms and grow larger clusters over time.[48] For the production of ultrathin gold films we used thermal evaporation which simply heats up a solid source material in a high vacuum chamber so that it vaporises and subsequently redeposits on another substrate. In figure 1.7 the Lesker LAB18 evaporator that was used for this work.

Figure 1.7. Lesker LAB18 evaporator in the Nanofabrication laboratory at ICFO.

Contact angle measurement

Cohesive forces that exist between the same type of molecules, such as water molecules, cause the surface of a liquid to minimize its surface area, a phenomenon that is called surface tension. Surface wettability is a measure of how surface energy influences the degree of contact with a surface and is measured through a droplet between different interfaces. Young's equation considers a force balance of lateral forces and is commonly used to describe the relationship of a drop's equilibrium contact angle (θ_{eq}) with the surface and the three interfacial tensions (Υ), solid-liquid, liquid-gas, and solid-gas: [49,50]

$$\gamma_{SG} = \gamma_{SL} + \gamma_{LG}\ \cos\theta_{eq}$$
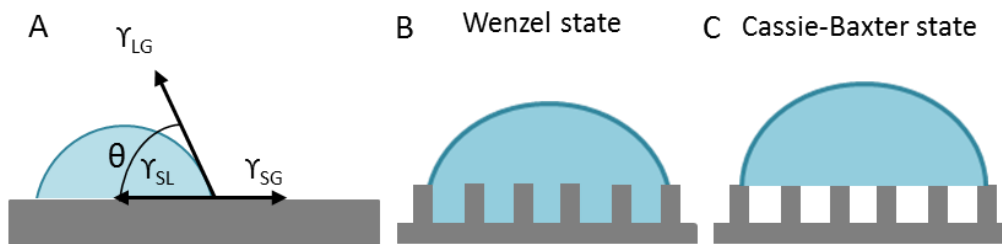
Figure 1.8. Wetting on surfaces. A. Drop on flat surfaces with contact angle θ and three surface tensions indicated. B. Wenzel configuration on rough surface, showing full wetting. C. Cassie-Baxter configuration on rough surface showing air pockets and no wetting.

Wetting of rough surfaces is generally described by two modes. The Wenzel mode refers to complete wetting while the Cassie-Baxter mode represents no wetting (figure 1.8). More recently, a third configuration of intermediate wetting based on the thermodynamic energy minimization method has been proposed, where the drop partially enters in between the surface structures.[51] Table 1.1 is indicative for the different degrees of wetting and their corresponding ranges of contact angles. We carried out experimental work with a Krüss GmbH DSA100 drop shape analyser (figure 1.9A), its software calculates the where the three phases, solid, liquid, and gas intersect. In practice one can observe that a water drop on a hydrophobic (water repellent) surface minimizes its contact with the surface resulting in a high contact angle while its simultaneously oleophilic (fat attracting) character allows a hexadecane (oil) drop to maximize balanced wetting providing a low contact angle as seen in figure 1.9B.

Table 1.1. Wetting classification and corresponding water contact angle range.

Classification	Water contact angle (θ)
Superhydrophilic	$\theta << 10°$
Hydrophilic	$10° < \theta < 90°$
Hydrophobic	$90° {}^{<} \theta < 150°$
Superhydrophobic	$150° < \theta < 180°$
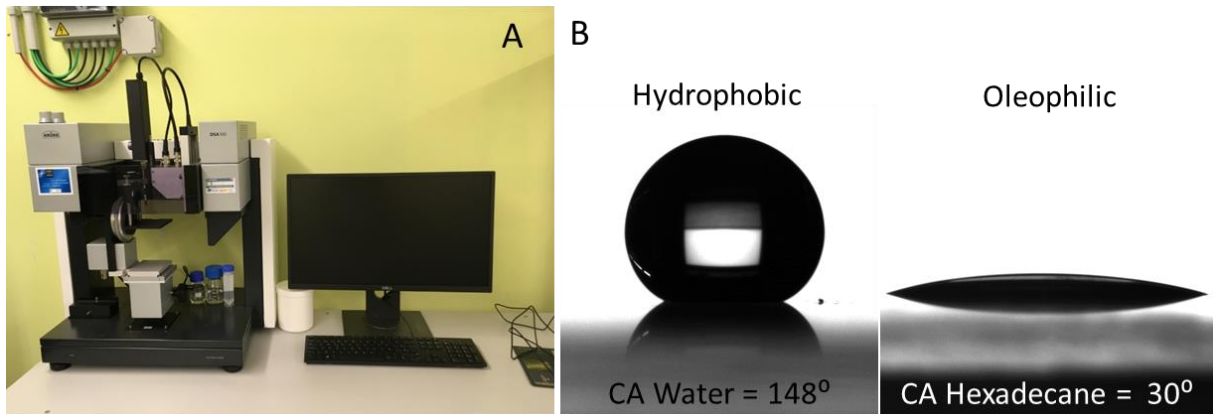
Figure 1.9. A. Krüss GmbH DSA100 drop shape analyser in the Corning laboratory at ICFO. B. Photo examples of contact angle measurements with water and oil (hexadecane) showing wetting properties of the surface, hydrophobic and oleophilic.

Fluorescence microscopy

Live cell imaging experiments were perfomed with a commercial Nikon inverted fluorescence microscope (Nikon Eclipse T*i*) using a 100x Plan-Achromat oil immersion objective (NA 1.49). Light excitation and emission was done through the microscope objective. Emitted light was filtered by a quad-band filter cube (LF405/488/561/635-A-NTE) and collected by an electron-multiplying charged-coupled-device (EMCCD) camera. The microscope was used in total internal reflection (TIRF) mode and thus alternatively referred to as TIRF microscopy in this thesis (figure 1.10). TIRF utilizes a confined electric field in the form of an evanescent wave to excite specimen in immediate proximity of the surface or more precisely at the interface of two media possessing different refractive indices. TIRF efficiently excites fluophores within about the first 100 nm from the surface with the advantages of low background fluorescence and minimal out-of-focus signals.[52]

Figure 1.10. Nikon inverted fluorescence microscope (Nikon Eclipse T*i*) in the NSTORM laboratory of the super-resolution and nanoscopy laboratory at ICFO.

1.6. Thesis objectives

The overall objective of the thesis is to study the interaction and optical properties of bacteria on surfaces and, in this way, contribute to the field of antimicrobial resistance. More specifically, it investigates novel methods for enhanced bacteria detection, growth monitoring and presents an in-depth study of interaction mechanisms of bacteria and surface nano-structures.

The specific objectives include:

1. **Monitoring bacterial growth over time.** This by implementing an in-house built large field-of-view optical surface detection system measuring fluorescence.
2. **Enhancing imaging and microscopy of bacteria.** This by using ultrathin metal films for quenching background fluorescence on a surface, in this way achieving a more accurate localization of cells.
3. **Engineering glass surfaces for antimicrobial activity.** This by either avoiding adherence or killing upon attachment, with molecular dynamics simulations to predict bacterial behavior and time-lapse fluorescence microscopy for direct observation.

1.7. Thesis outline

This thesis is organized in 5 Chapters as follows:

After the introduction (**Chapter 1**), in **Chapter 2** we describe a novel in-house built sensing technology, a surface cytometer, which measures average fluorescence intensity from a surface, proportional to the number of bacteria present. The device was tested and validated against established laboratory techniques such as absorbance and scattering measurements as well as fluorescence microscopy to quantify cell growth. The generated bacterial growth curves allowed us to compare and contrast the advantages and limitations of the three techniques. The results confirm the applicability of surface cytometer as a rapid, compact, and cost-effective device to measure bacterial growth.

Chapter 3 describes a new type of surface that is capable of quenching background fluorescence in microscopy, hence, improve the signal-to-noise ratio in the digital images. The surface is transparent, electrically conductive and its prototypical form is composed of glass with an ultrathin (<10nm) gold film. Numerical calculations provide information on the distance-dependent lifetime of a fluophore in proximity of such surface. Experiments further corroborate its suitability for commonly used specimen in biophysics studies such as microspheres, bacteria, and proteins. As the substrate can be used in air and liquid, it can provide new ways for improved imaging of single molecules and living cells, as more photons can be collected at lower laser powers and shorter acquisition times.

Chapter 4 centralizes on surface wettability as an important factor that influences bacterial adhesion and proliferation. The interaction of bacteria with surfaces possessing different degrees of wettability was studied through molecular dynamics simulations in combination with time-lapse fluorescence microscopy. In contrast to commonly indirect methods, our direct observations of bacteria-surface interactions provide a more accurate analysis of spatial evolutions over time. Surface nanostructuring enhances the hydrophobic and oleophilic character of the surface and avoids bacterial cell adherence. The results provide better understanding of molecular- and cell evolution during these interaction and guidelines to design surfaces that constrain bacterial growth.

The final chapter (**Chapter 5**) of the thesis summarizes the main findings and provides an outlook on future implementations towards real-life applications.

Chapter 2: A large-scale detection of bacterial cell growth on surfaces

The content of this chapter has been adapted and paraphrased under the terms of the Creative Commons Attribution Non-commercial license, from the original publication:

Sibilo, R, Pérez, JM, Tebbenjohanns, F, Hurth, C, & Pruneri, V 2019, `Surface cytometer for fluorescent detection and growth monitoring of bacteria over large field-of-view', *Biomedical Optics Express*, vol. 10, no. 4, pp. 2101-2116.

When pathogenic microbes adhere to surfaces and proliferate, they can form biofilms and cause adverse effects in clinical settings, water systems as well as in the food and beverage industry. Therefore, early, rapid, and accurate detection of microbial contamination is essential. Ideally, devices and biosensors used for microbial detection should be fast, compact, low-cost and require minimal training of personnel in particular, for point-of-care (POC) i.e. rapid bedside testing applications.[53,54]

The aim of the work contained in this chapter was to test an in-house developed low-cost and portable sensing device to detect cells on surfaces and monitor growth. Validation was conducted by generating a bacterial growth curve with the surface cytometer and benchmark it against the growth curves obtained from fluorescence microscopy and spectrophotometry. The three techniques reveal a similar trend demonstrating its applicability for monitoring cell growth on surfaces. The surface cytometer technology incorporates off-the shelf optical components such as a light- emitting diode (LED) as the light source and a complementary metal-oxide-semiconductor (CMOS) as the image sensor. Distinct advantages are its detection range with a large field-of-view (FOV) of ~200 mm^2 and a large depth of focus (DOF) ~2mm. Furthermore, no complex post-processing is required, the limit of detection (LOD) is ~10^4 cells/mm^2 and falls in a commercially competitive range with an acquisition time less than 1 min per frame. A visual summary of the work is depicted in the mind map of figure 2.1.

Aim: Surface cytometer (S-CYT) validation
- Device characteristics:
  - Large field-of-view (FOV)
  - Large depth of field (DOF)
  - Limit-of detection (LOD) ~10^4 cells/mm2
  - Light-emitting diode (LED) light source
  - Complementary metal-oxide-semiconductor (CMOS) image sensor
  - Direct method, no complex post-processing
  - Portable, compact, inexpensive
- Benchmark against
  - Spectrophotometry — Absorbance measurements
  - Fluorescence microscopy — Cell counting

Prediction
- Proof of concept in laboratory setting

Equipment
- S-CYT — FOV ~200 mm2, DOF 2-3 mm
- fluorescence microscope — FOV < 20 mm, DOF < 30 µm
- Spectrophotometer — Optical beam = 2 mm, Optical path length = 10 mm
- Incubator for bacteria
- Software for analysis (Fiji)

Fair Test
- How ?
  - Growth cycle
    - Lag phase (adaptation)
    - Exponential phase (exponential growth)
    - Stationary phase (similar rate growth and death)
  - Compare bacterial growth curves
    - S-CYT
    - Fluorescence microscope
    - Spectrophotometer (reference curve)
- Why ?
  - Benchmark
  - Competitive with current devices?

Method
- Grow bacteria from lag phase to stationary phase
- Collected 3 samples at different time intervals
- Sample 1: Reference curve based on optical density measurements (1 ml cuvet)
- Sample 2: S-CYT measurement in volume + analysis
  - Fluorescently stain E.coli and measure
- Sample 3: Fluorescence microscopy glass substrate
  - Acquire images
  - Analyze average fluorescence
  - Acquire images
  - Particle analysis for cell count

Result
- Bacterial growth curve
  - S-CYT similar to spectrophotometer
  - Microscopy similar growth trend but fewer cells due to surface and small FOV

Conclusion
- S-CYT growth curve agrees with reference curve
- Results S-CYT competitive with commercial devices

Evaluation
- Strengths
  - Fast, greater FOV & DOF compared to microscopy
  - portable, compact, easy post-processing
- Weaknesses
  - Collect enough sample
  - Microbial specificity
  - Further research to use in real life setting

Central image labels: 0 min, 292 min

Large-scale view on bacterial growth

Figure 2.1. Mind map chapter 2. A large-scale detection of bacterial cell growth on surfaces.

2.1. State-of-the-art and overall objective

Microbial contamination and proliferation are undesired in various industries. In healthcare, pathogens increase the risk of spreading infection, cause failure of orthopaedic- and dental implants, while food- and drinking water industries regulate microbial growth to avoid food poison and disease transmittance, respectively.[55,9,56,57] Detecting the early onset of bacterial contamination is important because once they have colonized a local environment and formed biofilms their presence becomes persistent, complex, and hard to eliminate.[58,35] There are several techniques that are commonly used in laboratories to identify and quantify microbes.[53,56] Colony forming unit (CFU) counting is time-consuming, can form aggregates which are hard to count, and only detects microbes that readily grow on a solid medium.[59] Quantitative polymerase chain reaction (qPCR) is highly specific and sensitive but requires prior sequencing of the target genes and can cause overestimation in presence of free extracellular DNA (eDNA).[53] Microscopy imaging analysis is a direct method but does not distinguish well between the type of bacteria unless an appropriate dye is chosen.[56] Immunological assays such as enzyme-linked immunosorbent assays (ELISA) are rapid, high throughput, and precisely quantify microorganism but lack sensitivity and selectivity and thus are used in combination with other techniques such as colorimetric approach.[56,60] Generally, these techniques are not rapid and require trained personnel. To detect and quantify microbes rapidly, on site and in real-time, many innovative biosensors have been proposed. They fall in different categories such as mechanical, electrical, optical, chemical or a combination[56,60,61] of these as portrayed in figure 2.2, each with their distinct advantages. Additionally, they are designed to be sensitive, specific, cost-effective and portable.[62]
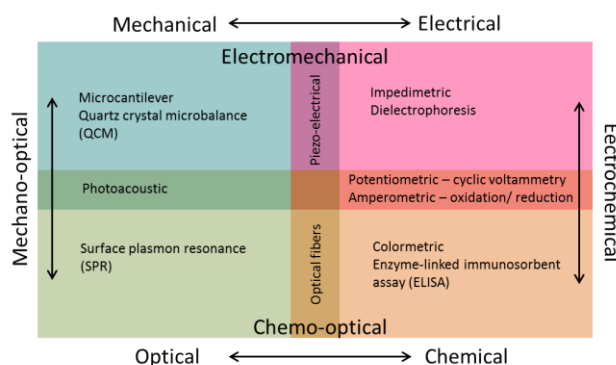
Figure 2.2. Categories of biosensors based on their detection and signal transduction method. Modified.[61]

Biosensors electronically detect and transmit signals based on changes of the biological component. Several microbiological detection markers include nucleic acids, proteins, adenosine triphosphate, immunological components, antigens or metabolic products.[56,18] Reported magnetoelastic biosensors detect pathogens directly on fresh food, in situ and in real-time but require a somewhat complex and costly sensor fabrication.[63] While electrochemical sensors on the one hand are cost-effective, their sensors need to be functionalized reach competitive LOD values in the order of 10^2 cells/ml.[64]

Surface-Enhanced Raman Spectroscopy (SERS) sensors are highly specific and versatile with single-molecule sensitivity but surface fabrication, sample transport, and trained personnel limit their applicability.[65,66] Optical biosensors are widely studied and applied because they offer rapid detection, are portable, multiplexed, and low-cost.[66]

2.2. Technology description of the surface cytometer

Figure 2.3 portrays the main optical components of the surface cytometer alongside the pathway the light rays travel from light source to image sensor. Its total dimensions are 20 cm x 20 cm, 10 cm and encompasses four main units, a light source, an optomechanical assembly, an image sensor, and controlling electronics. The light source unit is composed of a free space high power light-emitting diode (LED) (M470L3, Thorlabs, GmbH) in combination with an interference filter to achieve a cutoff bandwidth (BW) of 40 nm with a central wavelength (CWL) of 466 nm (86-352, Edmund Optics Ltd.). The next unit incorporates a series of optical components, two lenses and two filters all secured in precision holders. The achromatic doublet lens (Thorlabs AC254-050-A) confines the light into the sample and possesses an antireflective coating selective for the visible wavelength range 400-700 nm having a focal length of about 49.6 mm at 470 nm. This lens works in sequence with two filters, an interference filter having a BW of 53 nm and a CW of 526 nm (87-241, Edmund Optics Ltd.) and a green color filter (46-053, Edmund Optics Ltd.) that together filter out the excitation wavelength while improving the SNR even though the peak transmission coefficient is only 70% for the latter. The image lens has a focal length of 6 mm, a manual focus adjuster and an iris (Navitar). Non-linear behavior nor excessive aberrations were expected since all lenses were handled according to their specified normal working conditions at room temperature and below damage treshold. A photodiode sensor (Thorlabs S120C) set at 470 nm was used to determine the power that reached the sample plane. The power after the excitation filter was 135.2 mW over 94 mm^2 that reduced to 0.750 mW over 1.13 mm^2 at the sample plane, corresponding to irradiances of 1.44 mW/mm^2 and 0.66 mW/mm^2, respectively. The discrepancy is due to the low collimation of the LED but offers sufficient sensitivity.

The third unit is a 4.6 mm CMOS-ISA image sensor (Sony IMX219) with 3280 x 2464 pixels also referred to as the Raspberry Pi camera module version 2. The FOV and spatial resolution were quatified with a positive 1951 USAF test chart (R3L1S4P, Thorlabs, GmbH). The test chart has defined elements that become increasinlgy smaller towards its center. The ability to see the separate lines within an element determines the resolving power of an optical device. For the surface cytometer this was corresponding to element 5 of group 4 with a resolution of 25.4 lines/mm or a spatial resolution of 39 µm with a FOV of 200 mm^2. The final unit encompasses controlling electronics. The CMOS sensor camera was controlled by Python software using the third party module (picamera). The CMOS sensor IMX219 is based on a Bayer filter configuration having 2 x 2 bordering pixels, one red, one blue, and two green pixels. Each capture is based on four two-dimensional arrays 1640 x 1232 pixels with 10 bits per pixel. The optimized acquisition settings were 100 ms exposure time for a nominal gain of 1.0 acquiring at 30 frames/s. A 2 s interval was allowed for gain stabilization. The electronic signal from each acquisition was processed by a small Raspberry Pi 3 Model B computer to produce a fluorescence count proportional to the fluorescence emission level of the sample. Then, in-house developed software based on Python 2.7.6 processed the obtained data and produced a fluorescent count corresponding to the number of bacteria in an area of 200 mm^2.
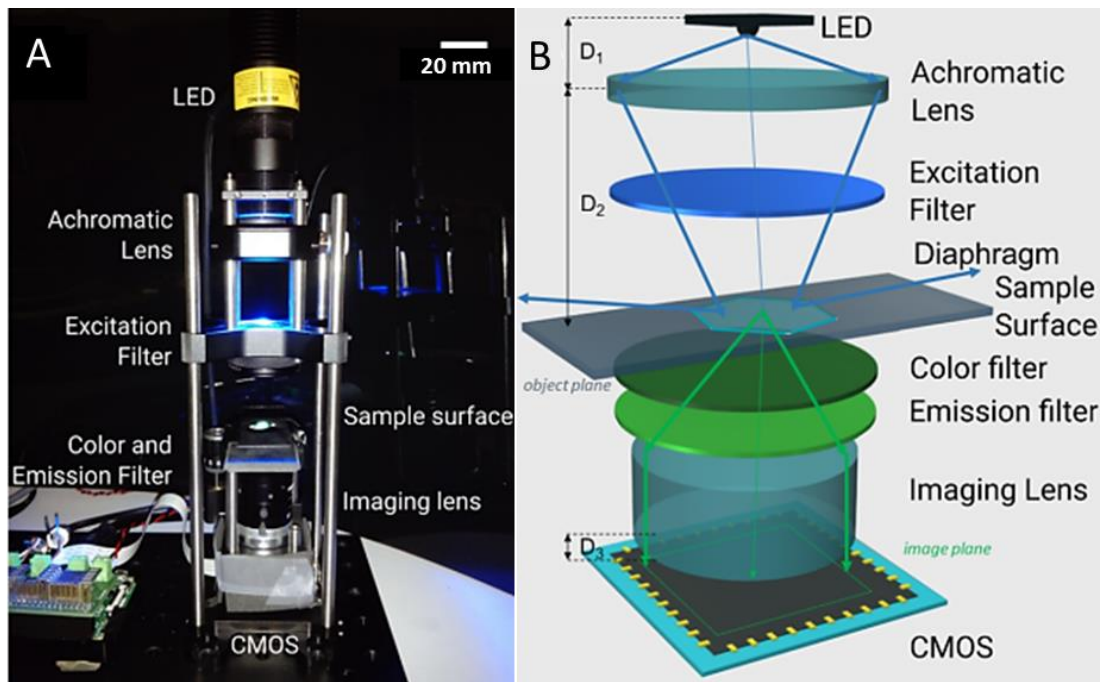
Figure 2.3. Optical setup surface cytometer. A. Photo of surface cytometer in the laboratory. B. Optical elements and light path from LED light source to CMOS detector with D_1 = 10 mm, D_2 = 50 mm, and D_3 = 11 mm.

2.3. Depth of field of the surface cytometer

Determination of the depth of field of the surface cytometer using 1951 USAF target provided a value of 3 mm. In order to evaluate the performance of the surface cytometer at a larger depth of field, labeled bacterial cells were placed in focus, then images were acquired at incremental steps in axial direction away from the focus for both the surface cytometer and the microscope. The surface plane was moved with a precision ½" translation stage (Thorlabs CT1) in the case of the surface cytometer while for the microscope the focal plane was adjusted using a piezoelectric-driven objective positioner. Bacteria in LB growth medium were used as control sample and compared with bacterial suspension to which fixatives either ethanol or glutaraldehyde were added. The fixatives ensure that the majority of the bacteria deposit on the surface, thus assemble in the same plane. Results are illustrated in figure 2.4. From the surface cytometer data, it is clear that the detected signal in the green channel remains stable over a distance of 3 mm away from the focus of the sample plane. The signal of glutaraldehyde 2.5% (v/v) varies somewhat from ethanol which is most likely due to a lower efficiency. The addition of 40% (v/v) absolute ethanol to the bacterial suspension results in the highest mean fluorescence measured, indicating that most bacteria were on the surface. After 3 mm the signal changes abruptly, indicating that outside of the depth of field range background signals from out-of-focus objects are pronounced while normally the focus is solely set to the center of the CMOS-ISA sensor.

To quantify the number of bacteria present in one digital image obtained from TIRF microscopy we used a particle analysis algorithm. In total 53 frames of a Z-stack series covering a distance range of 2 μm below the surface to 50 μm above it were analyzed. The results of the particle counts are displayed in figure 2.4B with trend lines for the three series of measurements, averaged from 3 to 4 stacks. After just 10 μm from the focus a clear drop in particle count becomes apparent, indicating that the depth of field is more than two orders of magnitude smaller compared with the surface

cytometer. This confirms that the surface cytometer has an improved depth of focus while being capable of measuring samples at larger volumes and because an average fluorescent signal is collected this minimizes bias towards the density of bacteria on the surface compared to those further away from it in the bulk liquid.
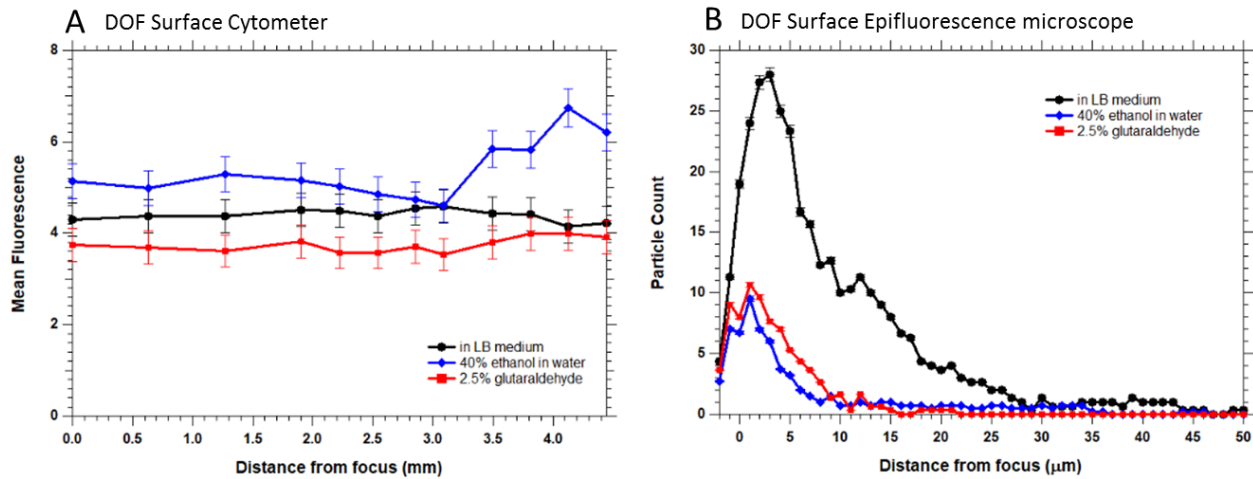
Figure 2.4. Comparison depth of field measurements between the surface cytometer and the microscope. A. DOF mean fluorescence data obtained with the surface cytometer. B. DOF analysis based on particle counting on a z-stack of images.

E.coli bacteria were used at O.D. 0.2 and stained with SYBR Green. Legend, ●black circles from LB medium, , ■red squares after fixation with glutaraldehyde at 2.5% (v/v) final, and ◆blue diamonds after fixation with absolute ethanol to 40% (v/v) final. The surface cytometer offers a higher DOF and thus measures a larger sample volume compared with traditional microscopy.

2.4. Experimental validation of the surface cytometer

The surface cytometer was experimentally validated through bacterial growth detection and comparison with spectrophotometry and fluorescence microscopy. A typical bacterial growth curve goes through three phases. In the lag phase, bacteria adapt to their new environment showing minimal growth, in the exponential growth phase they proliferate rapidly, and the stationary phase the growth- and death rate are assumed similar. These growth curves are very easy to produce by measuring the change in optical density (OD) over time with a spectrophotometer.

Spectrophotometric optical density measurements

A temporal-dependent increase in the number of bacteria correlates with more light absorption. All experiments were conducted using *Escherichia coli (E.coli)* bacteria (Invitrogen DH5α strain). To start a new 8h growth cycle, fresh LB broth growth medium (Scharlau 02-384-500) was inoculated with an overnight bacterial culture and placed in an incubator shaker (Thermo Fisher Scientific MaxQ8000) at 37 °C. At about 30 min time intervals an aliquot of bacterial suspension was extracted. The aliquot was divided into three separate aliquots. After measuring a blank sample, the first aliquot of 1 ml bacterial suspension was used to measure the OD with the spectrophotometer (Thermo Fisher Scientific Nanodrop 2000c) set at a wavelength of 600 nm. Measurements with the spectrophotometer served as reference. The second two were stained with SYBR Green I (Invitrogen S7563) that diffuses into DNA and fluoresces upon intercalation. No washing is required because when it is unbound, the dye has very low background signals. After a 20 min incubation time, one aliquot was used for measurements with the surface cytometer while the other was used for

fluorescence microscopy. Note that OD measurements are done in a cuvette with a large volume while the latter two are done on glass surfaces.

Surface cytometer measurements
Borosilicate cover slips of a 100 µm thick (Knittel Glass) were divided into compartments by silicon isolators (Grace Bio-labs GBL665301). After adding 50 µl bacterial suspension into the compartments, images were acquired through the green channel and the obtained mean fluorescence was correlated to the concentration of bacteria in cells/mm^2 from which the growth curve was generated. In a separate experiment, the LOD was tested with a dilution series of Alexa Fluor 488 and determined to be about 1 nM.

Epifluorescence microscopy measurements
TIRF microscopy experiments were carried out with commercial a Nikon inverted fluorescence microscope (Nikon Eclipse T*i*) with a 100x Plan-Achromat oil immersion objective (NA 1.49). Samples were excited with a 488 nm laser with a power in the range of 0.0166 to 0.002 mW. Emitted light was collected by the objective, filtered with a quad-band filter cube (LF405/488/561/635-A-NTE), and detected onto an electron-multiplying charged-coupled-device (EMCCD) camera at an exposure of 100 ms per frame.

2.4.1. Reference bacterial growth curve based on optical density measurements

As bacteria grow over time, their density in suspension increases which causes more light to be absorbed during the optical density measurements. From these measurements performed over several days, we generated the normalized bacterial growth curve presented in figure 2.5. For comparison to surface cytometer data, two well-known models that belong to the family of Richards sigmoid growth models, were fitted to our growth curves to quantitatively describe microbial growth and determine the corresponding growth parameters. The Gompertz-Zwietering model[67,68] was applied to derive the lag time (T_{lag}) and the absolute growth rate (k_z) with:

$$\text{OD(t)} = B_G + A_G \exp(-\exp(\frac{ek_z}{A}\left(T_{lag} - t\right) + 1))$$

While the logistic population growth model adapted to bacterial growth was used to determine the maximum growth rate, *r*, as well as the seed ratio, x_0, of the inoculum size [68,69]:

$$\text{OD(t)} = B_R + \frac{A_R}{(1 + \left(\frac{1}{x_0} - 1\right)\exp(-rt))}$$

Where, A_R and B_R are constants for normalization of the experimental data. From the logistic model we deduced x_0 = 0.0077 ±0.001 and r = 0.0140 ± 0.0004 s^{-1}. The obtained time frames for the different phases of growth were 191 ± 14 min for the lag phase, which is rather short, 200 to 450 min for the exponential growth phase, and the stationary phase started after 500 min. The calculated absolute growth rate k_z = 0.0035 ± 0.0004 s^{-1}. Furthermore, we found a residual error X^2 = 1.67 10^{-3} for the Gompertz-Zwietering model and X^2 = 1.60 10^{-3} for the logistic model, respectively. These findings show that the fitting models are well-suited for our data, justifying that both the obtained growth curve as well as its corresponding parameters can serve as reference for our further study.
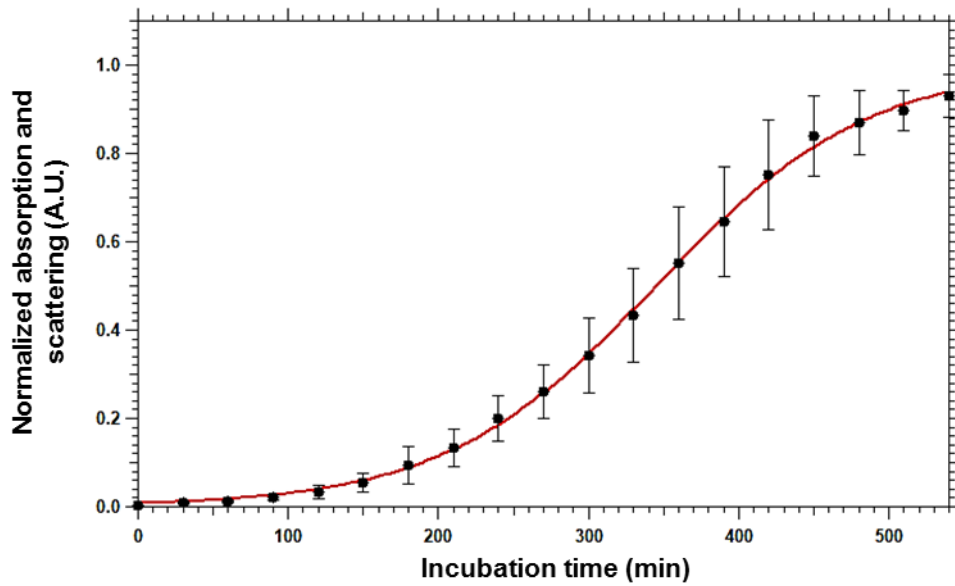
Figure 2.5. Bacterial growth using spectrophotometry. The absorption and scattering of bacteria in suspension were measured through optical density at a wavelength of 600 nm. Discrepancies in the error bars are as a result of experiments performed over several days. Normalized data based on the logistic population growth model indicated by the red line. Maximum growth rate r = 0.0140 ± 0.0004 s^{-1}.

2.4.2. Bacterial growth curve based on fluorescence microscopy analysis

Microscopy is another widely-used technique in studies about biofilm formation.[53,56] Digital images acquired at about hourly intervals and the corresponding growth curve after analysis are depicted in figure 2.6 The growth curve was obtained by counting cells using a particle analysis algorithm. To remove possible contributions of autofluorescence from the glass surface and unbound fluophore in the focal plane, digital images were first background subtracted using the rolling ball approach set at 10 pixels which roughly corresponds to 1.5 µm, the width of *E.coli*. Each digital image had a FOV with a size of about 82 x 82 µm in which particle analysis with Fiji software[70] was performed to count the number of bacteria. All images were analyzed at a 16-bit scale with a minimal intensity threshold set at 29.000. As the number of bacteria increased over time it became challenging to distinguish between adjacent cells so we applied the watershed algorithm[71] to delimit and count cells. Analysis parameters such as area and circularity were set according to the typical dimensions of *E.coli*. [72,73] The particle area was set to be above 3 µm and the circularity values between 0.0 and 0.8. The circularity parameter c[36], indicates how close an object resembles a true circle and is defined as:

$$c = 4\pi \frac{A}{P^2}$$

Where A is the area, P the perimeter, and c = 1 represent a perfect circle while c = 0 an elongated object. Figure 2.6B depicts the growth evolution based on cell counting. Notice that all phases of growth cover shorter time frames compared with the spectrophotometric reference curve. This could be due to several factors. Bacterial behavior alters near a surface and this triggers certain genes to be upregulated and others to be downregulated to favor cell adherence to a surface and promote growth.[30,36] However, as imaging is done within 30 min after harvesting aliquots which is also within the time needed for *E.coli* to double, we expect the effect derived from growth to be minimal. The shorter phases obtained are rather due to artefacts introduced by the experimental

procedure, the surface, and the limitation to distinguish between adjacent cells during image processing. Living cells do not readily adsorb unto a solid abiotic surface[74] but is a prerequisite for microscopy imaging. Additionally, only objects in the focal plane are considered but not all out-of-focus signals that come from a larger distance from the surface are eliminated. Taken together, these factors contribute to an underestimation of the number of bacteria within the sample compared with the reference curve. Moreover, the relatively small FOV only allows very local evaluation of a sample and thus one needs to acquire multiple images of several representative positions within the sample. The software analysis is a good approximation to quantify fluorescence signals from specimen on a surface but always includes trade-offs as biological samples are inherently variable and thus some degree of error is always present. Also, as time evolves fewer vacant sites are present on the surface so fewer bacteria can be counted. These considerations have outlined that fluorescence microscopy assesses small sample volumes at great detail but its use is constrained for larger sample volumes in situations where answers are rapidly needed. The surface cytometer is a direct method circumventing some of the highlighted limitations in microscopy with the potential to be used for in-situ measurements.
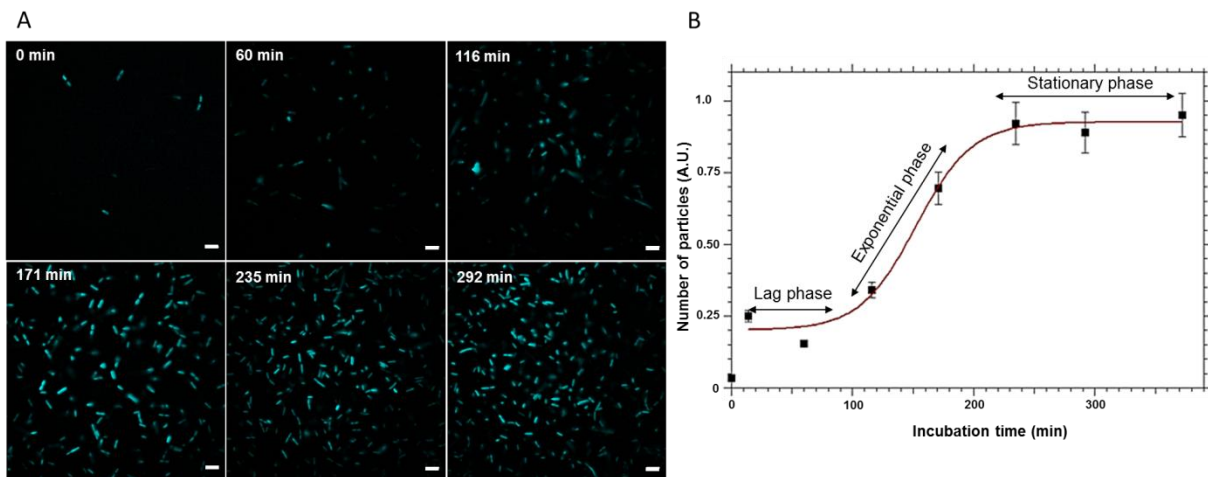
Figure 2.6. Bacterial growth using fluorescence microscopy. A. Images acquired at different time intervals were background subtracted with the rolling ball algorithm set a radius of 10 pixels (1.6 μm) using Fiji software. B. Corresponding growth curve obtained from particle analysis with the red line indicating the expected curve from a sigmoid fit. Different stages of growth are indicated. The stationary phase plateau corresponds to about 180 particles. Scale bar 5 μm.

2.4.3. Bacterial growth curve based on surface cytometer measurements

This section focuses on the performance of the cytometer and compare the obtained result with the reference growth curve as well as the growth curve generated from microscopy. Background measurements with the same exposure time were acquired, first with the camera on and then off. Then the fluorescence intensity of bacterial suspensions was measured and only signals from the green channel were considered from which the background was subsequently subtracted. As only the mean fluorescence values were considered no actual images were stored. In contrast to microscopy, the surface cytometer measures larger sample volumes at greater depths providing more information of the sample. As SYBR Green I is reported to reliably and efficiently (> 99%) stain bacteria,[74] we assumed that fluorescence signal averaged over the large field-of-view of the

cytometer reader was directly proportional to the number of bacteria present in the sample. Therefore, the Gompertz-Zwieter and logistic growth models applied to the optical density measurements could be used for the surface cytometer data. For comparison purpose, the collected signal was transformed to an intensity value with $I(t) = ln(C(t)/C_0)$. Where C is the intensity of the signal averaged over the entire CMOS image sensor at incubation time t, and C_0 is the signal averaged of the CMOS sensor prior to sample insertion.

The final normalized growth curve depicted in figure 2.7 is based on the average signal from 3 consecutive measurements of each triplicate data point, omitting the lowest and highest values. Data at low concentrations were excluded from fitting because they came from power fluctuations of the system and would add error. For visual representation we applied an offset to overlap the first reliable data point with the reference optical density curve to make comparison straightforward. Based on the model we found the seed ratio x_0 = 0.017 ± 0.005, and the maximum growth rate r = 0.0120 ± 0.0009 s^{-1}, with residual error X^2 = 4.77 10^{-3}. The error bars represent twice the standard deviation (±2σ). Furthermore, from the Gompertz-Zwieter model we obtained an absolute growth rate of k_z = 0.0031 ± 0.0007 s^{-1}, T_{lag} 165 ± 4 min with X^2 = 5.43 10^{-4}. Most of these values and the onset of the exponential growth phase are in close agreement with reference curve thus confirming the suitability of the surface cytometer as surface sensing device with the capability to assess samples at a larger FOV and larger depth of field compared with microscopy. Note however that the lag phase is lightly shorter compared with the reference curve and the value for x_0 suffers imprecision because the surface cytometer has reduced sensitivity at lower concentrations. The bacteria counting using image analysis of the fluorescence microscope compares well with the counting of the surface cytometer.
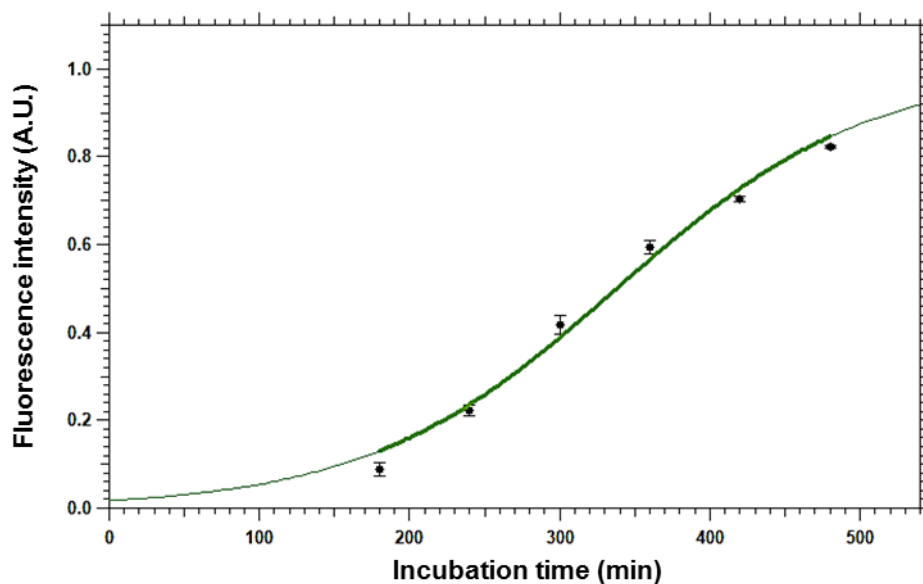
Figure 2.7. Bacterial growth using surface cytometry. Fitted fluorescence intensity (in green) based on the logistic population growth model. Maximum growth rate r = 0.0120 ± 0.0009 s^{-1}. The growth behaviour reflects the trends of figures 2.5 and 2.6.

Device acquisition characteristics for the spectrophotometer, the fluorescence microscope, and the surface cytometer are summarized in table 2.1 for comparison.

Table 2.1. Comparison acquisition features spectrophotometer, microscopy, and surface cytometry. The data are approximate values.

	Spectrophotometer	Microscopy	Surface cytometer
Field-of-view	20 mm^2	7 x 10^{-3} mm^2	200 mm^2
Depth of field	2 mm	< 30 µm	2 mm
Acquisition time	< 1 min	< 5 min	< 1 min
Post-processing	no	Yes	Yes

Many optical-based sensors have been proposed and to place our technology into context with the performance of other sensing devices in the field, we compared several criteria and summarized them in table 2.2. This table corroborates the suitability of our surface cytometer as rapid, portable, and low-cost technology with acceptable LOD values compared with other biosensing technologies.

Table 2.2. Comparison available techniques to monitor bacterial biofilms to our work.

Method	LOD (cells/ml)	LOD (cells/mm^2)	Time (min)	Real-time	Portability	Substrate	Reference
This work	-	~10^4	< 1	Yes	Yes	Glass	-
FISH	10^4	-	< 5	Yes	Yes	Glass	[75]
qPCR	-	10^2	> 60	No	No	Custom	[76]
UV	-	10^4	< 1	Yes	No	UV-grade	[77]
Colorimetric	10^2	-	> 60	No	Yes	Custom	[78]
Magnetic	-	10^3	< 1	Yes	Yes*	Direct	[63]
SERS	10^2	10^4	< 20	No	No	Custom	[79]
Electrochemical	10^2	-	> 20	No	No	Custom	[64]

*Requires a network analyzer to read the response.

2.5. Conclusion and outlook

We have provided experimental data that validates our in-house devised CMOS-based fluorescence reader which is capable of detecting and quantifying cells on surfaces by measuring the fluorescence intensity over a volume. The surface cytometer, was benchmarked against fluorescence microscopy and spectrophotometry which are widely-used laboratory devices. All three devices illustrated a similar trend in their bacterial growth curves. This places the surface cytometer in a promising position because of its distinct advantages to measure large field-of-views (about 200 mm^2) and large depths of focus (about 2 mm) further improvement of the system could be of great interest for in-situ measurements and point-of-care testing. Additionally, the device is portable, compact, and measurements take only a few minutes without the need of complex post-processing. The total time-to-result is between 15-20 min, which is rapid however, not specific. In contrast, many of the standard laboratory equipment is bulky, expensive, not portable and requires trained personnel. For instance, a simple light-emitting diode and CMOS-based sensor are at the core of the surface cytometer whereas high-end fluorescence microscopy requires expensive lasers and electron-multiplying charged-coupled device (EMCCD) sensor technology. Further advancements of the surface cytometer technology should consider several issues such as possible improvement of its sensitivity at low concentrations, sample collection via swabbing and possibly amplifying (genetic) material using qPCR to reach the current limit of detection. Also, bacteria take time to reach a surface so by mounting wells on our setup with defined dimensions that fall within the measuring limit of the surface cytometer, a fixed volume of bacterial suspension could be assessed rapidly. Antibody-based fluorescent labels could further increase the specificity for microbes but the staining procedure involves several incubation-and washing steps thus require more time. In summary, our proposed surface cytometer was validated and proven suitable to detect cells and their growth on surfaces.

Chapter 3: An ultrathin gold quencher for improved imaging of bacteria

The content of this chapter is material under consideration for a journal paper submission (Note that the author list and order may change at the time of the submission to a journal).

Sibilo, R, Pérez, JM, Tebbenjohanns, F, Hurth, C, Campelo, F, Bareza, N, Maniyara RA & Pruneri, V 2021, `Imaging and detection of bacteria on a surface enhanced by an ultrathin metal quencher', *xxx*, vol. xx, no. xx, pp. xxx-xxx.

Quantitative fluorescence imaging aims to produce digital images with high contrast.[80] During the acquisition of a digital image, photons detected at each pixel are converted to an intensity value that is related to the number of detected photons.[81] The images can be used to quantitate spatial- and intensity information from a specimen. The intensity values within a digital image are composed of the signal and the background. By maximizing the signal relative to noise and background, i.e., improving the signal-to-noise ratio (SNR), the measurement and images become more precise.

In this chapter, we provide numerical calculations and experimental evidence that surfaces with ultrathin metal films are capable of quenching fluophores in their proximity, reducing their lifetime. Experimental work corroborates the applicability of improving the SNR through these metal surfaces for imaging microspheres, bacterial cells, and proteins using fluorescence microscopy and surface cytometry. Numerical calculations confirm fluorescence lifetimes, which increase with the distance from the metal surface and are strongly reduced within approximately the first 10 nm. A visual summary of the work is depicted in the mind map of figure 3.1.
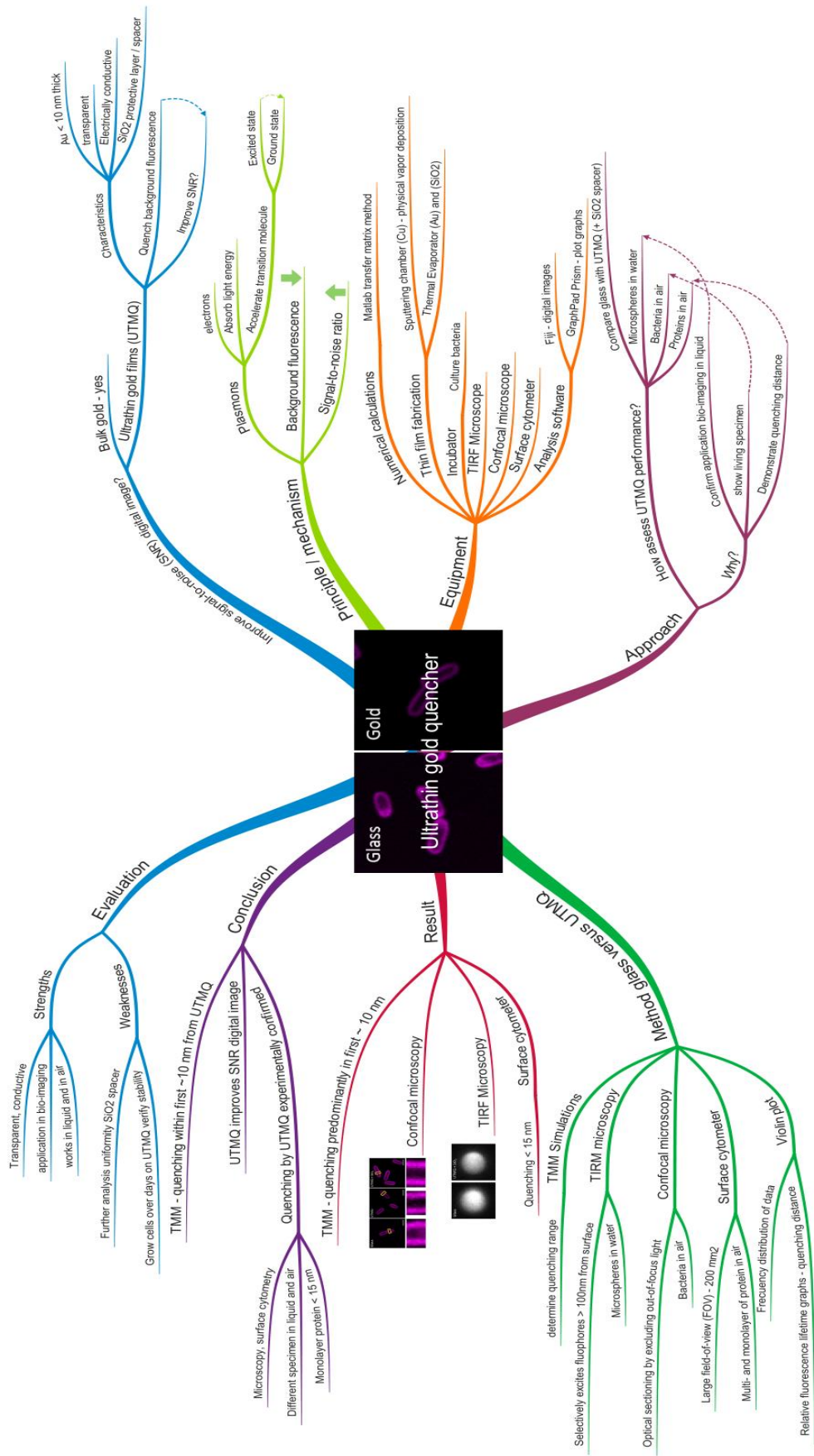
Figure 3.1. Mind map of Chapter 3. An ultrathin gold quencher for improved imaging of bacteria.

3.1. State-of-the art and surface design

Background reduces the SNR because Poisson noise is equal to the square root of all detected photons - signal and background.[82] Fundamental limitations based on quantum mechanical events are limited by Poisson statistics that cannot be eliminated however, its contribution to the intensity in images can be minimized by collecting more photons.[83] Therefore, background from various origins such as imaging parameters (excitation light, camera noise) and autofluorescence from the sample (unbound dye, the medium) need to be constrained. We provide numerical calculations and experimental evidence that surfaces with ultrathin gold metal films, predominantly quench background fluorescence within the first 10 nm from the substrate but becomes less noticeable at larger distances. As a result, the SNR in digital images is improved. Experiments were carried out with fluorescence microscopy and surface cytometry measurements.

Previous research has shown to achieve optical localization at the sub- and nanometre level based on the principle of electromagnetic coupling of fluorescence to graphene and bulk metal films, respectively.[84,85] However, until recently, ultrathin metal films were not used because one of the greatest challenges in fabricating large continuous ultrathin gold films on glass was to overcome the poor wetting of gold. The latter leads to irregular island formations (Volmer-Weber growth mode) in the initial growth phase.[86] To overcome this drawback, a ~1 nm thick oxidised copper seed layer was first sputtered onto a glass substrate followed by gold evaporation producing a gold film with long-range connectivity and percolation at 1 nm thickness.[87]

The ultrathin metal quenching (UTMQ) surfaces have a gold film of a few nanometers thickness, are transparent and electrically conductive. We first numerically calculated the fluorescence emission modulation, i.e., the lifetime of a fluophore in proximity of the UTMQ and the range of quenching. In the near-field, the quenching is nonlinear for both UTMQ and UTMQ with a spacer but gradually converges with glass in the far field. Then, the applicability of UTMQ to quench background fluorescence in biological samples was experimentally assessed. Commonly used specimen in biology research such as bacteria, proteins, and microspheres deposited on UTMQ films of different thicknesses were imaged in both air and water using different imaging devices. These include confocal microscopy, total internal reflection fluorescence (TIRF) microscopy, and surface cytometry. The obtained results show SNR improvement in all cases. Throughout this chapter, SNR represents the ratio of the intensity taken from the fluorescent signal from specimen and the background ('noise') is the intensity of pixels in the area next to the specimen. A major advantage of and increased SNR is that more photons are collected and that could provide a more accurate localization precision in single molecule localization microscopy (SMLM). Moreover, background reduction minimizes photodamage to the specimen either through the use of a lower laser power or by improving the dynamic range of the camera because a shorter pixel dwell time is needed i.e., a shorter image acquisition time, which is particularly important for live imaging. Additionally, the UTMQ may aid in reducing background from remaining unbound fluorophores in the medium. visualizes fluorescently labelled bacteria on a glass- and UTMQ surface, respectively. A side- and top view of the fabricated UTMQ surfaces is displayed as well. The quenching principle is shown in figure 3.2 together with the fabricated surfaces.
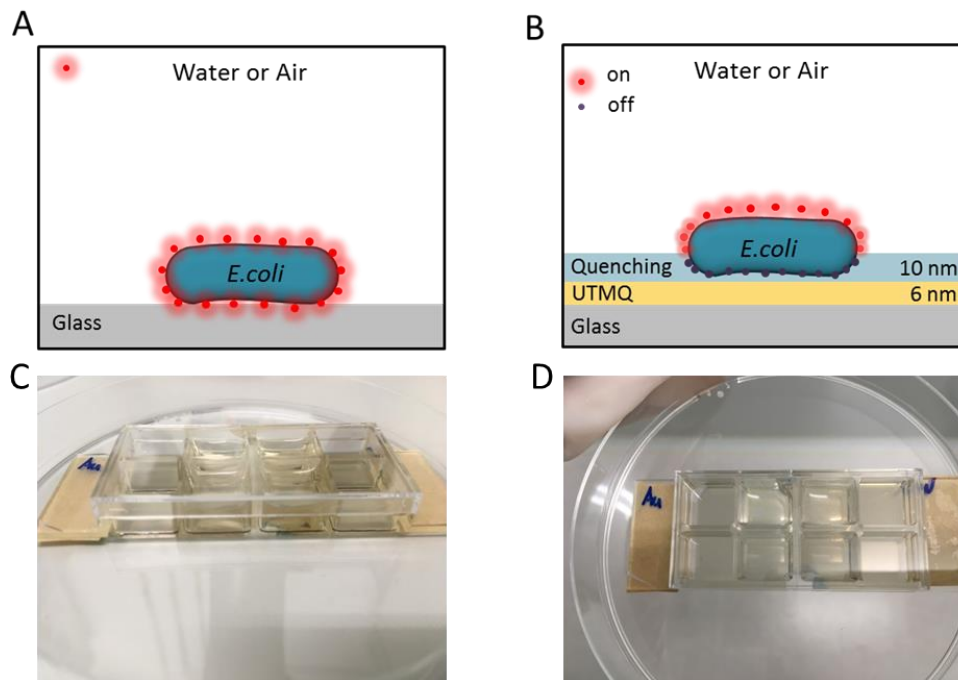
Figure 3.2. Quenching principle and fabricated surfaces with UTMQ. A. Fluorescently labeled *E.coli* (not in scale) on bare glass with fluophores switched on and B. in proximity of the Au UTMQ surface the fluorophores get switched off, quenched. Quenching reduces at larger distances from the surface. C and D are side- and top view of the fabricated UTMQ.

3.1.1. Physical principle

Fluorescent molecules (emitting dipoles) on substrates (planar structure) are excited and detected through a microscope objective. In proximity of a metal surface the radiation emission power *P,* i.e., fluorescence emission of an excited molecule can be enhanced or suppressed. In this study, we assessed multilayered planar structures made of different thicknesses of gold films (UTMQ) either with or without a silica (SiO$_2$) spacer. The ability of UTMQ substrates to accelerate the energy transfer of a molecule in the excited state to its ground state was assessed through numerical simulations and lab experiments. Simulations of this phenomenon or more precise, near-field electrodynamic coupling of the dipole at a distance z_0 from the multilayer UTMQ surface were performed according to the scheme presented in figure 3.3. For all simulations throughout this chapter the distance z_0 refers to the topmost layer of the UTMQ.
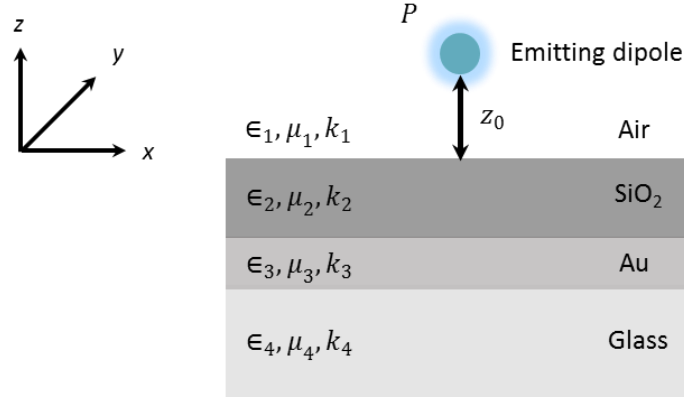
Figure 3.3. UTMQ multilayer structure. A fluophore is considered an ideal electric dipole emitter at distance z_0 from the topmost layer, its radiative emission power is indicated by the letter P. UTMQ multilayer structure extends infinitely in the x- and y- direction with the z axis perpendicular to all interfaces.

The emitting dipole is considered as an ideal oscillating electric dipole and its electromagnetic field is mathematically presented by a superposition of left- and right travelling plane waves. The interaction of each of these waves with the UTMQ can be calculated using Fresnel's coefficients which provide the desired electromagnetic field (EM) field of the emitting dipole in the form of reflection- and transmission coefficients. Then by integrating the Poynting vector, representing the directional energy flow, of the layered UTMQ this leads to the total energy flux of the emitted EM field through the surface. Finally, this can be used to describe the full emission rate of the emitting dipole as well as the energy absorbed by the metallic substrate. The emission rate does not depend on the angle of orientation but only on the distance z between the dipole and the surface.[88]

The onset to study the propagation of EM waves through a multilayered structure is Maxwell's equations which requires continuity of the electric field, $\vec{E}$, across the boundary from one medium to another.[89] Based on this, EM calculations for each layer can be done with the transfer matrix method to obtain the emission power of the dipole emitter as a of function of z_0 and dipole orientation θ, with respect to the interface and can be expressed as:

$$P(z_0, \theta) = P_\perp(z_0) \cos^2(\theta) + P_\parallel(z_0) \sin^2(\theta)$$

$$\frac{P_\perp}{P_0} = 1 + \int_0^\infty \frac{3}{4} \mathrm{Re} \left\{ \frac{s}{s_z} [r^s - s_z^2 r^p] e^{2ik_1 z_0 s_z} \right\} ds$$

$$\frac{P_\parallel}{P_0} = 1 + \int_0^\infty \frac{3}{2} \mathrm{Re} \left\{ \frac{s^3}{s_z} r^p e^{2ik_1 z_0 s_z} \right\} ds$$

where $P_\perp(z_0)$ and $P_\parallel(z_0)$ represent the perpendicular and parallel components with respect to the UTMQ normal respectively, P_0 as free-space emission, s and s_z as normalized transverse and normal wavevector components respectively, and $k_1 = \sqrt{\epsilon_1 \mu_1} \frac{\omega_{em}}{c}$ as the wavevector evaluated at emission frequency ω_{em}. The permittivity, ϵ_1, is the characteristic dielectric constant of a material and is a measure of how much molecules oppose to an external electric field in other words how easily they can be polarized when subjected to an electric field. The other fundamental material parameter, μ_1, is a measure of how easily a magnetic field can pass through a given medium. The speed of light is shown as c. The ratio of the emission power in free-space to the emission in presence of the UTMQ

reflects the degree of suppression of the fluorescent emission rate as a function of position, hence the quenching enhancement. This is inversely related to the lifetimes of emitting dipole in the excited state τ and non-radiative part in free space τ_0 by $\frac{\tau}{\tau_0} = \frac{P_0}{P}$ which we coin relative fluorescence lifetime throughout the chapter.

3.2. Numerical simulations

The electromagnetic field reflection coefficients r_p and r_s were calculated from Fresnel equations using the transfer matrix method (TMM) of Matlab. All calculations were carried out with thickness values of 1 nm for the copper seed layer and 5 nm for the silica protective layer. In the experiment, the copper layer is likely to be oxidised, in this way promoting wetting for the gold. Note that its thickness is anyway small compared to the gold layer, so is its contribution to the optical response of the surface. The refractive index of the glass substrate was approximately set to $n_{subs} = 1.52$. The refractive indices of the silica protective layer (n_{SiO2}) and the complex UTMQ combination (n_{Cu}, n_{Au}) depend on the emission wavelengths of the labeled specimen. Table 3.1 provides the experimental parameters such as the thickness of the gold layer, the emission wavelength of the fluorescent dye and the imaging condition, which were used to set up the numerical simulations. The refractive indices for the different thicknesses of the ultrathin layers of gold were approximated and adapted from the optical dispersion data of Yakubovsky et.al.[90]

Table 3.1. Numerical simulation parameters corresponding to experimental parameters for different types of UTMQ substrates.

Specimen + fluorescent label	Emission wavelength (nm)	Gold thickness & Complex refractive index
E.coli SYBR Green (air)	512	$n_{Au,12nm} = 0.7500 + 1.8364i$
E.coli QD (air)	605	$n_{Au,12nm} = 0.3130 + 3.0060i$
E.coli FM4-64 (air)	640	$n_{Au,6nm} = 0.5340 + 2.9980i$
Protein spots FITC (air)	512	$n_{Au,2nm} = 0.8166 + 1.9002i$
Dragon Green Microspheres (liquid)	520	$n_{Au,6nm} = 0.7900 + 1.8430i$

3.3. Experimental procedures

3.3.1. Deposition of gold ultrathin metal films (UTMFs) and SiO$_2$

Borosilicate-based glass substrates (Corning Willow glass) of 0.15 mm thick with areas of 1 square inch were ultrasonically cleaned with acetone followed by ethanol (10 min each), rinsed with deionized water, and dried with nitrogen gas. Then, the substrates were placed in a sputtering chamber and cleaned with low-power argon plasma for 15 min. Next, a 1 nm copper seed layer was sputtered onto the rotating substrates (60 rpm) through physical vapor deposition at 30 cm from the copper target (99.99% purity) using a DC power of 100 W and a working pressure of 2 mTorr. Subsequently, after a brief exposure to air, a gold thin film was thermally evaporated (Thermal Evaporator Kurt J. Lesker) at a deposition rate of 1Å/s. Further characterization is described elsewhere.[87] Finally, the gold UTMQ was protected by silicon dioxide (SiO$_2$) spacer. A 5 nm thick SiO$_2$ film was deposited onto the gold UTMQ substrates via ion assisted (IAD) thermal evaporation at

1Å/s. Before use, all surfaces were sterilized with 99.99% pure ethanol and rinsed in sterile MiliQ water, dried in air in the fume hood, and glued to sterile bottomless 8 well chambers (ibidi GmbH) prior to adding the fluorescently-stained bacterial suspension.

3.3.2. Bacterial growth and fluorescent labelling

E. coli DH5α bacterial cells were grown overnight in a Luria-Bertani nutrient broth (LB medium) in a shaker incubator (Thermo Fisher MaxQ8000) at 37 °C. The following day, 1 ml of the overnight culture was transferred to fresh medium and growth was monitored by measuring the optical density at an absorption wavelength of 600 nm (OD_{600}) with a spectrophotometer (Nanodrop 2000c, Thermo Fisher Scientific). In the first half of the exponential growth phase with an OD_{600} between 0.5 – 0.6, cells were harvested and diluted to an OD_{600} of 0.05. Next, fluorescent lipophilic membrane dye, FM4-64, (Thermo Fisher Scientific) (maximum of excitation/ emission spectra at 515/640 nm) at a concentration of 5 µg/ml was directly added to the bacterial suspensions. Then, 200 µl bacterial suspension was added to the different surfaces and left to settle for 20 min before the medium was removed from the center of the wells leaving bacteria in most condition with < 10 bacterial cells per FOV attached to the surface.

3.3.3. Statistical analysis line scan and violin plot

All raw microscopy digital images were processed with Fiji[70] using line scans. 2 lines scans (10 pixels wide ~ 1.6 µm, empirically chosen) per bacterial cell for 5 cells per substrate, 4 cells for the SiO_2 spacer, were taken and averaged to get the mean fluorescence intensity. This was done by selecting regions of the cells with the Fiji line option, edit, selection, and then straightened. Similarly, to determine the background, five locations away from the cells were selected and the average mean intensity line scan value was determined. Then, SNR, that we defined as the ratio between the signal of interest and the background signal, was calculated by taking the intensity from the signal (bacteria) and divide it by the average mean intensity of the background. The raw data for the fluorescence intensity from the cells or the microspheres were plotted along with the normalized version using GraphPad Prism 5 with the options column and then violin plot. A violin plot is a rotated symmetric kernel density plot that visualizes how the data is distributed. Data points in the wider region represent a high density and the narrow region a low density.

3.4.   Fluorescence quenching of bacteria

The following step was to see if the substrates would improve the SNR using living bacteria. Images were captured with a confocal microscope which takes the advantage of a spatial pinhole that removes out-of-focus light so that only light from the focal plane of the sample that passed through it, reaches the detector.[91] Confocal microscopy imaging experiments were carried out at room temperature with a commercial Leica TCS SP8 confocal microscope equipped with a pulsed supercontinuum white light excitation source using a 100x 1.4 NA HC PL APO CS2 oil immersion objective. The FM4-64 signal was acquired in the confocal mode, where the excitation was done at 515 nm at 7% of the white-light source intensity. The images were taken with 3x line accumulation (unidirectional scanning at 400 lines per second) in a z-stack mode, with a voxel size of 71.4 nm x 71.4 nm x 900 nm. The detection was done with a hybrid single molecule detector (HyD SMD) in

photon counting mode and an acquisition window set to 630–750 nm. Images were acquired with the Leica LAS AF software.

Figure 3.4 displays the obtained confocal images of *E.coli* bacteria that were allowed to adhere to the surface prior to removing liquid from the center of the glass, UTMQ, and UTMQ with SiO_2 spacer surfaces. In the lower series, a zoomed-in part of *E.coli* visually confirming an improved SNR for UTMQ and UTMQ with SiO_2 spacer compared with glass, with UTMQ outperforming both. Note, as *E.coli* were first allowed to adhere to the surface, the UTMQ surface shows the highest degree of quenching in the center and more defined cell membranes that are at a higher distance from the surface. Next, the line scan analyses are presented as density distribution of the data points. Figure 3.4B on the left the raw background data of the three substrates, followed by the raw data in the middle and the raw data divided by the background on the right. The raw background data are almost not visible for UTMQ and UTMQ with SiO_2 spacer. In general, UTMQ seems more variable but this is most likely due to imaging condition for one series of captures. Since only 5 cells were imaged and analyzed, more acquisitions would likely show a more accurate distribution. Nevertheless, the experimental results are in line with the simulation results confirming UTMQ provides largest SNR.

Figure 3.4C and D depict the calculated relative fluorescence lifetime corresponding to the imaging conditions of the bacteria in the long-range as well as in the short-range distance for each of three types of surfaces. The graph on the left shows the long-range evolution of the relative fluorescence lifetime as a function of increasing distance from the surface. In the proximity of the UTMQ and UTMQ + SiO_2 spacer, the fluorescence is substantially quenched but sharply decreases after z_0 reaches 25 nm which is visible in the graph by the increase in the fluorescence lifetime that finally converges in the far-field with the lifetime on glass surfaces.
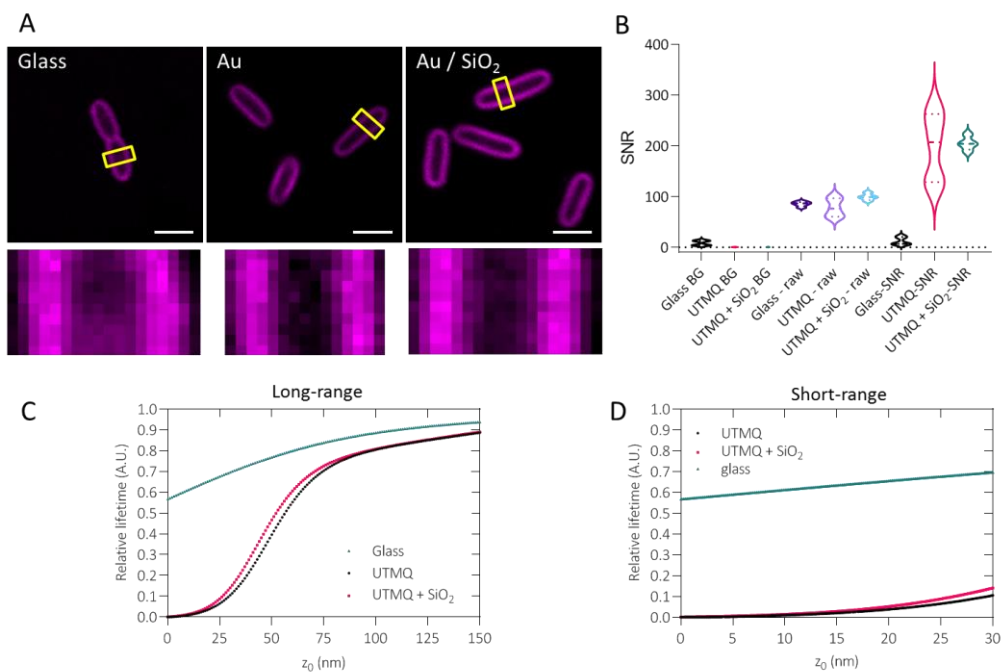
Figure 3.4. Confocal images and simulations of bacteria in air. A. Imaged bacteria on three different substrates, bare glass, a Au UTMQ, and a Au UTMQ with a 5nm SiO_2 spacer with the yellow boxes corresponding to zoomed-in images below. Scale bars = 5 µm. B. Violin plots obtained from the average fluorescence intensity from line intensity scans of bacterial cells. The first three data sets are background (BG) measurements for the three substrates, followed by the raw intensity values, and then the SNR, I.e., the raw intensity values divided by the background. Corresponding simulations C. Relative fluorescent lifetime as a function of distance z0 between a dipole and the top of surface for bare glass, Au UTMQ, and Au UTMQ with a 5 nm thick SiO_2 top layer (spacer). D. Similar to C. at distance z0 between the dipole and the top of surface is

shown from 0 to 30 nm with quenching strongly effective in the first ~ 10 nm. Simulation were performed at emission wavelength 640 nm and refractive indices, 1 for air, n(Au,6nm)=0.5340 + 2.9980i for Au, and 1,46 for SiO_2, respectively.

3.5. Fluorescence quenching of microspheres

To demonstrate that UTMQ surfaces can be used for imaging applications with biological specimen in buffers, we used fluorecent microspheres with similar sizes to bacteria (Dragon Green 1% w/v, 2.07 µm, Bangs Laboratories, Inc). TIRF microscopy has the advantage to selectively excite fluorophores in aqueous or cellular environment within ≤ 100 nm proximity from a solid surface, generating images with very low background fluorescence and practically no out-of-focus fluorescence.[92] Figure 3.5A shows a microsphere with a higher signal-to-noise ratio on the UTMQ + SiO_2 substrate compared with glass. Note, the non-uniform illumination typical to TIRF microscopy is less visible on the UTMQ while the laser power (0.05%) was the same for both substrates. Corresponding violin plots and background measurements are provided in figure 3.5B, showing the density of points at different values. Where the plot is wide the density of data points is high, the more narrow, the lower the density of data points. The intensity density plots are based on 15 microspheres. The distribution for glass is more spread but this is most likely due to the non-uniform illumination as some microspheres were not exactly in the center of the field-of-view and this seem more apparent in glass than in the case of the UTMQ surface. The stronger a fluophores gets quenched the shorter the fluorescence lifetime and in contrast, a reduced quenching coincides with an increase in the lifetime. Figure 3.5C shows a shifted quenching effect as function of distance in water for all three substrates compared with the results obtained in air in figure 3.4D because the lifetime of the fluophore depends on the characteristics of the different media so the speed of light is more reduced in water compared to air. Moreover, in contrast to gold which is an electric conductor that allows charge to flow, SiO_2 is a dielectric material and thus an electric insulator. Therefore, we observe that UTMQ with SiO_2 spacer quenches stronger within the first ~5 nm from the substrate while for the UTMQ alone this is within the first ~10 nm from the surface. However, for applications in biology, an SiO_2 layer offers more protection and stability. Together these results confirm that UTMQ and UTMQ with SiO_2 can be used for biological specimen in aqueous conditions.

Fluorescent microspheres (Dragon Green 1% w/v, 2.07 µm, Bangs Laboratories, Inc) were used to evaluate the surface quenching performance in a liquid since they are a common approximation of fluorescently-labelled cells used in biology imaging experiments. All TIRF imaging experiments were performed TIRF using a commercial Nikon inverted fluorescence microscope (Nikon Eclipse Ti) with a 100x Plan-Achromat oil immersion objective (NA 1.49). Excitation was done at 488 nm at 0.05% of the laser intensity. The emitted light was collected by the objective, filtered by a quad-band filter cube (LF405/488/561/635-A-NTE), and subsequently, collected by an electron-multiplying charged-coupled-device (EMCCD) camera with an exposure time of 100 ms per frame. A UTMQ surface was tested under these conditions together with its counterpart by flipping the surface with the Au layer in touch with the oil on the objective.
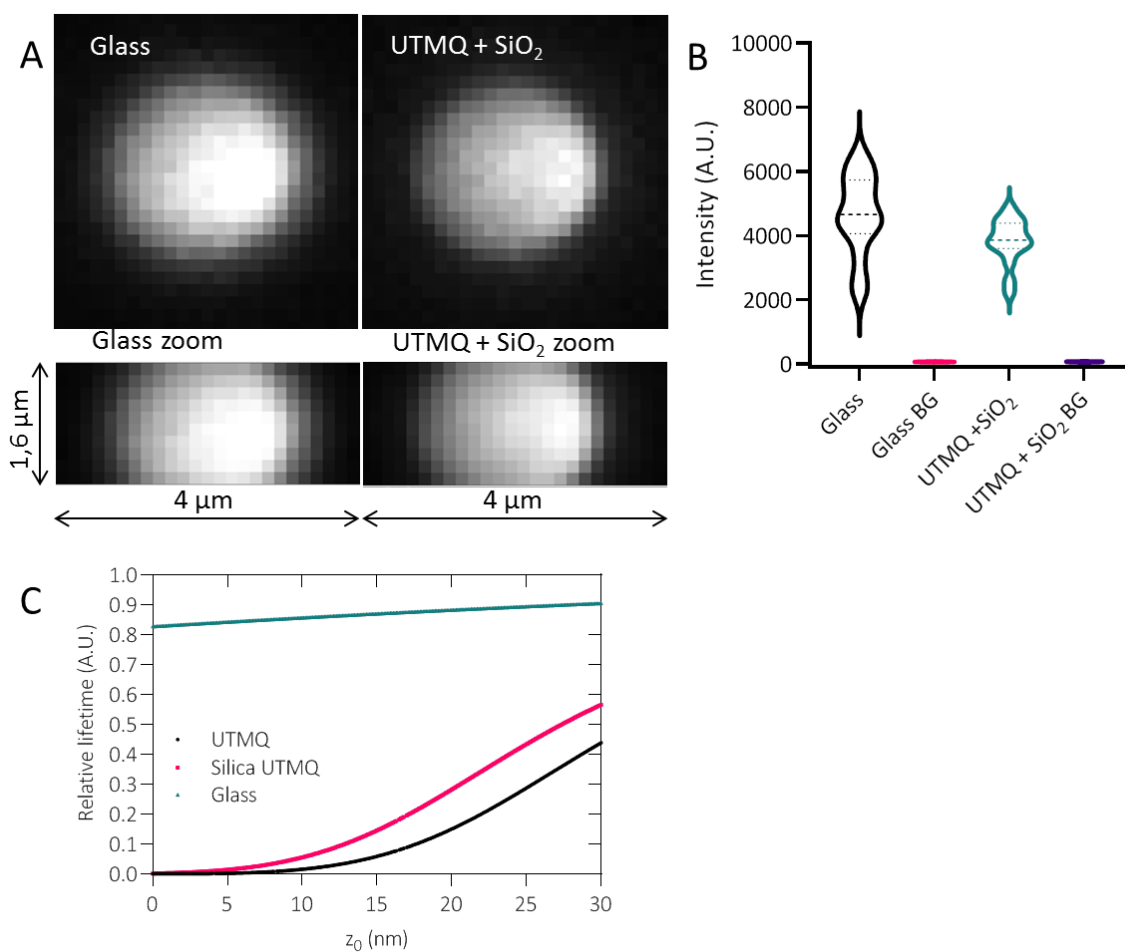
Figure 3.5. TIRF images of fluorescent microspheres in water. A. Green fluorescent microspheres of ~2 μm in size were imaged with TIRF microscopy on a Au UTMQ having a 5 nm SiO$_2$ spacer (left) and a similar surface was flipped so that the microspheres were on top of glass and Au UTMQ + SiO2 at the bottom in touch with the oil of the objective (right). B. Violin plot of the raw average fluorescence intensity from line intensity scans and the background for both glass and Au UTMQ with an SiO2 spacer. C. Corresponding calculated relative lifetime as a function of distance z_0 between a dipole and the substrates bare glass, Au UTMQ, and Au UTMQ with a 5 nm thick SiO2 spacer. Simulations were performed at an emission wavelength of 520 nm and refractive indices, 1,33 for water, 0,79 for Au, and 1,46 for SiO$_2$, respectively.

3.6.   Fluorescence quenching of proteins

This section presents experimental data generated by Felix Tebbenjohanns and Juan Miguel Pérez Rosas who performed quenching experiments with the surface cytometer using proteins.

To demonstrate that the UTMQ could also be used for localization at the nanometer level, we spotted Fluorescein isothiocyanate (FITC) labeled bovine serum albumin (BSA) proteins as spacer on epoxysilane coated glass and on a 2 nm Au thick UTMQ. The BSA proteins' sizes are ~14 nm for their major axis and ~40nm for their minor axis.[93] Nine spots were left to air dry and formed a multilayer (figure 3.6A & C) of which the fluorescence was captured. Next, the samples were washed leaving monolayer proteins on the surface (figure 3.6B & D) which was confirmed by interferometry. [94] Surface cytometry measurements were taken with a shutter time (t_s) of 3 s and analog gain (G_a) of

331/128. The average fluorescence intensity of the spots was compared with the background area next to the spots. The difference between them is represented by the symbol, Δ. The standard deviation σ (Δ) is calculated from the sum of the variances of the spot averages and the background.

In figure 3.6A and B fluorescence is visually clearly observed on epoxysilane surfaces, the intensity is strongly reduced on UTMQ and even more after washing to almost a similar value as the background, as seen in figure 3.6C and D. The table shows the averaged intensity value of each spot ($\bar{I}_{spots}$) as well as the background from the area surrounding the drops ($\bar{I}_{background}$). The difference is represented as Δ and the corresponding standard deviation by σ(Δ). The corresponding relative lifetime for glass and the 2 nm Au UTMQ are provided in figure 3.6E where quenching is predominantly achieved within the first ~10 nm from the UTMQ surface, in line with previous findings with bacteria and microspheres. The results confirm that the UTMQ is able to detect specimen at the nanometer level.
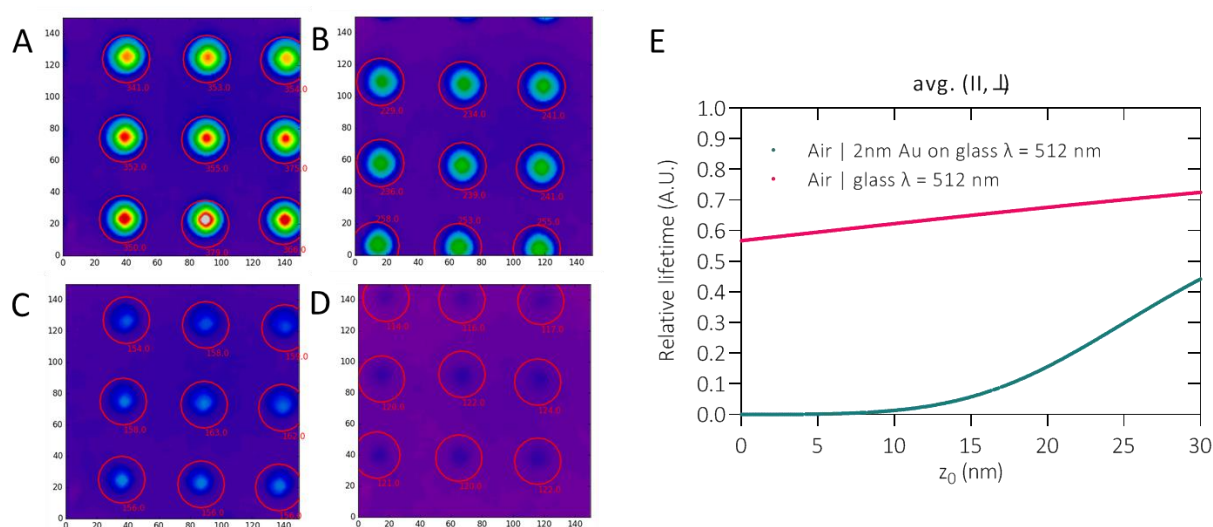
Figure 3.6. Surface cytometer measurements in air of FITC labelled BSA spacer spotted on glass and a 2 nm Au UTMQ. Captures of fluorescence from a multilayer of BSA on epoxy glass A. prior to rinsing and B. after rinsing. Quenched fluorescence from a monolayer of BSA on a Au UTMQ C. prior to rinsing and D. after rinsing. E. Corresponding calculated relative fluorescent lifetime as a function of distance z0 between a dipole and the substrates bare glass and Au UTMQ with a ≤ 15 nm thick BSA protein spacer. Simulations were performed at an emission wavelength of 512 nm and refractive indices, 1 for air and 0,82 for Au and show quenching the axial direction of around 10 nm.

Table 3.2. Fluorescein isothiocyanate labeled BSA spotted on epoxysilane coated glass and a 2 nm Au UTMQ. Averaged intensity value of each spot ($\bar{I}_{spots}$) and background area next to drops ($\bar{I}_{background}$) with the difference between them indicated by Δ and the corresponding standard deviation, σΔ.

Substrate	Monolayer	$\bar{I}_{spots}$	$\bar{I}_{background}$	Δ	σ(Δ)
Epoxy glass	No	358.4	133.6	224.8	13
Epoxy glass	Yes	242.8	127.3	115.5	11.8
2 nm Au UTMQ	No	157.9	130.8	130.8	4.1
2 nm Au UTMQ	Yes	119.6	116.2	116.2	4

3.7. Conclusion and outlook

Ultrathin quenchers made of gold films were fabricated and tested to quench background fluorescence and hence increase the SNR in fluorescence intensity digital images, obtained from microscopy and surface cytometry. Numerical calculations via the transfer matrix method identified that fluorescence modulation of the fluorescence emitter by UTMQ is dominant in the near field within the first ~10 nm distance from the surface potentially opening the possibility to image at the molecular level. We provided evidence for applications to improve SNR by imaging microspheres, living bacteria and BSA proteins smaller than 15 nm of which the fluorescence emission was quenched thus further supporting simulation results. Future development of this approach should consider the analysis of the SiO_2 layer protecting the gold and the gold film stability over various days in the presence of commonly used buffers in microscopy. Moreover, single molecule detection could be performed on these surfaces to experimentally confirm improvement in spatial resolution because of an improved SNR in presence of an UTMQ. Though gold is considered bio-compatible, at the nanometer level one should also evaluate cell fitness after adherence to the UTMQ substrate. An interesting path to explore would be to use silver because of its potentially improved quenching properties with respect to gold. When combined with a protective SiO_2 layer that avoids oxidation, it may open new possibilities in biosensing applications enhanced by ultrathin metal films.

Chapter 4: Transparent nanostructured bactericidal glass

The content of this chapter has been adapted and paraphrased under the terms of the Creative Commons Attribution Non-commercial license, from the original publication:

Sibilo, R, Mannelli, I, Reigada, R, Manzo, C, Noyan, MA, Mazumder, P & Pruneri, V 2020, `Direct and fast assessment of antimicrobial surface activity using molecular dynamics simulation and time-lapse imaging', *Analytical Chemistry*, vol. 92, no. 10, pp. 6795–6800.

When surfaces are contaminated with pathogenic microbes they become a source of transmission, increase the risk of healthcare-associated infection (HCAI) and the spreading of antimicrobial resistance (AMR).[95] Once a single bacterial cell irreversibly adheres to a surfaces, it can proliferate and transform into a microbial community called a biofilm consisting of microbes and non-microbial matter. A biofilm is a 100 to 1,000 times more resistant than single cells, that is why it is essential to prevent pathogen adherence when they are still in their planktonic, also called single-cell phase.[96]

This chapter presents a new approach to directly monitor the effect on bacteria of different glass substrates´ surfaces with tuned wetting and morphological characteristics. The physiochemical surface properties were tuned through non-reactive self-assembling molecules. Molecular dynamics simulations were used to predict the bacteria- surfaces interactions at the molecular level, followed by direct observations of these effects at the macro level using time-lapse fluorescence microscopy. The microscopy study provided a temporal evolution of these interactions that were statistically analyzed using variance-to-mean calculations and correlation analysis. The results demonstrate that bacterial growth can be regulated through surface wettability. A visual summary of the work is depicted in the mind map of figure 4.1.

Nanostructured bactericidal glass — Bactericidal / Normal

Regulate bacterial growth by surface wetting?
- bactericidal effect surface morphology & wettability
- in-silico studies
  - Experimental work
  - Direct observation

Prediction
- interaction using simulations
- Different effects from surface morphology and wettability
- Combination surface morphology with wettability most destructive (seen with viruses)

Equipment
- Molecular dynamics simulation (MDS) software
  - Martini v2.0 force field 4-to-1 coarse-grained (CG) procedure
  - GROMACS v.4.5.5 software package
- Glass substrate fabrication/ coating
  - Sputtering chamber (Cu)
  - Reactive ion etcher (RIE)
  - Chemicals
    - Hydro- and fluorosilanes
    - Toluene
- Surface characterization
  - Scanning electron microscope (SEM)
  - Contact angle (CA) measuring device
- Incubator for bacteria
- Spectrophotometer
- TIRF microscope
- Analysis software: Fiji

Safety

Fair Test
- How ?
  - Flat- and nanostructured glass
  - Effect from surface morphology?
- Why ?
  - Uncoated
  - hydrocarbon-coated (HC)
  - Fluorocarbon-coated (CF$_4$)
    - Hydrophobic (water repulsion)
    - Oleophilic (oil/fat attracting)
    - Hydrophobic
    - Oleophobic (oil/fat repellent)
  - Effect from surface wetting?

Method
- Experiments
  - MD Simulations
    - Construct lipid vesicle mimicking bacterium
      - Phospholipids
      - Cholesterol
    - Construct surfaces: flat, nanostructured, HC, FC
    - Simulation parameters similar to experiments
    - Measure CA
  - 1. Flat- and nanostructured glass, silanize, CA measurements
  - 2. Grow bacteria, dilute from O.D. 0.6 to 0.1
    - Membrane (FM4-64)
    - Nucleoid (SYBR Green I)
  - 3. Fluorescently stain E.coli
  - 4. Challenge E.coli with different substrates observe with TIRF microscope
  - 5. Statistical analysis
    - Variance-to-mean ratio
    - Correlation analysis

Result
- Partial disruption
  - Most destructive
    - Nanostructured glass
    - Hydrophilic + oleophilic
  - Flat and coated substrates
  - Uncoated nanostructured substrate
  - Hydrophobic + oleophobic substrates

Conclusion
- Nanostructured surfaces simultaneously hydrophobic and oleophilic have bactericidal effects
- Surface wetting is enhanced by silanization and regulates bacterial adhesion/growth

Evaluation
- Strengths
  - Understanding interactions at molecular level
  - Direct and more accurate observation bacteria - surface interaction at the macro level
- Weaknesses
  - Living sample, no destructive pre-treatment
  - MDS simplified model of real bacterium
  - No extensive study surface durability

Coulomb & van der Waals forces
- minimize intravesicle and surface interactions
- avoid collapse molecules

Figure 4.1. Mind map chapter 4. Transparent nanostructured bactericidal glass.

4.1 State-of-the-art and overall objective

Antimicrobial resistance and healthcare-associated infections remain pressing issues in society. Antimicrobial surfaces can play an important role to reduce microbial contamination of surfaces by preventing microbes to attach and/or kill attached microbes. A deeper understanding of the interaction mechanisms of bacteria with surfaces is essential to establish guidelines for antimicrobial surface design which can be impactful for orthopaedic implants, potent water systems, and objects in clinical settings. Ideal antimicrobial surfaces should be safe, long term, prevent biofilm formation, do not invoke resistance, work rapidly, and should be easy to fabricate and implement.[95,42] There are two main strategies to design antimicrobial surfaces: (i) built-in antibacterial agent release, (ii) surface topography combined with anti-adhesion/ bacteria-repelling properties.

(i)   Built-in antibacterial agent release

In coatings various agents with antimicrobial properties have been proposed and tested such as peptides, enzymes, antibiotics, quaternary ammonium compounds,[42,96,97,98] nanoparticles, graphene (oxide),[99,100,101] and metals[102]. Toxic doses of copper and silver metal ions are known to have antimicrobial effects, causing injuries to microbes through oxidative stress, protein dysfunction and membrane damage. A coating or porous material can be made antibacterial by soaking it into an antibacterial compound but also through carriers such as poly(methyl methacrylate) (PMMA), polyacrylic acid (PAA) or chitosan (polysaccharides from seafood).[42]

(ii)   Surface topography combined with anti-adhesion/ bacteria-repelling properties

Surface topography can be designed to be either antimicrobial, reducing cell viability, or anti-adhesive, reducing microbial attachment. Early work on nanostructures used for antimicrobial purposes include studies on cicada wings,[103] gecko skin,[104] black silicon,[105] and silicon. The nanospikes are assumed to be able to puncture the bacterial cell wall causing it to die. Over the years, these approaches have been further developed with many other materials tested and a plethora of methods used. Several recently published review articles provide a thorough overview on the state-of-the-art in this field.[106,107,108,109,110] These reviews summarize insightful findings but at the same time show that it is challenging to compare the different findings with each other because of the different experimental approaches there exists no unified standard to date to assess their performance. Bacteria-surface adhesion studies using nanostructured surfaces mainly used materials like silicon (Si), titanium dioxide (TiO_2), titanium (Ti), zinc oxide (ZnO), gold (Au), and PMMA.[110] Studies with nanopillars that exhibit bactericidal properties are reported to have heights of 100-900 nm, diameters of 20-207 nm, and interspaces of 9-380 nm.[110] Surface structures can be functionalized with silanes to tune their wettability thus making them more hydrophilic or hydrophobic to repel bacteria.[42]

In this chapter we present an in-depth study of bacterial interaction in relation to surface wettability. Our new approach predicts bacterial behavior based on in silico experiments using molecular dynamics simulation in combination with time-lapse fluorescence microscopy to directly observe how surfaces affect bacteria. In contrast, popular evaluation techniques involve indirect methods and are prone to artefacts. Scanning electron microscopy (SEM) is a widely used imaging method that

utilizes a beam of electrons to obtain high resolution three-dimensional images and provide information on the morphology, surface topography, chemical composition, and electrical behavior of non-living specimen under vacuum.[47] Bacterial colony forming unit (CFU) counting is time-consuming and imprecise because one cannot exclude cell aggregation and only colonies of bacteria that readily grow on a solid medium are counted.[59] Another method to assess bacterial cell viability of adherent cells is staining with DNA-intercalating fluorophore propidium iodide (PI). However, PI significantly underestimates cell viability because its uptake depends on the bacteria's physiological state and the presence of extracellular nucleic acids, requiring further confirmation by additional methods.[111,112] Sample processing involving washing, dipping, and centrifuging introduce undesired artefacts that result in cell damage and detachment from the surface.[113,114] These drawbacks motivated us to take a different direction through a quantitative approach with minimal experimental interference into the process of bacteria interacting with surfaces.

4.2 Methodology: experimental and modelling

We constructed a small simplified lipid vesicle having comparable chemical composition as bacterial membranes and studied its interaction with surfaces exhibiting different wetting behaviors using coarse-grained molecular dynamics simulation. Then we fabricated glass surfaces with nanopillars using reactive ion etching. To study how surface wettability, surface morphology or its combination influence bacterial behavior, the physicochemical properties of flat- and nanostructured surfaces were modulated using non-reactive self-assembling molecules (silanization). Surface wetting was assessed by contact angle measurements. The microscopy study provided a temporal evolution of bacteria-surface interaction that was statistically analyzed using variance-to-mean calculations and correlation analysis. Summarized as project workflow in figure 4.2.
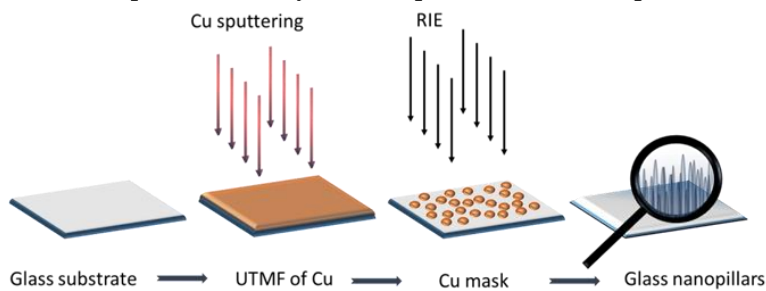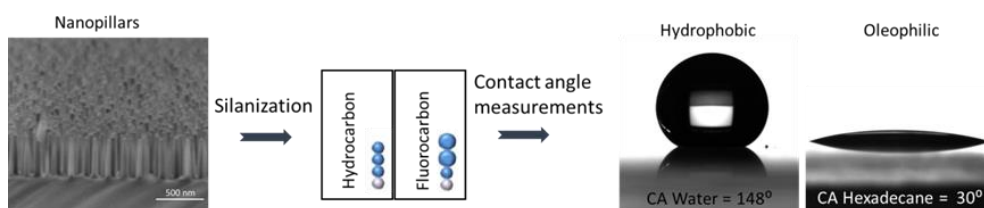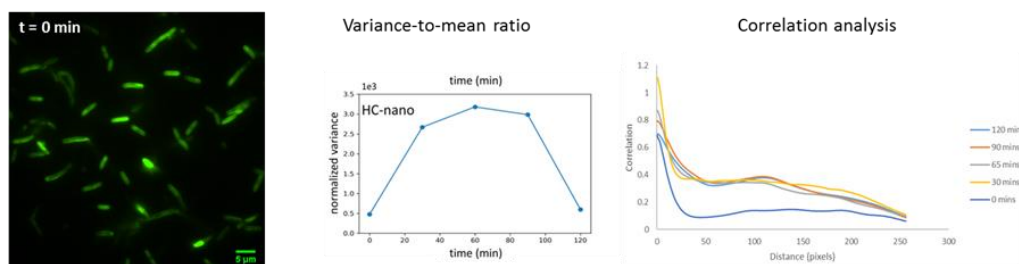
Figure 4.2. Experimental workflow. Obtained data, photos, and images do not necessarily correspond to each other but rather represent the result of different procedural steps in simulations and experiments.

4.3 Molecular Dynamics Simulation

Molecular dynamics simulation is known as a powerful computational technique for cell-surface interaction studies at the molecular level. Atomistic molecular dynamics simulation works with short time scales of a few hundred nanoseconds and short length scales of 10-20 nm. In contrast, the coarse-grained approach offers longer time- and length scales while conserving the molecular characteristics of simulated moieties.[115] Surface wetting properties can be tailored by morphology and chemical composition. By increasing the surface area through micro- or nanostructuring, hydrophobic surfaces can become superhydrophobic and hydrophilic surfaces can become more hydrophilic.[49] Conventionally, wetting states are divided into two groups. In the Cassie-Baxter state water remains on top of micro- and nanostructures, leaving air pockets between the structures while the Wenzel state describes water droplets that enter in between the surface structures.[116,117] Previous research had already shown that surfaces that simultaneously exhibit hydrophobic and oleophilic properties were able to deactivate enveloped Influenza A viruses. The effect was more pronounced in the Cassie-Baxter state through surface nanostructuring, increasing the effective surface area for self-assembling molecules to coat the surface and make it more hydrophobic / oleophilic and thus more attractive to phospholipids of cell membranes.[118] For the molecular dynamics simulations we applied the 4-to-1 coarse-grained (CG) procedure described in the Martini v2.0 force field[119] using the GROMACS v.4.5.5 software package.[120]

4.3.1. Lipid-vesicle construction

A lipid vesicle that mimics the bacterial cell membrane was constructed as a model to study its interaction with surfaces of varying wetting and morphological characteristics. The simulated vesicle was composed of 614 phospholipids (POPC) and 263 (30 mol %) cholesterol (Chol) molecules that formed a unilamellar (lipid bilayer) liposome with a diameter of 10 nm. The liposomes were hydrated with 71 552 water particles and equilibrated in an isothermal–isobaric ensemble at T = 310 K and p = 1 bar. Simulated vesicles in touch with the surfaces were assessed during 4 µs production runs. At equilibrium, the water density reaches stability around 980 g/l inside and outside the vesicle, no holes were observed and both leaflets of the lipid bilayer showed fluid behavior. Note that due to computational limitations, the constructed lipid vesicle is an extremely simplified model of the real bacterium which is bigger and more complex in nature. Simulated equilibrated lipid vesicles on top of self-assembled flat- and nanostructured surfaces at the start of the simulation are displayed in figure 4.3.
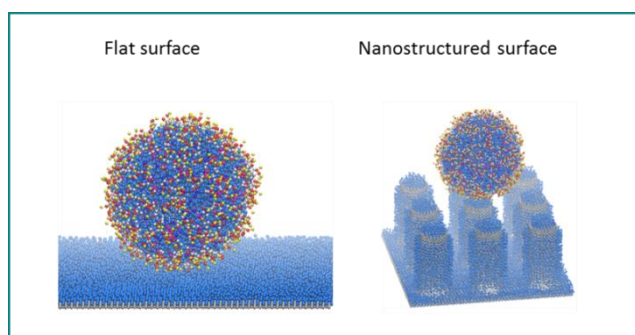
Figure 4.3. Simulation surface / vesicle model. Bacterium-mimicking lipid vesicle on flat- and nanostructured surface.

4.3.2. Surface construction and characterization with contact angle measurements

Simulated flat and nanostructured glass surfaces were modelled as compact $25 \times 25 \; nm^2$ surfaces composed of fixed and regularly placed silica-like particles. The nanostructured surfaces had a 3×3 array configuration with cylindrical nanopillars having a diameter of 4 nm and a height of 10 nm with a filling factor of 18%. The surfaces were coated with different moieties according to the type of silane used for experiments, where the first silane-like bead fixed unto the surface served as anchorage for other molecules. The hydrocarbon (HC) coated surfaces were coated with dodecane ($-$(CH2)11-CH3), formed by three CG apolar beads bonded to the fixed silane-like particle. The fluorocarbon (FC) coated surface, is similar to HC but the last two alkane particles were replaced by beads with equal apolar character having an increased particle radius of 35%, in agreement with atomistic simulations.[121] Attached molecules were separated by 0.5 nm, similar to experimental observations for alkylsilane monolayers.[122] Coulomb- and van der Waals forces minimized intravesicle and surface interactions and prevented collapse of the molecules. Flat (flat) and nanostructured (nano) glass surfaces were coated with either hydrocarbon (HC) or fluorocarbon (FC) moieties. Further adjustments were made to match the surface morphology and wetting properties of fabricated glass surfaces in the laboratory and were assessed by contact angles (CA) measurements. for water and hexadecane.

A simulation box of $50 \times 50 \; nm^2$ was used for contact angles (θ) measurements for water and oil (hexadecane). A square drop composed of 40,000 water particles or 10,000 hexadecane (HD) molecules, respectively was deposited onto the surface. Here, the nanostructured surfaces correspond to a 6×6 array of cylindrical glass nanopillars having the same dimensions described earlier. In short runs (100 ns) described in the simulation protocols in 4.3.3. explained it was possible to observe how water and hexadecane drops spread on the coated surfaces. The CA can be measured from the profile of a drop in equilibrium with the surface, except for drops that strongly wet the surface because they have irregular profiles that do not allow accurate measurements (~ low CA). The values obtained are listed in table 4.1.

Table 4.1. MD simulations measured contact angles (θ) for water- and hexadecane for FC- and HC-coated flat and nanostructured surfaces.

Substrate	θ_{water}	θ_{HD}
FC- Flat	~125^0	~80^0
HC-Flat	~105^0	~0^0
FC-NP	~150^0	~90^0
HC-NP	~120^0	~0^0

4.3.3. Simulation protocol

The GROMACS v.4.5.5 software package was used for simulations[120] with periodic boundary conditions applied in the x and y directions, a fixed temperature of 310 K, and with x, y planes kept constant. Surface particles and the first bead of the attached 'silane molecule' remained in fixed positions during simulation. Coulomb and van der Waals forces used a cut off at 1.2 nm prevented inter-particles interactions from different molecules. Shifted Coulomb potential energy was used for electrostatic interactions where charges had a relative dielectric constant of 15. Simulations were run for 4 μs. To meet numerical accuracy of the molecular dynamics simulation, the integration step time was set to 20 fs. The CG method has an inherent 'smoothing' procedure to reduce the simulation time and was set to a standard speed-up factor of 4 in our simulations.[119] Water freezing was prevented with 15% of anti-freeze waters.[119] The simulation is limited for non-coated glass surfaces because even with the use of anti-freeze particles, freezing still occurs. Thus, non-coated glass surfaces were not included for simulations.

4.3.4. Simulation results

Surfaces coated with hydrocarbons are simultaneously hydrophobic (water repellent) and oleophilic (attracting fat) while fluorocarbon molecules are both hydrophobic and oleophobic (repelling fat). The temporal sequences of the interaction of a lipid vesicle with flat HC-and FC-coated surfaces are depicted in figure 4.4 The HC-flat substrate shows that de lipid vesicle evolves into a dome-like structure that over time completely disintegrates and the fatty part of the phospholipids cover the surface, whereas the FC-flat substrate shows only partial disruption leaving the vesicle as a dome-like structure on the surface. On surfaces that were nanostructured and coated with either HC or FC, the effect from the surface on the vesicle was stronger as seen in figure 4.5. On FC-nano surface, the dome-like structure was deformed but the lipid vesicle was not completely destroyed. In contrast, the HC-nano substrate resulted in a rapidly disintegrated vesicle without forming an intermediate state first. This is further visualized in figure 4.6 by the strong drop in the potential energy for HC-nano compared with the other surfaces. Once the vesicle ruptures, hydrophobic attraction between the hydrophobic-oleophilic surface and the phospholipids of the vesicle becomes stronger than the interaction with water. Consequently, the phospholipids from the destructed vesicle coat the surface and the total free energy of the system is reduced compared to an intact vesicle in solution. In the case of FC coated surfaces which are hydrophobic but also oleophobic, the interaction between the fatty phospholipids is less favorable and the hydrophobic attraction is less compared to HC molecules, this explains why the vesicles are only partially disrupted. In summary, the simulation results show the cumulative effect of intermolecular forces encompassing van der Waals, hydrophobic, and electrostatic effects that arise from the vesicle/ surfaces interactions and how they lead to either partial disruption or complete disintegration of the phospholipid double layer of the vesicle induced by the wetting and morphology characteristics of the surface.
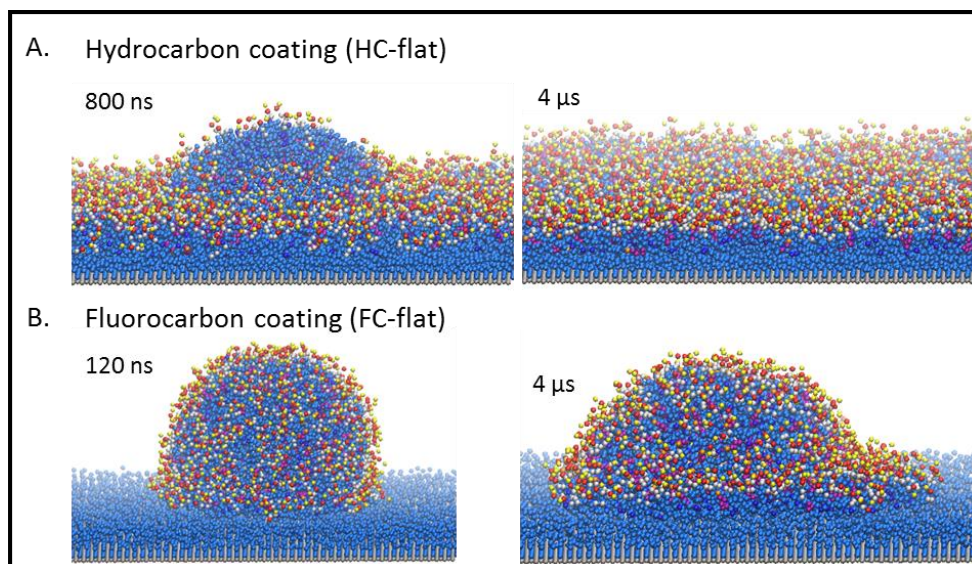
Figure 4.4. Molecular dynamics simulation for flat surfaces. Temporal sequences of lipid vesicle interactions with A. a hydrocarbon-coated surface leading to total disruption of the vesicle and B. a fluorocarbon-coated surface showing partial disruption of a vesicle that remains like a dome-like structure on the surface.
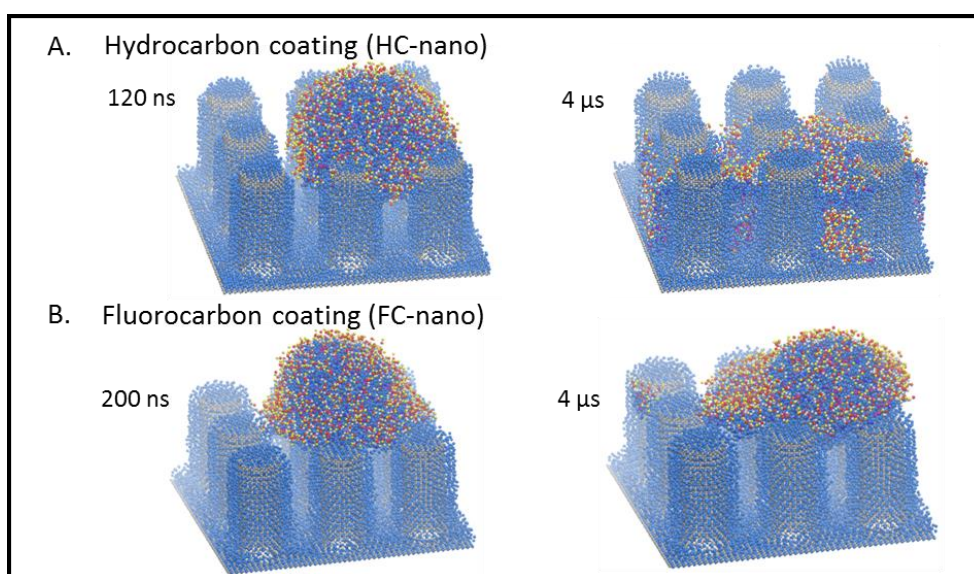
Figure 4.5. Molecular dynamics simulation for nanostructured surfaces. Temporal sequences of lipid vesicle interactions with nanostructured surfaces of a 3×3 array of cylindrical nanopillars (height = 10 nm, diameter = 4 nm) A. Action mode of hydrocarbon-coated nanopillars leading to total disruption of the vesicle. B. Action mode of fluorocarbon-coated nanopillars leading to partial disruption of the vesicle.
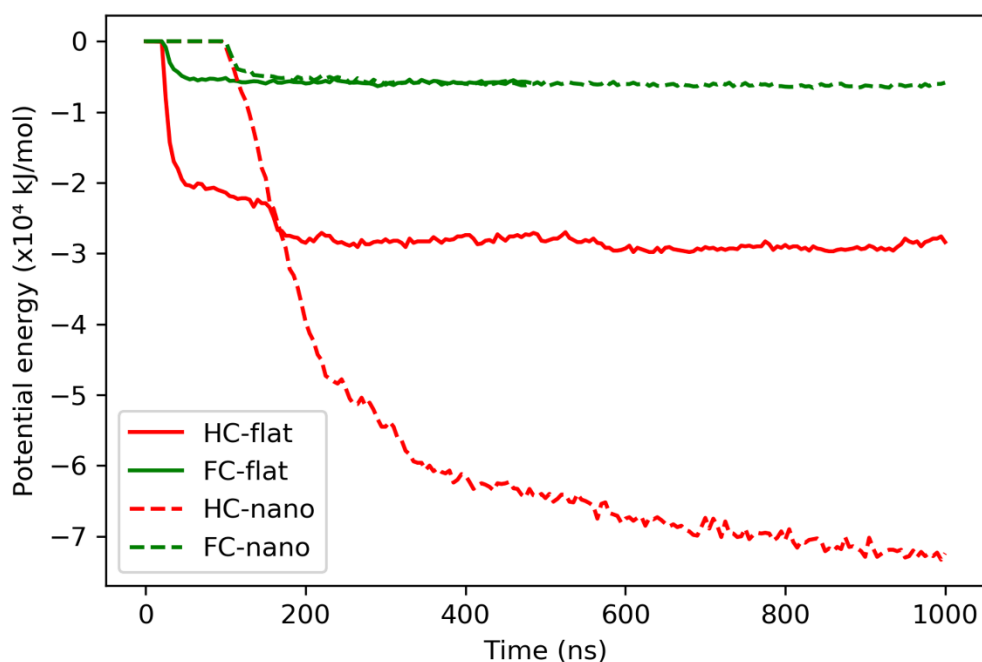
Figure 4.6. Temporal energy evolution of lipid vesicle interaction with various coated surfaces. Fluorocarbon moieties in green and hydrocarbon in red of flat (solid lines) and nanostructured (dotted lines) surfaces. The highest higher energy drop (5x104 kJ/mol) is seen for the vesicle interacting with an HC-nano surface. This interaction is stronger than of the vesicle with fluorocarbon moieties (0.5x104 kJ/mol), indicative for the stronger disruptive effect arising from HC coated surfaces that attracts to the phospholipids from the vesicle.

4.4. Surface fabrication, functionalization, and characterization.

Surface fabrication. Surfaces were nanostructured using reactive ion etching (RIE) as described by Infante et al.[123] First , borosilicate glass surfaces (Schott) of 0.1 mm thick were cleaned with oxygen plasma (700 W, 300 ml/min, 13 min) and a 6 nm copper film was sputtered unto it. After thermal dewetting, the little copper islands that were obtained served as a mask during etching with RIE. Scanning electron microscopy (FEG-SEM, Inspect F, FEI Systems) was used for morphological and dimensional analysis. The images were analyzed with the particle analysis tool using Fiji software.[70] The fabricated pillars had average dimensions of about 250 nm in height and 100 nm in diameter, and a surface filling factor of 18%.

Surface functionalization and characterization. To tune the surface wettability, flat and nanostructured glass surfaces were subjected to oxygen plasma and then directly immersed in MilliQ water for 30 min to maximize –OH groups on the surface. After drying we performed wet chemistry silanization. Briefly, hydrocarbon trichloro(octadecyl)silane (HC), and fluorocarbon trichloro (1H,1H,2H,2H-perfluorooctyl)silane (FC) silanes (Sigma-Aldrich) were prepared at a concentration of 5 mM in toluene and left overnight. The next day, all samples were rinsed in toluene, then in Milli-Q water and finally, dried with nitrogen gas and stored under vacuum until needed for experiments. Static contact angles of water and hexadecane were measured using the Krüss GmbH DSA100 drop shape analyzer and then averaged. Detailed analysis of contact angles of water and hexadecane (θ_{water} and θ_{HD}) can be found in our previous publications, in particular in Infante et al 2013 (FC-family) and Mannelli et al 2016 (HC family).[123,124]

Table 4. 2. Experimental contact angle (θ) values for water and hexadecane for FC- and HC-coated flat and nanostructured surfaces.

Substrate	θ_{water}	θ_{HD}
FC- Flat	~110^0 -120^0	~75^0
HC-Flat	~100^0 -110^0	~40^0
FC-NP	~150^0	~110^0
HC-NP	~150^0	~30^0

4.5 Time-lapse fluorescence microscopy and statistical analysis

Bacterial staining and imaging settings. Bacteria were grown and stained with both SYBR Green I (nucleoid) and FM4-64 (membrane) as described in the sections 2.4. Image acquisition was performed as described in the previous sections 2.4 and 3.5 with the following adjustments. A laser power range of 0.0166 to 0.002 mW was used for excitation with wavelength 488 nm and 0.014 – 0.002 mW for excitation with wavelength 560 nm. Glass surfaces were mounted, a background image was captured, and then 50 μl of stained *E.coli* suspensions was added. Images were acquired within 3 min after *E.coli* deposition unto the glass (time 0). Then for 2 hrs every 30 mins images were captured. The FOV was kept the same for each condition throughout the 2hrs of acquisition.

Control surfaces were included to assure that the observed effects on bacteria were arising from surface morphology and/or wettability. Figure 4.7 displays the spatio-temporal evolution of bacteria on a bare glass surface. This negative (-) control shows gradual increase in cell density over time (30, 60, and 120 min), indicating a normal cell growth over the entire FOV. Artificially added colors with the membranes in cyan and the nucleoids in red with the scale representing 5 μm. Comparison of all the fabricated surfaces in figure 4.8 and figure 4.9 was done against the (-) control. Results confirm the findings obtained with simulations except for HC-flat which shows incomplete disruption, possibly due to the more complex nature of the real bacterium which might require more time before complete disruption can be noticed. Clustering is more profound for HC-flat compared to FC-flat implying stronger interactions with hydrocarbons. For all the fabricated surfaces structured and/or coated, bacterial behavior was altered and causing cell re-orientation, clustering, growth inhibition and for HC-nano, the most severe case, this led to cell disappearance.
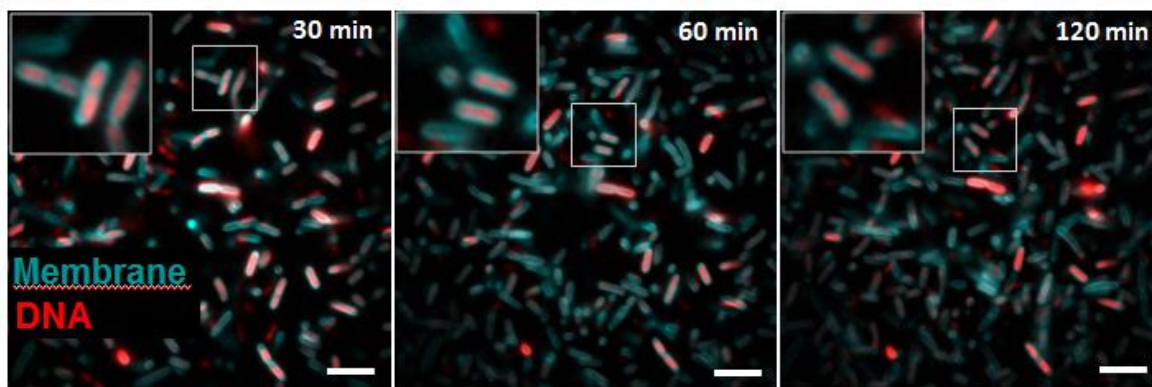
Figure 4.7. Time-lapse images of *E.coli* on a bare glass substrate. Normal growth evolution over time with glass as negative control. Membranes in cyan and DNA in red, scale bar is 5 µm.
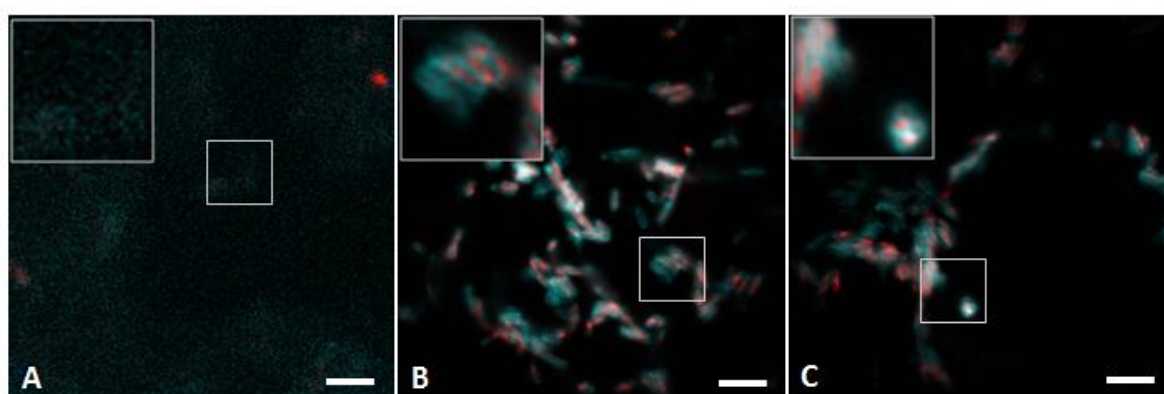
Figure 4.8. Time-lapse images of *E.coli* on flat glass surfaces at time 120 min. A. Positive control where 2% SDS was added to kill all bacteria. B. Fluorocarbon-coated flat substrate (FC-flat) that induced cell clustering and partial cell rupture seen in fluorescence spreading. C. Hydrocarbon-coated flat surface (HC-flat), caused cell clustering, rounding-up of cells and fluorescence spreading indicating cell membrane damage. Color code similar to figure 4.7 and scale bar 5 µm.
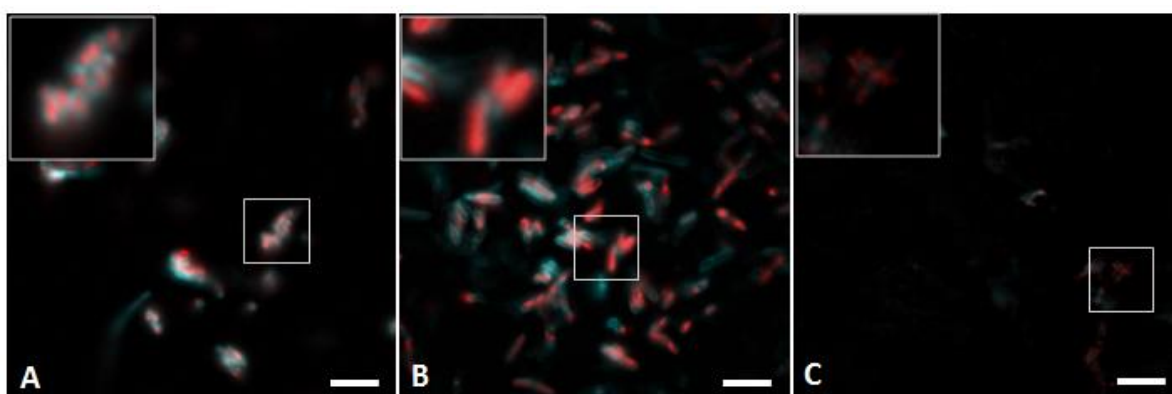
Figure 4.9. Time-lapse images of *E.coli* on a nanostructured glass surfaces at time 120 min. A. Uncoated nanostructured glass substrate induced strong cell clustering, deformation, and cell damage leading to fluorescence spreading. B. Fluorocarbon-coated nanostructured substrate (FC-nano) that induced cell clustering and partial cell rupture causing fluorescence leakage, many cells lost the membrane staining in cyan color. C. Hydrocarbon-coated nanostructured surface (HC-nano), caused total cell rupture and killed bacteria. Color code similar to figure 4.7 and scale bar 5 µm.

Variance-to-mean ratio (VMR) analysis. VMR is a statistical method to study the spatial distribution of biological specimen in a given image and is denoted as:

$$VMR = \frac{\sigma^2}{\mu}$$

Where σ^2 is the variance of pixel intensities and μ their mean. A VMR < 1 reflects no clustering, VMR = 1 describes a random distribution equal to Poisson distribution, and VMR > 1 is an indication for cluster formation. Translated to our work the variance of pixel values (σ^2) in an image were determined and divided by the mean pixel value (μ), which was done for all the different time points (0, 30, 60, 90, and 120 min). This allowed us to observe how the pixel intensity distribution changed over time in a given field-of-view (FOV). We performed the analysis for nucleoid staining as well as for the membrane staining. Pixel intensity distribution changes over time are presented in figure 4.10. This graphical aid shows that HC-nano rapidly exceeds VMR > 1, remains around VMR 3 for about 70 mins and then substantially declines to a VMR < 1, thus followed a pattern of no-clustering (single cells), clustering (cell aggregates), no clustering (disintegrated cells), confirming that the VMR can be used to evaluate cell clustering in our experiments. The other conditions show a different pattern, no clustering at the beginning of the experiment to VMR > 1, clustering after 30 min but the increase in VMR values was not as significant as for HC-nano glass. The results for DNA are slightly shifted as DNA remains protected until the membrane is damaged / ruptured before it becomes accessible to the surface. Note that studies on the staining efficiency and its relation to the precise intensity is beyond the scope of this work.
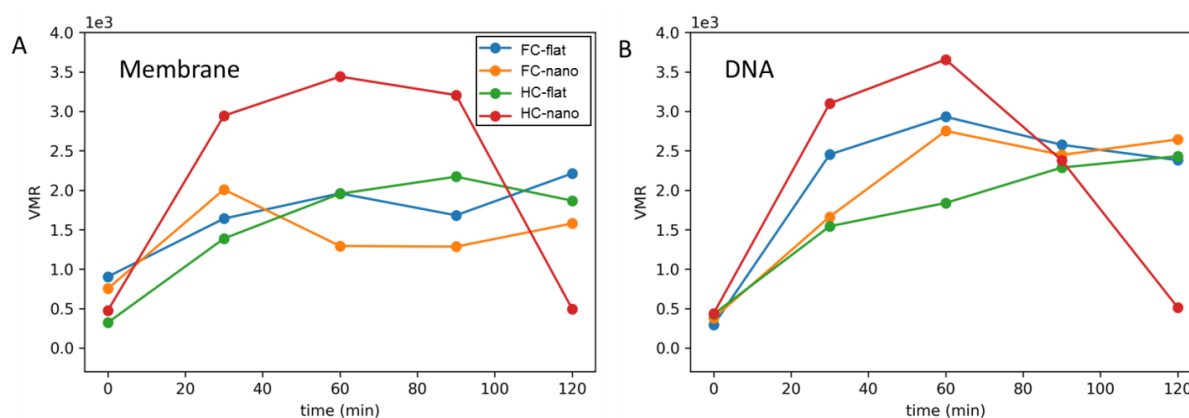
Figure 4.10. Temporal variance-to-mean ratio plots of pixel intensity distribution. Representing the degree of cell clustering with VMR < 1 no clustering and VMR > 1 clustering for A. membrane and B. DNA features.

Image autocorrelation analysis (IAA). Spatio-temporal changes in the digital images were also assessed through autocorrelation analysis to quantify bacterial growth or disappearance. IAA was only performed on the region of interest, the center of the image FOV, to minimize the effect of non-uniform illumination. The IAA analysis produces a correlation curve which is described by the convolution of the microscope's point-spread function (PSF)[125] which is assumed to follow a Gaussian PSF profile in the x-y plane. Therefore, we obtain the following correlation function:

$$g(r) = A * exp\left[\frac{-r^2}{4s^2}\right] + 1$$

where the amplitude, *A* depends on the density of subdiffraction objects, their brightness and the background level, whereas the spatial scale, *s* is determined by the microscope's resolution. When objects possess a cylindrical symmetry and sizes larger than the microscope's resolution, the parameter *s* provides an estimate of the object's characteristic size, in our case, the fluorescent bacteria (clusters). Thus, the amplitude refers to the *density* of cells clusters while the spatial scale is linked to changes in the *size* of cell clusters. The correlation function was fitted using a custom code written in Matlab (R2018b, The Mathworks) with the free parameters amplitude *A* and the spatial scale s, including a constant offset. To test IAA we first evaluated synthetic images obtained by randomly generating rod-like structures in a 2-dimensional binary map of $256 \times 256 \ pixels^2$ with an uniform distribution of angles. Then the images were convoluted with a Gaussian kernel and corrupted with Gaussian noise. Figure 4.11 shows a density increase in bacteria (A) with its corresponding correlation plot (C), a slightly increasing amplitude (E) (the density of the rods), and spatial scale (F) remaining low for the negative control, representing living bacteria. In contrast, in the case of the positive control, bacteria disappear and 'fluorescence' is spreading causing a decrease in the amplitude value and an increase in the spatial scale value.
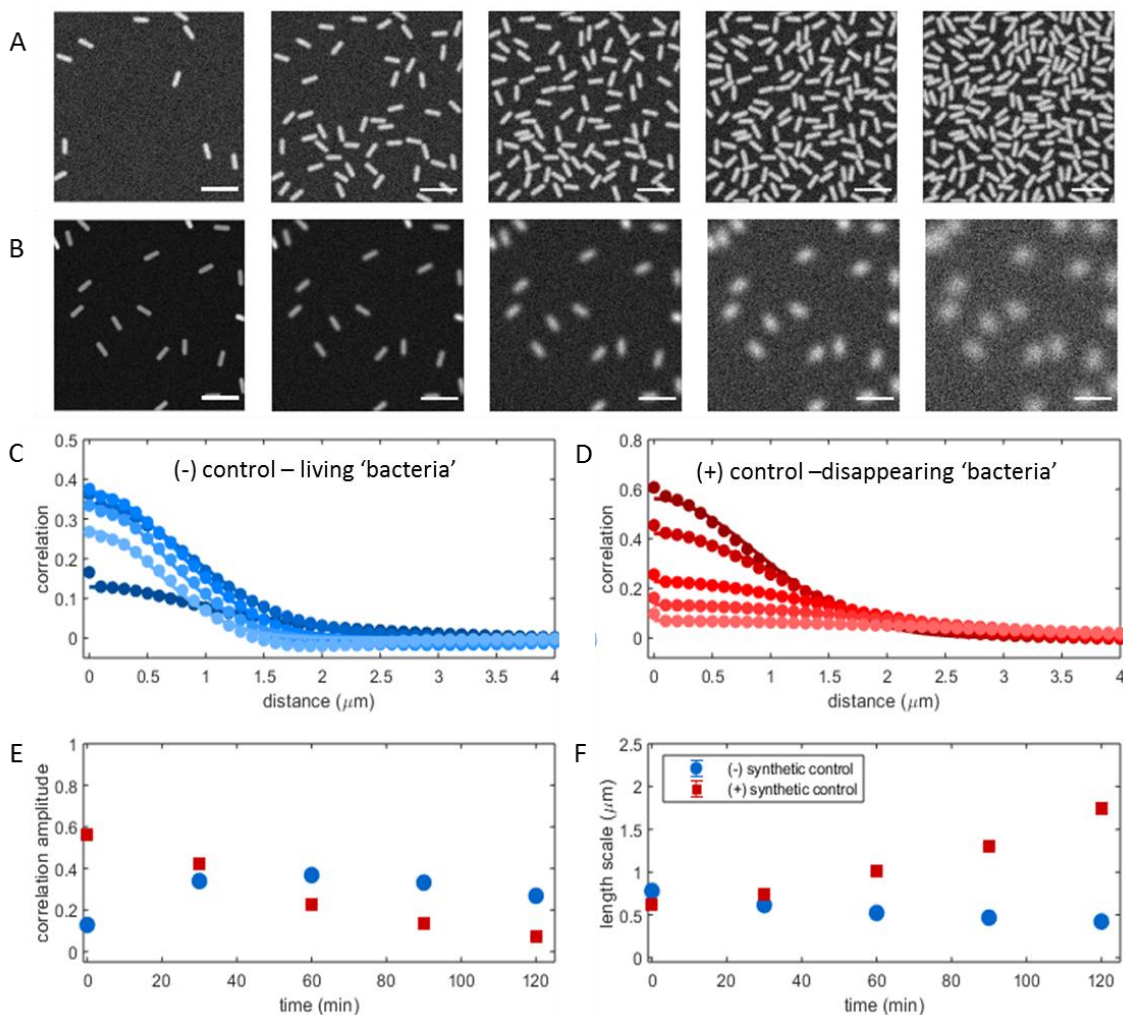
Figure 4.11. Synthetic images to test image correlation, fit, and interpretation. Time evolution of A. objects that increase in density over time representing normal bacterial growth and B. objects that lose their integrity reflecting fluorescence spreading due to bacterial death. C.D. Correlation fit to A and B, respectively and E.F. the corresponding correlation amplitude (density of clusters) and length scale (size of clusters) parameters. These results confirm that the Gaussian model provides a good approximation for the fit of the correlation curves. Scale bars 10 µm.

Next, we performed IAA on our real control samples. The (-) control refers to living bacteria, the (+) control to dying/ disappearing bacteria, and glass-nano is uncoated nanostructured glass that induced bacterial cell clustering. The results are depicted in figure 4.12 were the (-) control with increasing bacteria density in time reflects a reduction in the correlation amplitude with little change in the length scale ($s \sim 0.6$ µm). However, for the (+) control with 2% SDS the initial positive correlation s = 0.8 µm rapidly decreased to almost zero, hence the length scale cannot be defined, i.e., graphically presented. This reflects fluorescence spreading over larger areas due to cell disruption and cell death. Glass-nano displayed a progressive increase of the correlation amplitude and scale over time because bacteria formed clusters which size increased up to s = 1.5 µm. These results confirm the IAA approach can be applied to our data.
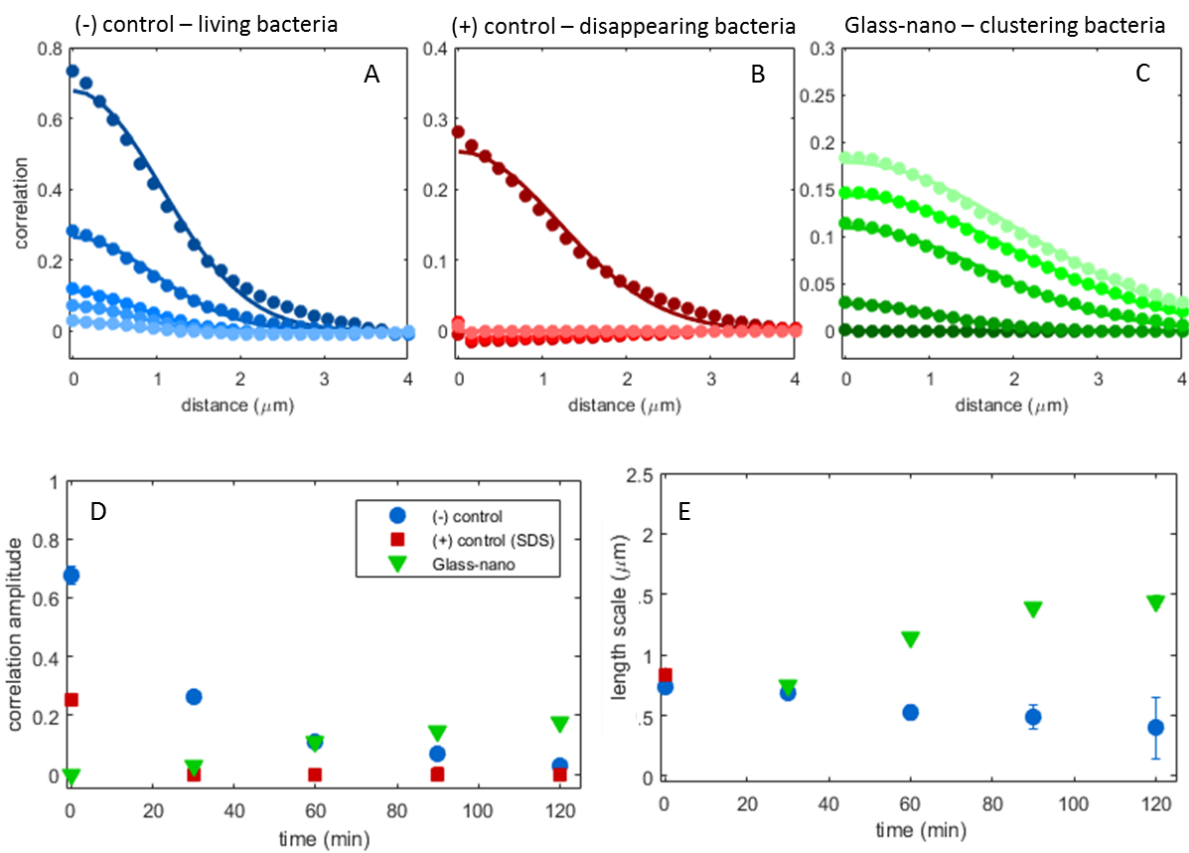
Figure 4.12. Autocorrelation analysis of bacteria on control substrates. Offset-subtracted correlation curves of bacteria on A, (-) control, B, (+) control (2% SDS), and C, glass-nano substrates at different times. Lighter colors correspond to later times; lines correspond to fitting curves. The parameters, correlation amplitude (D) and length-scale (E) were derived from the fit of the correlation curves for the different substrates. Error bars correspond to 99% confidence interval. Scale bars: 5 µm.

The validated IAA to analyse was then applied to the other surfaces with varying wettability and morphology (figure 4.13). For FC-flat and FC-nano only small changes were observed most likely due to a more limited clustering effect linked to partial disruption. The lower value of correlation amplitude observed for FC-nano seems to favor bacterial attachment but does not cause them to organize into clusters (lower spatial scale, s = 0.9 µm) with respect to the FC-flat case (1.5 µm). Also, AAI confirms that HC induces faster clustering of bacteria on both HC-flat and HC-nano surfaces. In fact, correlation curves obtained for HC-flat and HC-nano showed a bimodal decay that can be fitted

by a two-component model, each of them with its characteristic length scale. The larger length-scale (*s* = 7 μm) is due to a supra-cluster organization induced by the high bacterial density (-4.13A,B). Note that the data associated to the fit of the short-scale correlation (s = 1.5 μm), where one can observe for both substrates a time-dependent modulation of the correlation, showed a maximum at 30 min followed by a decay. This decay, indicating a nearly total bacterial death/disappearance, is more evident for HC-nano than HC-flat.
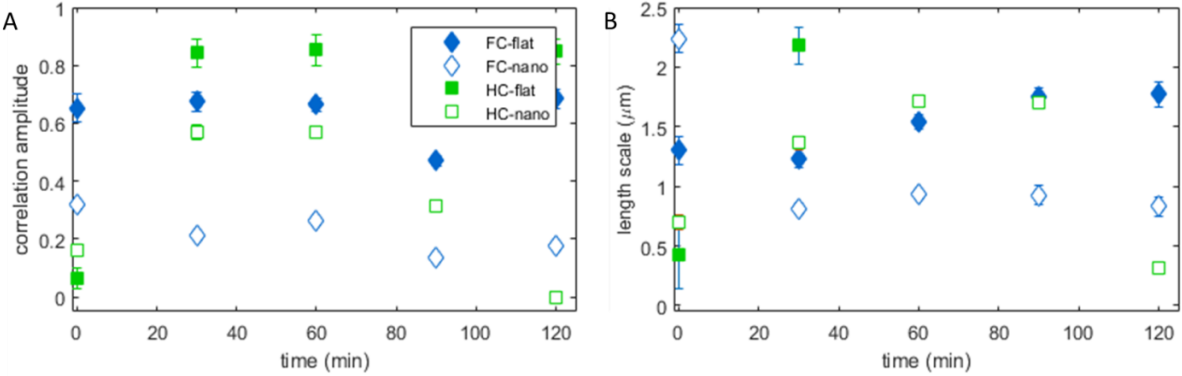
Figure 4.13. Autocorrelation analysis of time-lapse images of bacteria on different substrates. Correlation curves were fitted for different substrates obtaining the corresponding A. correlation amplitude and B. length-scale. Error bars correspond to 99% confidence interval.

4.6. Conclusion and outlook

This study aimed to contribute to the growing field of antimicrobial surfaces by performing in silico- and laboratory experiments. This combination of molecular dynamics simulations and time-lapse fluorescence imaging allowed direct differentiation and correlation of bactericidal effects that arise from either surface morphology, wetting or both. Molecular dynamics simulation offers the advantage to precisely tune surface geometry and wettability, so that bacterial interactions with such surfaces can be predicted and provide design rules for experiments. Here, we used a simplified lipid vesicle that mimics the bacterial membrane and studied its interaction with coated and non-coated flat- and nanostructured surfaces.

First, molecular dynamics simulations were used as a predictive tool to study adhesive and destructive characteristics of coated and patterned surfaces on a bacteria-mimicking vesicle, offering the advantage to precisely tune the geometry of the surfaces to achieve specific inter-actions and thus reducing lab work. Then, we experimentally assessed and statistically evaluated the molecular dynamics predictions of the membrane-surface interactions through the quantification and visualization of the results obtained through time-lapse fluorescence microscopy. The main feature of the latter is that bacteria from the exponential growth phase were stained with fluorescent dyes that diffused into either the membrane or the nucleoids, added to test substrates and immediately monitored with the microscope. The advantages are twofold. First, we avoid experimental procedures such as washing and centrifuging that unintentionally introduce artefacts. Second, we observe the evolution of the bacteria in time that can reveal cell re-orientation, clustering, growth inhibition and in the most severe case cell disappearance. Instead, current methods are mainly based on propidium iodide staining which relies on the cell membrane permeability, leading to significant drawbacks. For example, underestimation of cell viability because of the reversible permeability of propidium iodide ions and the presence of extracellular nucleic acids.[111,126,126] Though many evaluation methods and international standards are available and have their own strength, directly observing processes as they unfold in a reliable manner enhances our understanding on bacteria-surface interactions. Furthermore, our approach allows us analysing the data straightforwardly (in about one hour) using variance-to-mean calculations and image processing. Future work could involve imaging using z-stacks to obtain 3D information or videos to determine the diffusion coefficient. Moreover, Gram-positive bacteria possess a thicker and stronger external membrane and could respond differently to our tested surfaces so future work should also include bacteria from this category. The morphology of our nanostructured glass substrates could be further modified by varying the height to study the effect on bacteria under time-lapse conditions. Another approach worth studying could include the addition of bactericidal metal particles[102] to hydrocarbon-based coatings and evaluate the relation between concentrations and time scales of the killing effect on bacteria. Though the interaction of bacteria with surfaces is highly dynamic, real-time studies with minimal perturbation to these interactions provide more insight into spatial- and temporal evolution that could be further elucidated through molecular dynamics simulations. The presented results indicate that the proposed method will enable an effective evaluation of antimicrobial surface products for applications in healthcare and public electronic devices.

Chapter 5: Conclusions and future outlook

In this thesis we have presented a comprehensive approach to study the interaction and optical properties of bacteria on surfaces.

In **chapter 1**, we introduced the multidisciplinary character of the work, the state-of-the-art surface fabrication techniques, bacteria methodology, and imaging. In the following chapters, we focused on bacterial growth monitoring, enhanced bacterial detection, and bacterial-surface interactions on nanostructured surfaces.

In **chapter 2**, we validated a novel optical bio-sensing device that allowed us to monitor bacterial growth over time. The surface cytometer was demonstrated to be consistent with the routinely-used laboratory techniques spectrophotometry and microscopy by means of generating bacterial growth curves showing similar trends. The surface cytometer can measure average fluorescence intensity signal over a large field-of-view (about 200 mm^2) - roughly 10 times more than the spectrophotometer - and a large depth of field (about 2 mm), within 1 minute and without complex post-processing. Its limit-of-detection is around 10^4 cells/mm^2 and compares well with state-of-the-art techniques. These combined features point out the potential of the surface cytometer as rapid, compact, and inexpensive device that could be used for applications that require in-situ measurements and point-of-care testing.

In **chapter 3**, we proposed a novel transparent surface with an ultrathin gold film to quench background fluorescence and improve the signal-to-noise ratio in microscopy digital imaging. Numerical calculations have been presented, showing the evolution of distance-dependent quenching of fluophores. The lifetime of a fluophore in proximity of an ultrathin metal quencher (UTMQ) surface is strongly reduced, predominantly in the near field ($\leq$ 10 nm from the surface), and gradually increases at longer distances, reaching similar values compared with glass in the far field (> 100 nm). Experimentally, we have achieved improved SNR values for bacteria in moist using confocal microscopy, microspheres in water using total internal reflection microscopy, and proteins in air using surface cytometry, confirming to be in line with the numerical calculations. A higher signal-to-noise ratio (SNR) harvests more photons leading to higher localization precision at lower laser powers and shorter acquisition times. UTMQ film stability was enhanced through a SiO$_2$ spacer of 5 nm thick that in combination with an improved SNR could further extend the application of these surfaces to super-resolution microscopy and live-cell imaging, which require high localization precision of specimen in buffers with minimal photodamage.

In **chapter 4**, we demonstrated that bacterial growth can be regulated by surface wettability and presented a method that combines molecular dynamics simulation to predict bacteria-surface interactions at the molecular level with time-lapse fluorescence microscopy for direct observation of these interactions. We found that surface nanostructures, coated with silane molecules that make the surface simultaneously hydrophobic and oleophilic, are disruptive for bacteria and cause them to die. The hydrophobic molecules on the surface repel the bacterial suspension while the simulations have shown that the oleophilic part of the surface prefers to interact with the fatty parts within the bacterial membrane. These combined observations provide a more accurate analysis of bacteria-surface interaction and shows bactericidal effect that stems from surface morphology and wettability.

In summary, the work presented in this thesis has contributed to the field of antimicrobial resistance by monitoring bacterial growth on surfaces with a novel device, enhanced detection of bacteria with microscopy, and showed various interaction mechanisms of bacteria with flat- and nanostructured surfaces to reduce their viability.

We foresee several future directions.

- To apply the surface cytometer to real life settings will require an in-depth testing of different biological samples and consider the quantity of material that could be collected to achieve reliable readouts.
- Further enhancement of the SNR in digital images using UTMQ will need an in-depth study of the film stability for live cell applications that make growth on surfaces possible over several days. Another improvement will come from the uniformity of the protective SiO_2 layer.
- For the surfaces that demonstrated to have bactericidal properties, further studies on their robustness, repeatability, and durability will be needed to work towards real life applications. Varying the height of the nanopillars could be another interesting parameter to study if this advances the killing rate of bacteria. Video acquisition is useful to determine the diffusion coefficient. More insight into kinetic- and thermodynamic processes involved in bacterial cell-surface adhesion could be acquired using techniques like quartz crystal microbalance (QCM) and surface plasmon resonance (SPR) for affinity studies. Another technique could be Raman spectroscopy which provides vibrational information of bacteria.

In summary, the work presented in this thesis has contributed to the field of antimicrobial resistance by monitoring bacterial growth on surfaces with a novel device, enhancing detection of bacteria with microscopy, and revealing various interaction mechanisms of bacteria with flat- and nanostructured surfaces to reduce their viability. It will be the basis for future design of nano-structured surfaces with antimicrobial activity that also possess other properties, e.g. antireflection. At the same time, the devices and techniques for imaging on a surface presented in the thesis can be developed further for real-time monitoring of bacterial growth in practical settings.

Bibliography

(1)   Observations, Communicated to the Publisher by Mr. Antony van Leeuwenhoeck; The Royal Society, 1676; pp 821–831.

(2)   Fransen, S. Antoni van Leeuwenhoek , His Images and Draughtsmen. **2019**, *27* (3). https://doi.org/10.1162/posc.

(3)   Hooke, R. Micrographia or Some Physiological Description of Minute Bodies by Magnifying Glasses with Observations and Inquiries Thereupon. London 1664.

(4)   Laboratories, P. U. C. Curriculum vitae published at the occasion of Johan Sebastian Ploem receiving the Ernst Abbe Medal and Award from the New York Microscopical Society in the USA, November 17, 1998. http://www.cyto.purdue.edu/cdroms/cyto10a/cytometryhistory/individualhistories/ploem.html (accessed Jul 21, 2021).

(5)   Griffiths, D. J. *Introduction to Electrodynamics*; Reeves, A., Ed.; Prentice Hall: Upper Saddle River, 1999.

(6)   Sliney, D. H. What Is Light ? The Visible Spectrum and Beyond. **2016**, 222–229. https://doi.org/10.1038/eye.2015.252.

(7)   Wegerhoff, R.; Weidlich, O.; Kassens, M. Basics of Light Microscopy & Imaging: Special Edition of Imaging & Microscopy. **2008**, 10.

(8)   Campoccia, D.; Montanaro, L.; Arciola, C. R. A Review of the Biomaterials Technologies for Infection-Resistant Surfaces. *Biomaterials* **2013**, *34* (34), 8533–8554. https://doi.org/10.1016/j.biomaterials.2013.07.089.

(9)   Marrie, T. J.; Nelligan, J. A Scanning and Transmission Electron Microscopic Study of an Infected Endocardial Pacemaker Lead Fim. **1982**, No. 6, 1339–1341.

(10)   Ravi, S.; Zhu, M.; Luey, C.; Young, S. W. Antibiotic Resistance in Early Periprosthetic Joint Infection. **2016**. https://doi.org/10.1111/ans.13720.

(11)   Malhas, A. M.; Lawton, R.; Reidy, M.; Nathwani, D.; Clift, B. A. ScienceDirect The Surgeon , Journal of the Royal Colleges of Surgeons of Edinburgh and Ireland Causative Organisms in Revision Total Hip & Knee Arthroplasty for Infection : Increasing Multi- Antibiotic Resistance in Coagulase-Negative Staphylococcus and T. *Surg.* **2014**, *13* (5), 250–255. https://doi.org/10.1016/j.surge.2014.04.002.

(12)   Boyce, J. M. Environmental Contamination Makes an Important Contribution to Hospital Infection. *J. Hosp. Infect.* **2007**, *65* (SUPPL. 2), 50–54. https://doi.org/10.1016/S0195-6701(07)60015-2.

(13)   Han, J. H.; Sullivan, N.; Leas, B. F.; Pegues, D. A.; Kaczmarek, J. L.; Umscheid, C. A. Cleaning Hospital Room Surfaces to Prevent Health Care-Associated Infections: A Technical Brief. *Ann. Intern. Med.* **2015**, *163* (8), 598–607. https://doi.org/10.7326/M15-1192.

(14)   Faria, S. I.; Teixxeira-Santos, R.; Romeu, M. J.; Morais, J.; Vasconceles, V.; Mergulhão, F. J. The Relative Importance of Shear Forces and Surface Hydrophobicity on Biofilm Formation By. *Polymers (Basel).* **2020**, *12* (653).

(15)   Bixler, G. D.; Bhushan, B. Biofouling : Lessons from Nature. *Philos. Trans. R. Soc. A Math. Phys. Eng. Sci.* **2012**, *370* (1967), 2381–2417. https://doi.org/10.1098/rsta.2011.0502.

(16)   Hunsucker, K. Z.; Vora, G. J.; Hunsucker, J. T.; Gardner, H.; Leary, D. H.; Kim, S.; Lin, B.; Swain, G.; Hunsucker, K. Z.; Vora, G. J.; Hunsucker, J. T.; Gardner, H.; Leary, D. H.; Kim, S.; Lin, B.; Swain, G. Biofilm Community Structure and the Associated Drag Penalties of a Groomed Fouling Release Ship Hull Coating. *Biofouling* **2018**, *7014*, 1–11. https://doi.org/10.1080/08927014.2017.1417395.

(17)   Schultz, M. P.; Bendick, J. A.; Holm, E. R.; Hertel, W. M.; Bendick, J. A.; Holm, E. R.; Hertel, W. M. Economic Impact of Biofouling on a Naval Surface Ship. **2011**, *7014*. https://doi.org/10.1080/08927014.2010.542809.

(18)   Law, J. W.; Mutalib, N. A.; Chan, K.; Lee, L. Rapid Methods for the Detection of Foodborne Bacterial Pathogens : Principles , Applications , Advantages and Limitations. **2015**, *5* (January), 1–19. https://doi.org/10.3389/fmicb.2014.00770.

(19)   O´Neill, J. et al. Tackling Drug-Resistant Infections Globally: Final Report and Recommendations. *Rev. Antimicrob. Resist.* **2016**, 84.

(20)   Cassini, A.; Högberg, L. D.; Plachouras, D.; Quattrocchi, A.; Hoxha, A.; Simonsen, G. S.; Colomb-Cotinat, M.; Kretzschmar, M. E.; Devleesschauwer, B.; Cecchini, M.; Ouakrim, D. A.; Oliveira, T. C.; Struelens, M. J.; Suetens, C.; Monnet, D. L.; Strauss, R.; Mertens, K.; Struyf, T.; Catry, B.; Latour, K.; Ivanov, I. N.; Dobreva, E. G.; Tambic Andraševic, A.; Soprek, S.; Budimir, A.; Paphitou, N.; Žemlicková, H.; Schytte Olsen, S.; Wolff Sönksen, U.; Märtin, P.; Ivanova, M.; Lyytikäinen, O.; Jalava, J.; Coignard, B.; Eckmanns, T.; Abu Sin, M.; Haller, S.; Daikos, G. L.; Gikas, A.; Tsiodras, S.; Kontopidou, F.; Tóth, Á.; Hajdu, Á.; Guólaugsson, Ó.; Kristinsson, K. G.; Murchan, S.; Burns, K.; Pezzotti, P.; Gagliotti, C.; Dumpis, U.; Liuimiene, A.; Perrin, M.; Borg, M. A.; de Greeff, S. C.; Monen, J. C.; Koek, M. B.; Elstrøm, P.; Zabicka, D.; Deptula, A.; Hryniewicz, W.; Caniça, M.; Nogueira, P. J.; Fernandes, P. A.; Manageiro, V.; Popescu, G. A.; Serban, R. I.; Schréterová, E.; Litvová, S.; Štefkovicová, M.; Kolman, J.; Klavs, I.; Korošec, A.; Aracil, B.; Asensio, A.; Pérez-Vázquez, M.; Billström, H.; Larsson, S.; Reilly, J. S.; Johnson, A.; Hopkins, S. Attributable Deaths and Disability-Adjusted Life-Years Caused by Infections with Antibiotic-Resistant Bacteria in the EU and the European Economic Area in 2015: A Population-Level Modelling Analysis. *Lancet Infect. Dis.* **2019**, *19* (1), 56–66. https://doi.org/10.1016/S1473-3099(18)30605-4.

(21)   Levy, S. B.; Marshall, B. Antibacterial Resistance Worldwide: Causes, Challenges and Responses. *Nat.Med.* **2004**, *10* (1078-8956 (Print)), S122–S129. https://doi.org/10.1038/nm1145.

(22)   Stewart, P. S.; William Costerton, J. Antibiotic Resistance of Bacteria in Biofilms. *Lancet* **2001**, *358* (9276), 135–138. https://doi.org/10.1016/S0140-6736(01)05321-1.

(23)   Wernli, D.; Jørgensen, P. S.; Parmley, E. J.; Troell, M.; Majowicz, S.; Harbarth, S.; Léger, A.; Lambraki, I.; Graells, T.; Henriksson, P. J. G.; Carson, C.; Cousins, M.; Skoog Ståhlgren, G.; Mohan, C. V.; Simpson, A. J. H.; Wieland, B.; Pedersen, K.; Schneider, A.; Chandy, S. J.; Wijayathilaka, T. P.; Delamare-Deboutteville, J.; Vila, J.; Stålsby Lundborg, C.; Pittet, D. Evidence for Action: A One Health Learning Platform on Interventions to Tackle Antimicrobial Resistance. *Lancet Infect. Dis.* **2020**, *20* (12), e307–e311. https://doi.org/10.1016/S1473-3099(20)30392-3.

(24)   US Department of Health and Human Services; CDC. Antibiotic Resistance Threats in the United States. *Centers Dis. Control Prev.* **2019**, 1–113.

(25) World Health Organisation. Global Action Plan on Antimicrobial Resistance. *WHO Press* **2015**, 1–28. https://doi.org/ISBN 978 92 4 150976 3.

(26) Mattar, C.; Edwards, S.; Baraldi, E.; Hood, J. An Overview of the Global Antimicrobial Resistance Research and Development Hub and the Current Landscape. *Curr. Opin. Microbiol.* **2020**, *57*, 56–61. https://doi.org/10.1016/j.mib.2020.06.009.

(27) European Observatory on Health Systems and Policies. *Challenges to Tackling Antimicrobial Resistance Economic and Policy Response*; 2019; Vol. 53.

(28) Clatworthy, A. E.; Pierson, E.; Hung, D. T. Targeting Virulence : A New Paradigm for Antimicrobial Therapy. **2007**, *3* (9), 541–548. https://doi.org/10.1038/nchembio.2007.24.

(29) Schultz, R. Tackling Antimicrobial Resistance Globally. *Med. J. Aust.* **2018**, *208* (6). https://doi.org/10.5694/mja17.01125.

(30) Berne, C.; Ellison, C. K.; Ducret, A.; Brun, Y. V. Bacterial Adhesion at the Single-Cell Level. *Nat. Rev. Microbiol.* **2018**, *16* (October), 616–627. https://doi.org/10.1038/s41579-018-0057-5.

(31) Wong, G. C. L. Roadmap on Emerging Concepts in the Physical Biology of Bacterial Biofilms: From Surface Sensing to Community Formation. *Mater. Today Proc.* **2019**, *27* (xxxx), 0–31. https://doi.org/10.1080/14484846.2018.1432089.

(32) Belas, R. Biofilms, Flagella, and Mechanosensing of Surfaces by Bacteria. *Trends Microbiol.* **2014**, *22* (9), 517–527. https://doi.org/10.1016/j.tim.2014.05.002.

(33) Garrett, T. R.; Bhakoo, M.; Zhang, Z. Bacterial Adhesion and Biofilms on Surfaces. *Prog. Nat. Sci.* **2008**, *18* (9), 1049–1056. https://doi.org/10.1016/j.pnsc.2008.04.001.

(34) Flemming, H.-C.; Wingender, J.; Szewzyk, U.; Steinberg, P.; Rice, S. A.; Kjelleberg, S. Biofilms: An Emergent Form of Bacterial Life. *Nat. Rev. Microbiol.* **2016**, *14* (9), 563–575. https://doi.org/10.1038/nrmicro.2016.94.

(35) Donlan, R. M. Biofilms: Microbial Life on Surfaces. *Emerg. Infect. Dis.* **2002**, *8* (9), 881–890. https://doi.org/10.3201/eid0809.020063.

(36) Tuson, Hannah H. Weibel, D. B. Bacteria–Surface Interactions. *Soft Matter* **2013**, *9* (17), 4368. https://doi.org/10.1039/c3sm27705d.

(37) Auer, G. K.; Weibel, D. B. Bacterial Cell Mechanics. *Biochemistry* **2017**, *56* (29), 3710–3724. https://doi.org/10.1021/acs.biochem.7b00346.

(38) Philips, R.; Kondev, J.; Theriot, J.; Garcia, H. G.; Orme, N. *Physical Biology of the Cell*, 2nd ed.; Scholl, S., Wolfe, N., Clarke, M., Eds.; Garland Science: New York, 2013.

(39) García-Bayona, L.; Comstock, L. E. Bacterial Antagonism in Host-Associated Microbial Communities. *Science (80-.).* **2018**, *361* (6408). https://doi.org/10.1126/science.aat2456.

(40) Berg, G.; Rybakova, D.; Fischer, D.; Cernava, T.; Vergès, M. C. C.; Charles, T.; Chen, X.; Cocolin, L.; Eversole, K.; Corral, G. H.; Kazou, M.; Kinkel, L.; Lange, L.; Lima, N.; Loy, A.; Macklin, J. A.; Maguin, E.; Mauchline, T.; McClure, R.; Mitter, B.; Ryan, M.; Sarand, I.; Smidt, H.; Schelkle, B.; Roume, H.; Kiran, G. S.; Selvin, J.; Souza, R. S. C. de; Van Overbeek, L.; Singh, B. K.; Wagner, M.; Walsh, A.; Sessitsch, A.; Schloter, M. Microbiome Definition Re-Visited: Old Concepts and New Challenges. *Microbiome* **2020**, *8* (1), 1–22. https://doi.org/10.1186/s40168-020-00875-0.

(41) Nadell, C. D.; Drescher, K.; Foster, K. R. Spatial Structure, Cooperation and Competition in

Biofilms. *Nat. Rev. Microbiol.* **2016**, *14* (9), 589–600. https://doi.org/10.1038/nrmicro.2016.84.

(42) Cloutier, M.; Mantovani, D.; Rosei, F. Antibacterial Coatings: Challenges, Perspectives, and Opportunities. *Trends Biotechnol.* **2015**, *33* (11), 637–652. https://doi.org/10.1016/j.tibtech.2015.09.002.

(43) Flemming, A. Sir Alexander Fleming - Nobel Lecture: Penicillin. *Nov. Price* **1945**, 11.

(44) Hecht, E. *Optics*, 4th ed.; Pearson Education Inc.: Sansome St., 2002.

(45) Lakowicz, J. R. *Principles of Fluorescence Spectroscopy Principles of Fluorescence Spectroscopy*; 2006. https://doi.org/10.1007/978-0-387-46312-4.

(46) Metwalli, E.; Pantano, C. G. Reactive Ion Etching of Glasses : Composition Dependence. **2003**, *207*, 21–27. https://doi.org/10.1016/S0168-583X(03)00517-2.

(47) Vernon-Parry, K. D. Scanning Electron Microscopy: An Introduction. *Analysis* **2000**, *13* (4), 40–44.

(48) Oura, K. et al. 14. Growth of Thin Films. In *Surface Science*; Springer- Verlag: Berlin Heidelberg, 2003; pp 357–387.

(49) Daoud, W. A. et al. *Self-Cleaning Materials and Surfaces: A Nanotechnology Approach*, 1st ed.; Daoud, W. A., Ed.; John Wiley & Sons, Ltd: Chichster.

(50) Bonn, D.; Eggers, J.; Indekeu, J.; Meunier, J.; Rolley, E. Wetting and Spreading. *Rev. Mod. Phys.* **2009**, *81* (2), 1–62.

(51) Nagayama, G.; Zhang, D. Intermediate Wetting State at Nano/Microstructured Surfaces. *Soft Matter* **2020**, *16* (14), 3514–3521. https://doi.org/10.1039/c9sm02513h.

(52) Axelrod, D. Total Internal Reflection Fluorescence Microscopy in Cell Biology [Review]. *Traffic* **2001**, *2*, 764–774. https://doi.org/10.1034/j.1600-0854.2001.21104.x.

(53) Azeredo, J.; Azevedo, N. F.; Briandet, R.; Cerca, N.; Coenye, T.; Costa, A. R.; Desvaux, M.; Di Bonaventura, G.; Hébraud, M.; Jaglic, Z.; Kačániová, M.; Knøchel, S.; Lourenço, A.; Mergulhão, F.; Meyer, R. L.; Nychas, G.; Simões, M.; Tresse, O.; Sternberg, C. Critical Review on Biofilm Methods. *Crit. Rev. Microbiol.* **2017**, *43* (3), 313–351. https://doi.org/10.1080/1040841X.2016.1208146.

(54) Perni, S.; Preedy, E. C.; Prokopovich, P. Success and Failure of Colloidal Approaches in Adhesion of Microorganisms to Surfaces. *Adv. Colloid Interface Sci.* **2014**, *206*, 265–274. https://doi.org/10.1016/j.cis.2013.11.008.

(55) Costerton, J.W., Stewart, P.S. & Greenberg, E. P. Bacterial Biofilms: A Common Cause of Persistent Infections. *Science (80-.).* **1999**, *284* (May), 1318–1322.

(56) Jayan, H.; Pu, H.; Sun, D. Trends in Food Science & Technology Recent Development in Rapid Detection Techniques for Microorganism Activities in Food Matrices Using Bio-Recognition : A Review. **2020**, *95* (November 2019), 233–246. https://doi.org/10.1016/j.tifs.2019.11.007.

(57) Edition, F.; The, I.; Addendum, F. *Guidelines for Drinking-Water Quality*; WHO.

(58) Flemming, H. Biofilms : An Emergent Form of Bacterial Life. *Nat. Publ. Gr.* **2016**, *14* (9), 563–575. https://doi.org/10.1038/nrmicro.2016.94.

(59)   Cundell, T. The Limitations of the Colony-Forming Unit in Microbiology. *Eur. Pharm. Rev.* **2015**, *20* (6), 11–13.

(60)   Hameed, S.; Xie, L.; Ying, Y. Trends in Food Science & Technology Conventional and Emerging Detection Techniques for Pathogenic Bacteria in Food Science : A Review. *Trends Food Sci. Technol.* **2018**, *81* (December 2017), 61–73. https://doi.org/10.1016/j.tifs.2018.05.020.

(61)   Chalklen, T.; Jing, Q.; Kar-narayan, S. Detection Techniques. **2020**, 11–13.

(62)   Rajapaksha, P.; Elbourne, A. Pathogenic Microorganisms. **2019**, 396–411. https://doi.org/10.1039/c8an01488d.

(63)   Chai, Y.; Horikawa, S.; Li, S.; Wikle, H. C.; Chin, B. A. Biosensors and Bioelectronics A Surface-Scanning Coil Detector for Real-Time , in-Situ Detection of Bacteria on Fresh Food Surfaces. *Biosens. Bioelectron.* **2013**, *50*, 311–317. https://doi.org/10.1016/j.bios.2013.06.056.

(64)   Liu, X.; Marrakchi, M.; Xu, D.; Dong, H.; Andreescu, S. Biosensors and Bioelectronics Biosensors Based on Modularly Designed Synthetic Peptides for Recognition , Detection and Live / Dead Differentiation of Pathogenic Bacteria. *Biosens. Bioelectron.* **2016**, *80*, 9–16. https://doi.org/10.1016/j.bios.2016.01.041.

(65)   Kim, J. A.; Wales, D. J.; Thompson, A. J.; Yang, G. Fiber-Optic SERS Probes Fabricated Using Two-Photon Polymerization For Rapid Detection of Bacteria. **2020**, *1901934*, 1–12. https://doi.org/10.1002/adom.201901934.

(66)   Yoo, S. M.; Lee, S. Y. Optical Biosensors for the Detection of Pathogenic Microorganisms. *Trends Biotechnol.* **2016**, *34* (1), 7–25. https://doi.org/10.1016/j.tibtech.2015.09.012.

(67)   Zwietering, M. H.; Jongenburger, I.; Rombouts, F. M.; van 't Riet, K. Modeling of the Bacterial Growth Curve. *Appl. Environental Microbiol.* **1990**, *56* (6), 1875–1881.

(68)   Tj, K. M. C.; Tj, E. The Use of Gompertz Models in Growth Analyses , and New Gompertz-Model Approach : An Addition to the Unified-Richards Family. **2017**, 1–17.

(69)   Fujikawa, H.; Morozumi, S. Modeling Surface Growth of Escherichia Coli on Agar Plates. **2005**, *71* (12), 7920–7926. https://doi.org/10.1128/AEM.71.12.7920.

(70)   Schindelin, J.; Arganda-Carreras, Ignacio Frise, E.; Kaynig, V.; Longair, M.; Pietzsch, T.; Preibisch, S.; Rueden, C.; Saalfeld, S.; Schmid, B.; Tinevez, J.-Y.; White, D. J.; Hartenstein, V.; Eliceiri, K.; Tomancak, P.; Cardona, A. Fiji - an Open Source Platform for Biological Image Analysis. *Nat Methods* **2009**, *9* (7), 676–682. https://doi.org/10.1038/nmeth.2019.Fiji.

(71)   Soille, P. W a Tersheds in Digital Spaces : An Efficient Algorithm Based on Immersion Simulations. **1991**.

(72)   Yu, A. C. S.; Loo, J. F. C.; Yu, S.; Kong, S. K.; Chan, T. Monitoring Bacterial Growth Using Tunable Resistive Pulse Sensing with a Pore-Based Technique. **2014**, 855–862. https://doi.org/10.1007/s00253-013-5377-9.

(73)   Rowlett, V. W.; Mallampalli, V. K. P. S.; Karlstaedt, A.; Dowhan, W.; Taegtmeyer, H.; Margolin, W.; Vitrac, H. The Impact of Membrane Phospholipid Alterations in Escherichia Coli on Cellular Function 1. *J. Bacteriol.* **2017**, *199* (13), e00849-16. https://doi.org/10.1128/JB.00849-16.

(74)   Chao, Y.; Zhang, T. Optimization of Fixation Methods for Observation of Bacterial Cell Morphology and Surface Ultrastructures by Atomic Force Microscopy. **2011**, 381–392.

https://doi.org/10.1007/s00253-011-3551-5.

(75)   Tseng, D.; Cerqueira, L.; Ozcan, A.; Azevedo, N. F. Identi Fi Cation of Pathogenic Bacteria in Complex Samples Using a Smartphone Based Fl Uorescence. **2018**, 36493–36502. https://doi.org/10.1039/c8ra06473c.

(76)   Buttner, M. P.; Cruz-perez, P.; Stetzenbach, L. D. Enhanced Detection of Surface-Associated Bacteria in Indoor Environments by Quantitative PCR. **2001**, *67* (6), 2564–2570. https://doi.org/10.1128/AEM.67.6.2564.

(77)   Dartnell, L. R.; Roberts, T. A.; Moore, G.; Ward, J. M.; Muller, J. P. Fluorescence Characterization of Clinically-Important Bacteria. *PLoS One* **2013**, *8* (9), 1–13. https://doi.org/10.1371/journal.pone.0075270.

(78)   Online, V. A.; Safavieh, M.; Ahmed, M. U.; Sokullu, E.; Ng, A.; Braescu, L.; Zourob, M. A Simple Cassette as Point-of-Care Diagnostic Device for Naked-Eye Colorimetric Bacteria Detection †. **2014**, 482–487. https://doi.org/10.1039/c3an01859h.

(79)   Wang, H.; Zhou, Y.; Jiang, X.; Sun, B.; Zhu, Y.; Wang, H.; Su, Y. Angewandte Simultaneous Capture , Detection , and Inactivation of Bacteria as Enabled by a Surface-Enhanced Raman Scattering Multifunctional Angewandte. **2015**, 5132–5136. https://doi.org/10.1002/anie.201412294.

(80)   Lichtman; Conchello. Fluorescence Microscopy: Reduced Photobleaching of Rhodamine and Fluorescein Protein Conjugates by n-Propyl Gallate. *Science (80-.).* **2005**, *217* (4566), 1252. https://doi.org/10.1038/NMETH817.

(81)   Waters, J. C. Accuracy and Precision in Quantitative Fluorescence Microscopy. *J. Cell Biol.* **2009**, *185* (7), 1135–1148. https://doi.org/10.1083/jcb.200903097.

(82)   Waters, J. C.; Wittmann, T. *Concepts in Quantitative Fluorescence Microscopy*, 1st ed.; Elsevier Inc., 2014; Vol. 123. https://doi.org/10.1016/B978-0-12-420138-5.00001-X.

(83)   Pawley, J. B. Fundamental Limits in Confocal Microscopy. *Handb. Biol. Confocal Microsc. Third Ed.* **2006**, 20–42. https://doi.org/10.1007/978-0-387-45524-2_2.

(84)   Ghosh, A.; Sharma, A.; Chizhik, A. I.; Isbaner, S.; Ruhlandt, D.; Tsukanov, R.; Gregor, I.; Karedla, N.; Enderlein, J. Graphene-Based Metal-Induced Energy Transfer for Sub-Nanometre Optical Localization. *Nat. Photonics* **2019**. https://doi.org/10.1038/s41566-019-0510-7.

(85)   Isbaner, S.; Karedla, N.; Kaminska, I.; Ruhlandt, D.; Raab, M.; Bohlen, J.; Chizhik, A.; Gregor, I.; Tinnefeld, P.; Enderlein, J.; Tsukanov, R. Axial Colocalization of Single Molecules with Nanometer Accuracy Using Metal-Induced Energy Transfer. **2018**. https://doi.org/10.1021/acs.nanolett.8b00425.

(86)   Phys, A. Volmer-Weber Growth Stages of Polycrystalline Metal Films Probed by in Situ and Real-Time Optical Diagnostics. **2018**, *183105* (November 2015). https://doi.org/10.1063/1.4935034.

(87)   Maniyara, R. A.; Rodrigo, D.; Yu, R.; Canet-Ferrer, J.; Ghosh, D. S.; Yongsunthon, R.; Baker, D. E.; Rezikyan, A.; García de Abajo, F. J.; Pruneri, V. Tunable Plasmons in Ultrathin Metal Films. *Nat. Photonics* **2019**, *13* (5), 328–333. https://doi.org/10.1038/s41566-019-0366-x.

(88)   Ro, C.; Chizhik, A. I.; Gregor, I.; Schleifenbaum, F.; Mu, C. B.; Meixner, A. J. Electrodynamic Coupling of Electric Dipole Emitters to a Fluctuating Mode Density within a Nanocavity. **2012**,

163002 (April), 1–4. https://doi.org/10.1103/PhysRevLett.108.163002.

(89)   Physics, C.; Chemistry, A.; Received, G. Single-Molecule Fluorescence near a Metal Layer. **1999**.

(90)   Akubovsky, D. M. I. Y.; Rsenin, A. L. V. A.; Ury, Y. V; Tebunov, S.; Edyanin, D. M. Y. U. F.; Olkov, V. A. S. V. Optical Constants and Structural Properties of Thin Gold Films. **2017**, *25* (21), 326–333.

(91)   Thorn, K.; Kellogg, D. A Quick Guide to Light Microscopy in Cell Biology. **2016**, *27*. https://doi.org/10.1091/mbc.E15-02-0088.

(92)   Axelrod, D. Total Internal Reflection Fluorescence Microscopy in Cell Biology. **2001**, No. 2, 764–774.

(93)   Chizhik, A. I.; Rother, J.; Gregor, I.; Janshoff, A. Metal-Induced Energy Transfer for Live Cell Nanoscopy. **2014**, *8* (February), 8–11. https://doi.org/10.1038/nphoton.2013.345.

(94)   Terborg, R. A.; Pello, J.; Mannelli, I.; Torres, J. P.; Pruneri, V. Ultrasensitive Interferometric On-Chip Microscopy of Transparent Objects. **2016**, No. June, 1–8.

(95)   Otter, J.; Brophy, K.; Palmer, J.; Harrison, N.; Riley, J.; Williams, D.; Larrouy-maumus, G. Smart Surfaces to Tackle Infection and Antimicrobial Resistance. **2020**, No. 4.

(96)   Salwiczek, M.; Qu, Y.; Gardiner, J.; Strugnell, R. a.; Lithgow, T.; McLean, K. M.; Thissen, H. Emerging Rules for Effective Antimicrobial Coatings. *Trends Biotechnol.* **2014**, *32* (2), 82–90. https://doi.org/10.1016/j.tibtech.2013.09.008.

(97)   Choi, H.; Rangarajan, N.; Weisshaar, J. C. Lights, Camera, Action! Antimicrobial Peptide Mechanisms Imaged in Space and Time. *Trends Microbiol.* **2016**, *24* (2), 111–122. https://doi.org/10.1016/j.tim.2015.11.004.

(98)   Swartjes, J.; Sharma, P.; van Kooten, T.; van der Mei, H.; Mahmoudi, M.; Busscher, H.; Rochford, E. Current Developments in Antimicrobial Surface Coatings for Biomedical Applications. *Curr. Med. Chem.* **2014**, *22*, 2116–2129. https://doi.org/10.2174/0929867321666140916121355.

(99)   Liu, S.; Hu, M.; Zeng, T. H.; Wu, R.; Jiang, R.; Wei, J.; Wang, L.; Kong, J.; Chen, Y. Lateral Dimension-Dependent Antibacterial Activity of Graphene Oxide Sheets. *Langmuir* **2012**, *28* (33), 12364–12372. https://doi.org/10.1021/la3023908.

(100)   Dellieu, L.; Lawarée, E.; Reckinger, N.; Didembourg, C.; Letesson, J. J.; Sarrazin, M.; Deparis, O.; Matroule, J. Y.; Colomer, J. F. Do CVD Grown Graphene Films Have Antibacterial Activity on Metallic Substrates? *Carbon N. Y.* **2015**, *84* (1), 310–316. https://doi.org/10.1016/j.carbon.2014.12.025.

(101)   Liu, S.; Zeng, T. H.; Hofmann, M.; Burcombe, E.; Wei, J.; Jiang, R.; Kong, J.; Chen, Y. Antibacterial Activity of Graphite, Graphite Oxide, Graphene Oxide, and Reduced Graphene Oxide: Membrane and Oxidative Stress. *ACS Nano* **2011**, *5* (9), 6971–6980. https://doi.org/10.1021/nn202451x.

(102)   Lemire, J. A.; Harrison, J. J.; Turner, R. J. Antimicrobial Activity of Metals: Mechanisms, Molecular Targets and Applications. *Nat. Rev. Microbiol.* **2013**, *11* (6), 371–384. https://doi.org/10.1038/nrmicro3028.

(103) Ivanova, E. P.; Hasan, J.; Webb, H. K.; Truong, V. K.; Watson, G. S.; Watson, J. A.; Baulin, V. A.; Pogodin, S.; Wang, J. Y.; Tobin, M. J.; Löbbe, C.; Crawford, R. J. Natural Bactericidal Surfaces: Mechanical Rupture of Pseudomonas Aeruginosa Cells by Cicada Wings. *Small* **2012**, *8* (16), 2489–2494. https://doi.org/10.1002/smll.201200528.

(104) Watson, G. S.; Cribb, B. W.; Schwarzkopf, L.; Watson, J. A.; Watson, G. S. Contaminant Adhesion (Aerial / Ground Biofouling) on the Skin of a Gecko. *J. R. Soc. Interface* **2015**, *12* (108), 1–13. https://doi.org/10.1098/rsif.2015.0318.

(105) Ivanova, E. P.; Hasan, J.; Webb, H. K.; Gervinskas, G.; Juodkazis, S.; Truong, V. K.; Wu, A. H. F.; Lamb, R. N.; Baulin, V. a; Watson, G. S.; Watson, J. a; Mainwaring, D. E.; Crawford, R. J. Bactericidal Activity of Black Silicon. *Nat. Commun.* **2013**, *4*, 2838–2845. https://doi.org/10.1038/ncomms3838.

(106) Abinash, T.; Prosenjit, S.; Bo, S.; Briscoe, W. H. Natural and Bioinspired Nanostructured Bactericidal Surfaces. *Adv. Colloid Interface Sci.* **2017**, *248*, 85–104. https://doi.org/10.1016/j.cis.2017.07.030.

(107) Luan, Y.; Liu, S.; Pihl, M.; van der Mei, H. C.; Liu, J.; Hizal, F.; Choi, C. H.; Chen, H.; Ren, Y.; Busscher, H. J. Bacterial Interactions with Nanostructured Surfaces. *Curr. Opin. Colloid Interface Sci.* **2018**, *38*, 1. https://doi.org/10.1016/J.COCIS.2018.10.007.

(108) Lin, N.; Berton, P.; Moraes, C.; Rogers, R. D.; Tufenkji, N. Nanodarts, Nanoblades, and Nanospikes: Mechano-Bactericidal Nanostructures and Where to Find Them. *Adv. Colloid Interface Sci.* **2018**, *252*, 55–68. https://doi.org/10.1016/j.cis.2017.12.007.

(109) Cheng, Y.; Feng, G.; Moraru, C. I. Micro- and Nanotopography Sensitive Bacterial Attachment Mechanisms: A Review. *Front. Microbiol.* **2019**, *10* (February), 191. https://doi.org/10.3389/fmicb.2019.00191.

(110) Modaresifar, K.; Azizian, S.; Ganjian, M.; Fratila-Apachitei, L. E.; Zadpoor, A. A. Bactericidal Effects of Nanopatterns: A Systematic Review. *Acta Biomater.* **2019**, *83*, 29–36. https://doi.org/10.1016/j.actbio.2018.09.059.

(111) Rosenberg, M.; Azevedo, N. F.; Ivask, A. Propidium Iodide Staining Underestimates Viability of Adherent Bacterial Cells. *Sci. Rep.* **2019**, *9* (1), 1–12. https://doi.org/10.1038/s41598-019-42906-3.

(112) Shi, L.; Günther, S.; Hübschmann, T.; Wick, L. Y.; Harms, H.; Müller, S. Limits of Propidium Iodide as a Cell Viability Indicator for Environmental Bacteria. *Cytom. Part A* **2007**, *71* (8), 592–598. https://doi.org/10.1002/cyto.a.20402.

(113) Gómez-Suárez, C.; Busscher, H. J.; Van Der Mei, H. C. Analysis of Bacterial Detachment from Substratum Surfaces by the Passage of Air-Liquid Interfaces. *Appl. Environ. Microbiol.* **2001**, *67* (6), 2531–2537. https://doi.org/10.1128/AEM.67.6.2531.

(114) Peterson, B. W.; Sharma, P. K.; van der Mei, H. C.; Busscher, H. J. Bacterial Cell Surface Damage Due to Centrifugal Compaction. *Appl. Environ. Microbiol.* **2012**, *78* (1), 120–125. https://doi.org/10.1128/AEM.06780-11.

(115) Mannelli, I.; Sague, F.; Pruneri, V.; Reigada, R. Lipid Vesicle Interaction with Hydrophobic Surfaces : A Coarse- Grained Molecular Dynamics Study. **2016**. https://doi.org/10.1021/acs.langmuir.6b03364.

(116) Li, H.; Yan, T.; Fichthorn, K. A.; Yu, S. Dynamic Contact Angles and Mechanisms of Motion of

Water Droplets Moving on Nano-Pillared Superhydrophobic Surfaces: A Molecular Dynamics Simulation Study. *Langmuir* **2018**, *34*, 9917–9926. https://doi.org/10.1021/acs.langmuir.8b01324.

(117) Gru, H.; Yerushalmi-rozen, R. Wetting Behavior of Water Droplets on Hydrophobic Microtextures of Comparable Size. **2004**, *220* (9), 10015–10019.

(118) Mannelli, I.; Reigada, R.; Suárez, I.; Janner, D.; Carrilero, A.; Mazumder, P.; Sagués, F.; Pruneri, V.; Lakadamyali, M. Functionalized Surfaces with Tailored Wettability Determine Influenza A Infectivity. *ACS Appl. Mater. Interfaces* **2016**, acsami.6b02779. https://doi.org/10.1021/acsami.6b02779.

(119) Marrink, S. J.; Risselada, H. J.; Yefimov, S.; Tieleman, D. P.; De Vries, A. H. The MARTINI Force Field: Coarse Grained Model for Biomolecular Simulations. *J. Phys. Chem. B* **2007**, *111* (27), 7812–7824. https://doi.org/10.1021/jp071097f.

(120) Lindahl, E.; Hess, B.; van der Spoel, D. GROMACS 3.0: A Package for Molecular Simulation and Trajectory Analysis. *J. Mol. Model.* **2001**, *7* (8), 306–317. https://doi.org/10.1007/S008940100045.

(121) Dalvi, V. H.; Rossky, P. J. Molecular Origins of Fluorocarbon Hydrophobicity. *Proc. Natl. Acad. Sci.* **2010**, *107* (31), 13603–13607. https://doi.org/10.1073/pnas.0915169107.

(122) Graupe, M.; Takenaga, M.; Koini, T.; Colorado, R.; Lee, T. R. Oriented Surface Dipoles Strongly Influence Interfacial Wettabilities. *J. Am. Chem. Soc.* **1999**, *121* (13), 3222–3223. https://doi.org/10.1021/ja983582h.

(123) Infante, D.; Koch, K. W.; Mazumder, P.; Tian, L.; Carrilero, A.; Tulli, D.; Baker, D.; Pruneri, V. Durable, Superhydrophobic, Antireflection, and Low Haze Glass Surfaces Using Scalable Metal Dewetting Nanostructuring. *Nano Res.* **2013**, *6* (6), 429–440. https://doi.org/10.1007/s12274-013-0320-z.

(124) Mannelli, I.; Reigada, R.; Suárez, I.; Janner, D.; Carrilero, A.; Mazumder, P.; Sagués, F.; Pruneri, V.; Lakadamyali, M. Functionalized Surfaces with Tailored Wettability Determine Influenza A Infectivity. *ACS Appl. Mater. Interfaces* **2016**, acsami.6b02779. https://doi.org/10.1021/acsami.6b02779.

(125) Veatch, S. L.; Machta, B. B.; Shelby, S. A.; Chiang, E. N.; Holowka, D. A.; Baird, B. A. Correlation Functions Quantify Super-Resolution Images and Estimate Apparent Clustering Due to over-Counting. *PLoS One* **2012**, *7* (2), 1–13. https://doi.org/10.1371/journal.pone.0031457.

(126) Stiefel, P.; Schmidt-Emrich, S.; Maniura-Weber, K.; Ren, Q. Critical Aspects of Using Bacterial Cell Viability Assays with the Fluorophores SYTO9 and Propidium Iodide. *BMC Microbiol.* **2015**, *15* (1). https://doi.org/10.1186/s12866-015-0376-x.